

SELF-ORGANIZED DUST ROTATION IN AN UNMAGNETIZED DC GLOW DISCHARGE

By

**MANJIT KAUR
PHYS06200804001**

Institute for Plasma Research, Gandhinagar

A thesis submitted to the

Board of Studies in Physical Sciences

In partial fulfillment of requirements

for the Degree of

DOCTOR OF PHILOSOPHY

of

HOMI BHABHA NATIONAL INSTITUTE

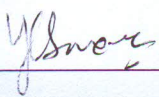


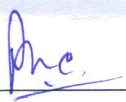
August, 2015

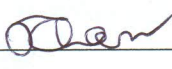
Homi Bhabha National Institute

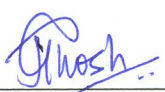
Recommendations of the Viva Voice Board

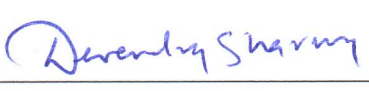
As members of the Viva Voice Board, we certify that we have read the dissertation prepared by **Manjit Kaur** entitled "Self-Organized Dust Rotation in an unmagnetized DC Glow Discharge" and recommend that it may be accepted as fulfilling the dissertation requirement for the Degree of Doctor of Philosophy.


Chairman: Prof. Y. C. Saxena **Date:** 11/12/2015


Guide / Convener: Prof. P. K. Chattopadhyay **Date:** 11/12/2015


Examiner: Prof. Manoranjan Khan **Date:** 11/12/2015


Member 1: Dr. Joydeep Ghosh **Date:** 11/12/2015


Member 2: Dr. Devendra Sharma **Date:** 11/12/2015

Final approval and acceptance of this dissertation is contingent upon the candidate's submission of the final copies of the dissertation to HBNI.

I hereby certify that I have read this dissertation prepared under my direction and recommend that it may be accepted as fulfilling the dissertation requirement.

Date: 11/12/2015

Place: Gandhinagar


Guide

STATEMENT BY AUTHOR

This dissertation has been submitted in partial fulfilment of requirements for an advanced degree at Homi Bhabha National Institute (HBNI) and is deposited in the Library to be made available to borrowers under rules of the HBNI.

Brief quotations from this dissertation are allowable without special permission, provided that accurate acknowledgement of source is made. Requests for permission for extended quotation from or reproduction of this manuscript in whole or in part may be granted by the Competent Authority of HBNI when in his or her judgment, the proposed use of the material is in the interests of scholarship. In all other instances, however, permission must be obtained from the author.

Dated: 28/08/2015


Manjit Kaur

DECLARATION

I, hereby declare that the investigation presented in the thesis has been carried out by me. The work is original and has not been submitted earlier as a whole or in part for a degree/diploma at this or any other Institution/University.

Dated: 28/08/2015


Manjit Kaur

List of Publications arising from the thesis

Published in refereed Journals

1. Observation of dust torus with poloidal rotation in direct current glow discharge
Manjit Kaur, Sayak Bose, P.K. Chattopadhyay, Devendra Sharma, J. Ghosh, and Y.C. Saxena, *Physics of Plasmas* 22, 033703 (2015).
2. Generation of multiple toroidal dust vortices by a non-monotonic density gradient in a direct current glow discharge plasma
Manjit Kaur, Sayak Bose, P. K. Chattopadhyay, D. Sharma, J. Ghosh, Y. C. Saxena and Edward Thomas, *Physics of Plasmas* 22, 093702 (2015).

Submitted for Publication

1. CPED – A test bed for studying dust vortices and other collective phenomena
Manjit Kaur, Sayak Bose, P. K. Chattopadhyay, J. Ghosh and Y. C. Saxena, *Manuscript under consideration* (2015).

To be submitted for Publication

1. Resolving Issues Associated with Langmuir Probe Measurements in High pressure Complex (Dusty) Plasmas
Manjit Kaur, Sayak Bose, P. K. Chattopadhyay, J. Ghosh and Y. C. Saxena, *Manuscript under preparation* (2015).
2. On the evolution of poloidal dust rotation with ambient neutral density
Manjit Kaur, Sayak Bose, P. K. Chattopadhyay, J. Ghosh and Y. C. Saxena, *Manuscript under preparation* (2015).



Manjit Kaur

Dedicated to

.... my parents....

ACKNOWLEDGEMENTS

I would like to start by expressing my sincere gratitude to my thesis supervisor Prof. P. K. Chattopadhyay for the continuous support of my PhD study and research, for his patience, motivation, enthusiasm, and immense knowledge. I am also thankful to him for many hours of help he provided me. I humbly appreciate his motivating ideas and fruitful discussions with him. His great hands-on-experience in experiments helped me in learning many new and interesting techniques to deal a problem.

My deepest gratitude is to Prof. Y.C. Saxena. I have been amazingly fortunate to have a teacher like Prof. Saxena whose patience and support helped me overcome many crisis situations and finish this thesis. Prof. Saxena is one of the best teachers that I have had in my life. I am deeply grateful to him for the discussions that helped me sort out the technical details of my work.

I would like to extend my thanks to Dr. Joydeep Ghosh. He has been always there to listen and give advice. His insightful comments and constructive criticisms at different stages of my research were thought-provoking and they helped me focus my ideas. I would like to thank him for asking the hard questions also which incanted me to widen my research from various perspectives.

I specially thank to Dr. D. Sharma, for his insightful comments and encouragement. I would like to extend my thanks to Prof. P. K. Kaw for being an excellent teacher who always listen very patiently and capable of providing great ideas to solve any physics problem possible. I am also thankful to Prof. Abhijeet Sen, Prof. R. Pal, Prof. Amita Das, Prof. R. Singh, Prof. R. Ganesh, Dr. Ramsubramanian, Dr. M. Kundu, Dr. Rajiv Goswami and Dr. Manoj Warrior for numerous discussions and lectures on related topics that helped me improve my knowledge in the plasma physics. I am also very thankful to our Academic Dean- Prof S. Mukherjee for encouraging each and every scholar to do experiments and for keeping us always updated about all the recent modifications happening in HBNI PhD guidelines. I am extremely thankful to Prof. Prabal K. chattopadhyay for involving me in collaboration with Prof. Edward Jr. Thomas. I am truly indebted and thankful to Prof. Edward Thomas Jr. who helped me in learning the Particle Image Velocimetry (PIV) technique.

I want to thank my classmate, lab mate and best friend – Sayak for providing me unforgettable cool ambience during first year course work, for the sleepless nights we

were working together before deadlines and throughout my Ph.D. Special thanks go to him. Without his help and humour, my PhD life would have been a very dull time. His support helped me overcome setbacks and stay focused in my research work. I deeply appreciate his belief in me. I also thank my fellow lab mates- Kshitish bhaiya, Soumen, Sonu and Hiral for the stimulating discussions and for all the fun we have had during these years. I have been very lucky to be a part of the Basic Lab. I am also grateful to the staff members of Electronics Lab, Workshop, Drafting Section, Computer Centre, Library, Stores, Purchase Section and Administration at Institute for Plasma Research for their co-operation and help during my entire duration of PhD.

I also thank my senior research scholars- Kishor da, Maya di, Vikrant bhaiya, Sunita di, Shekhar anna, Jugal bhaiya, Sharad bhaiya, Satya bhai, Sita di, Ujjwal bhaiya, Vikram bhaiya, Guru, Ashwin, Sanat, Sushil bhaiya, Rameswar, Pravesh and junior research scholars- Aditya, Vikram, Veda, Sandeep, Dushyant, Rana, Akanksha, Deepa, Vidhi, Saleem, Vara, Vibhu, Mangilal, Neeraj, Meghraj, Sameer, Harish, Rupendra, Chandrashekhar, Surbhi, Bhumika, Arghya, Debraj, Narayan, Umesh, Ratan, Modhu, Pallavi, Harshita, Minakshie, Prabhakar, Sagar, Deepak, Alamgir, Chetan, Atul, Sandeep, Jervis and all other junior research scholars for providing me a friendly ambiance in the hostel.

I would like to thank my brothers- Ricky, Parry, Harinder and Sukrit for being an emotional strength and supporting me spiritually throughout my life. I also would like to thank my Aunt for being a constant source of love, concern, support and strength all these years.

Lastly and most importantly, I would like to thank my parents and my grand-ma. No words are sufficient to describe their contribution to my life. I owe every bit of my existence to them. None of this would have been possible without their blessings, love, unconditional support and patience.

I would like to express my heart-felt gratitude to my family. I thank God for blessing me with the best family in the world.

Manjit Kaur

August, 2015

Basic Experiments Lab,

Institute for Plasma Research,

Gandhinagar

CONTENTS

SYNOPSIS.....	1
LIST OF FIGURES	9
LIST OF TABLES	14
1 CHAPTER: INTRODUCTION.....	15
1.1 Motivation.....	15
1.2 Basics of Complex (Dusty) Plasma	19
1.2.1 Dust Charging Processes	19
1.2.1.1 Collection of Charged Particles.....	19
1.2.1.2 Secondary Electron Emission.....	20
1.2.1.3 Thermionic Emission.....	21
1.2.1.4 Photoemission.....	21
1.2.1.5 Field Emission	22
1.2.2 Dust Surface Potential and Charge	22
1.2.3 Charging Time	25
1.2.4 Quasi-neutrality Condition	25
1.2.5 Characteristics Lengths.....	26
1.2.5.1 Plasma Debye Length.....	26
1.2.5.2 Dust Particle Radius (r_d).....	27
1.2.5.3 Inter-particle spacing (a).....	28
1.2.6 Characteristics Frequency.....	29
1.2.7 Coupling Parameter	30
1.2.8 Forces on the dust particles.....	32
1.2.8.1 Electric field force	32
1.2.8.2 Gravitation Force.....	33
1.2.8.3 Ion Drag Force.....	33
1.2.8.4 Neutral Drag force	37
1.2.8.5 Thermophoretic force	38
1.3 Overview of Earlier Works.....	40
1.4 Scope and Outline of the Thesis	43
2 CHAPTER: EXPERIMENTAL SET-UP.....	45
2.1 Experimental Set-up	45
2.1.1 Vacuum Vessel and Electrode Arrangement	45

2.1.2	Laser Sheet Formation Optics.....	48
2.1.3	Selection of Dust Particles.....	50
2.2	Camera.....	52
2.2.1	Principle of Operation.....	52
2.2.2	Selection of Camera and Accessories.....	53
2.2.3	Interfacing media.....	57
2.3	Data Analysis Using PIV Technique.....	59
2.4	Summary.....	60
3	CHAPTER: LANGMUIR PROBE FOR MEASUREMENTS IN DUSTY PLASMA AT HIGH PRESSURE.....	61
3.1	Issues Pertaining the Use of Single Langmuir Probe.....	61
3.2	Single Probe I-V characteristics.....	63
3.3	Theories for interpreting Langmuir probe characteristics.....	66
3.4	Probe design and construction.....	72
3.5	Specially Designed Langmuir probe circuit to prevent its contamination.....	74
3.6	Analysis of Single Langmuir probe I-V characteristics.....	82
3.7	Double Probe.....	85
3.8	Summary and conclusions.....	89
4	CHAPTER: DUST PARTICLE ROTATION.....	91
4.1	Observation of Dust Rotation.....	91
4.2	PIV analysis.....	96
4.3	Langmuir Probe Measurements.....	99
4.4	Probable Cause of Dust Rotation.....	100
4.5	Summary and Conclusions.....	105
5	CHAPTER: DOUBLE TORI.....	107
5.1	Observation of double torus.....	107
5.2	Theoretical background for Dust Vorticity Generation.....	109
5.3	Experimental Analysis.....	113
5.4	Summary and Conclusions.....	117
6	CHAPTER: EVOLUTION OF DUST ROTATION WITH DISCHARGE PARAMETERS.....	119
6.1	Evolution with Discharge Current.....	119
6.2	Evolution with Pressure.....	122
6.2.1	Number of Dust Particles.....	124

6.2.2	Dust Vortex Height above Cathode Surface	125
6.2.3	Dust Vortex Dimensions.....	128
6.2.4	Dust Particle Velocity	128
6.3	Summary and Conclusions	132
7	CHAPTER: CONCLUSIONS AND FUTURE SCOPE.....	134
7.1	Summary and conclusions	134
7.2	Future scope	138
	REFERENCES.....	140

SYNOPSIS

Present thesis reports experimental results and modelling of the poloidal rotation of mono-dispersed dust particles in toroidally symmetric structures in unmagnetized, inhomogeneous, cold cathode dc glow discharge dusty plasma. The evolution of dust rotation and its parametric variation with the discharge parameters has been studied in details and the underlying physics causing the rotation of dust particles has been determined. The major results established that a gradient in ion drag force arising due to a density gradient in the background plasma is the principal cause of rotation of dust particles.

Dusty plasmas are low temperature plasmas comprising of micron or sub-micron sized solid objects in addition to electrons, ions and neutrals. Due to the higher mobility of electrons than ions, the dust particles acquire a net negative charge on their surface. Depending upon their size as well as background plasma conditions, the dust particles can acquire charges of the order from $10^3 e^-$ to $10^5 e^-$. Due to the high charges acquired by the dust particles, they interact very strongly with each other as well as with the surrounding plasma species and increase the complexity of already complex plasma system. Their presence gives rise to many interesting phenomena with modified or entirely new collective modes of oscillation, instabilities and coherent nonlinear structures in plasmas, making the dusty plasmas a very interesting and challenging research topic.

Another important phenomenon that occurs in dusty plasma is of dust rotation in both presence and absence of external magnetic field. Dust rotation or so called “dust vortices” is one of the most interesting fundamental phenomena that have been observed in many laboratory as well as microgravity experiments. Different mechanisms can cause dust rotation due to subtle variations in the experimental conditions and although the vortices appear to be similar, their origins might be quite different. Dust particle rotation has been observed in many experiments with the application of external magnetic field. However, in many other experiments in laboratory plasmas as well as under microgravity conditions, dust particles rotation in absence of any external magnetic field has also been reported. Under microgravity conditions, the dust rotation or vortices [1] are usually observed (around the central dust free region called as “void”), due to the presence of a non-vanishing curl of the plasma

forces [2], such as ion drag force. In Laboratory experiments, if a biased probe [3] is immersed in plasma near the ordered crystalline structures, the dust particles start rotating because of the variation in local space-charge flux due to the ion wake associated with the probe. Gas convection either due to a thermal creep flow [4,5] along an inhomogeneously heated vessel walls at low pressures or due to a temperature gradient present [6] in the neutral gas at high pressures (\sim atmospheric) can also result into convective dust rotation. A space charge gradient [7,8] in an inhomogeneous plasma in the presence of a non-electrostatic force (such as gravity, ion drag force, etc.) orthogonal to it has also been attributed as the cause of generation of dust vortices. Also an asymmetry [9] in the ion drag force, near the edges of a metallic plate kept in plasma, may result into the formation of the dust vortices in a dc glow discharge. Hence, in most of the observations the role of the ion drag is found to be omnipresent. The importance of role played by ion drag in dust rotations has been further stressed in two recent publications. In one publication [10], it has been shown that under microgravity conditions, the dust vortices arise as a result of the balance between the driving torques from gradients of ion drag force function and dust charge and the loss of torque by friction on the neutral gas, while in the other publication [11], the dust cloud is assumed to behave like a fluid with weakly interacting dust particles. The dust fluid interacts with the vorticity of the dragging ion fluid and dissipative neutral fluid, resulting into stationary dust vortices.

The primary objective of the work described in this thesis is to study and understand the physics behind the formation of poloidal dust rotation by developing an experimental set-up equipped with advanced diagnostics such as, fast imaging with proper image processing tools and low noise Langmuir probe system capable of measurements at high pressure plasmas. Design, fabrication and operation of a state of art system for studying the rotation of charged dust particles in low temperature plasmas in the absence of any external magnetic field has been described in this thesis work. A low noise Langmuir probe system has been developed for proper and correct measurements of plasma parameters in high pressure plasma in presence of dust. A fast imaging camera systems with appropriate image analysing tools has been integrated to the plasma system for velocity and vorticity measurements of rotating dust cloud using Particle Image Velocimetry (PIV) technique. The cause of rotation of mono-dispersed dielectric microspheres (dust particles) in the system has been identified and modelled

successfully invoking the gradient of ion drag force generated due to radial density gradients present in the background plasma leading to dust rotation. The proposed model is rigorously tested by carrying out experiments in which multiple rotating dust vortices are produced. Parametric studies of the evolution of the dust rotation with the surrounding neutral density, plasma discharge current and other background plasma parameters have been carried out.

The work described in this thesis has two main parts (1) Development of Experimental set-up and Langmuir probe diagnostics and (2) Physics studies related to the formation of the poloidal dust rotation. The thesis comprises of seven chapters and has been organized as follows. The first chapter presents a brief introduction to dusty plasmas, the motivation and objective of the thesis and a brief review of some earlier works. The description of the experimental set-up that includes various sub-systems along with a special camera used to capture the dust dynamics during experiments is presented in second chapter. The second chapter also provides a brief description of the image analysis technique used to extract information about the dust rotation velocity and vorticity etc. The third chapter presents a brief review of the various theories that can be used to extract information about the plasma parameters from the I–V characteristics of Langmuir probe and discusses about the Langmuir probe system developed to work in dusty plasma environment at high pressures. The fourth chapter describes the observation of poloidal dust rotation in toroidally symmetric structures and provides a conjecture of the most probable cause behind rotation on the basis of the force analysis. The fifth chapter provides the experimental evidence supporting the model based ion drag gradient arising due to density gradient as the cause of dust rotation (as conjectured and elucidated in chapter 4). The dust dynamics is described using hydrodynamic formulations and it is observed that the vorticity of the dust fluid is in good agreement with that provided by the ion drag. Chapter six discusses the experiments performed related to the evolution of the toroidal dust structures with the background neutral gas density and discharge current. Finally, conclusions and future scopes of this thesis work are presented in the last (seventh) chapter.

After providing an introductory description of dusty plasmas as well as the review of some earlier studies in chapter **One**, the experimental set-up along with all its sub-systems is described in Chapter **Two**. The vacuum vessel is a stainless steel cylinder having four radial ports and two axial ports for evacuation and diagnostics. For

producing discharges, two parallel plate electrodes are being used. The upper electrode i.e., anode is inserted through the top port along with its electrical connections. The lower electrode is a specially designed electrode with a provision of placing concentric metallic ring / disk on its surface as per experimental requirements. It is used as a grounded cathode with the facility of active water cooling (for generating a controllable neutral gas temperature gradient in the discharge region) and is being inserted into the vacuum vessel through the bottom port. The experimental chamber is evacuated using a rotary pump through bottom port and gas is also fed through the same port using a needle valve to avoid any direct neutral flow due to its method of insertion in the system. The mono-dispersed dust particles made up of Melamine Formaldehyde having diameter of $6.48\ \mu\text{m}$ are used to prevent any size-dispersion related effects. These particles are uniformly spread over the desired region on the cathode surface. The axial ports have large diameter glass ports installed on them which provide wide viewing angles. The specialized sCMOS camera for recording the dust dynamics is installed on one of the axial ports and another one is used to view the dust particles through naked eyes or using a DSLR camera. We have obtained plasma discharge over a wide pressure range from $20\ \text{Pa}$ to $350\ \text{Pa}$ with discharge current in the range of $10\ \text{mA}$ to $50\ \text{mA}$. The neutral gas pressure and plasma discharge current are two main controlling parameters in our experiments. The formation of different types of structures likes low frequency oscillations, three-dimensional dust structures and vortices are obtained at different pressures in the same geometry.

1. *Manjit Kaur, et al.* (2015), “CPED – A test bed for studying dust vortices and other collective phenomena” (*Manuscript under preparation*).

In chapter **Three**, a detailed review of the previous works carried out at various pressure ranges and a low noise Langmuir probe system capable of working in dusty plasmas, is provided. When a Langmuir probe is kept in plasma, the dust particles get deposited on its surface and distort the current-voltage characteristics severely. To avoid the Langmuir probe contamination from dust deposition, it is maintained at a potential much less than the floating potential using a DC power supply so that the negatively charged micron sized particles are not attracted to it. To acquire the full I-V characteristics, single cycle triangular waveform is superposed on the DC bias at a frequency of $200\ \text{Hz}$ to ensure a very small time duration at which the probe bias is close to the plasma potential. As the dust plasma frequency is very small ($< 10\ \text{Hz}$), the

dust particles will not be able to respond to the positive probe potential within the small time duration and hence, the probe contamination can be avoided. At high pressures ($> 100 \text{ Pa}$), the ion-neutral collisions start affecting the probe collection due to destruction of the orbital motion of ions in the probe sheath and elastic scattering of ions due to collisions with neutrals.

1. *Manjit Kaur, et al.* (2015), “Low noise Langmuir probe system for high pressure dusty plasmas” (*Manuscript under preparation*).

In chapter **Four**, observation of dust cloud rotation [12] in parallel-plate DC glow discharge plasma is reported. The experiments are carried out at high pressures with a metallic ring placed on the lower electrode (cathode). The dust cloud rotates poloidally in the vertical plane near the cathode surface. This structure is continuous toroidally. Absence of magnetic field excludes the possibility of $E \times B$ induced ion flow as the cause of dust rotation. The rotational dust structures exist even with actively water cooled cathode. Therefore, temperature gradient driven mechanisms, such as thermophoretic force, thermal creep flow and free convection cannot be the cause behind the observed dust rotation. Langmuir probe measurement reveals the existence of a sharp density gradient near the location of the rotating dust cloud. A detailed force analysis is carried out which reveals that the dust particle rotation is occurring as a result of the non-conservative nature of the ion drag force. The gradient in the density, giving rise to a gradient in the ion drag force, is conjectured as the principal cause behind the rotation of dust particles.

1. *Manjit Kaur, Sayak Bose, P. K. Chattopadhyay, D. Sharma, J. Ghosh and Y. C. Saxena*, “Observation of dust torus with poloidal rotation in direct current glow discharge plasma”, **Phys. Plasmas** 22, 033703 (2015).

Chapter **Five** focuses on the deeper understanding of self-organized poloidally rotating mono-dispersed micro-particles in a toroidal geometry. Observations of two well-separated dust tori in unmagnetized parallel plate DC glow discharge plasma are reported in this chapter. A non-monotonic radial density profile, achieved by especially designed cathode structure using a concentric metallic disk and ring, is observed to produce double dust tori between cathode and anode. PIV analysis of the still images of these double tori shows oppositely rotating dust structures between the central disk and the ring. Langmuir probe measurements of background plasma shows non-uniform

plasma density profile between the disk and ring. Location and sense of rotation of vortices coincides with the location and direction of radial gradient in the ion drag force caused by radial density gradient. In order to establish this correlation further, the dust dynamics is described using hydrodynamic formulations assuming dust particles to be behaving as an incompressible fluid. The dust vorticity obtained from Navier-Stokes formulation shows two possible mechanisms charge gradient and ion drag gradient which can potentially drive vortex in the present set-up. Quantitative calculations using measured plasma parameters clearly indicate that the ion drag gradient is the main driving mechanism for the vortex generation in our experiments. These results corroborate that a radial gradient in the ion drag force directed towards cathode arising due to a density gradient is the principal cause of dust rotation.

1. *Manjit Kaur, Sayak Bose, P. K. Chattopadhyay, D. Sharma, J. Ghosh, Y. C. Saxena and Edward Thomas (2015), “Generation of multiple toroidal dust vortices by non-monotonic density gradient in direct current glow discharge plasma” (Manuscript submitted for publication).*

In chapter **Six**, the evolution of these rotating dust structures with discharge parameters such as the background gas pressure and the discharge current is reported. The dust particle velocity in the poloidal plane is found to increase considerably with an increase in the neutral gas pressure. The observations are made at constant discharge current in the absence of any directed neutral gas flow in the experimental region of interest due to method of gas insertion. This behaviour is just opposite to the general trend of decrease in dust velocity with an increase in neutral friction. With increase in discharge current too the dust particle velocity in the poloidal plane is found to increase but at a slower rate than that compared to the case of an increase in the neutral gas pressure.

1. *Manjit Kaur, et al. (2015), “On the evolution of poloidal dust rotation with ambient neutral density” (Manuscript under preparation).*

Chapter **Seven** summarises the content of the thesis and discusses the future scope of the current work.

Summary of the thesis:

1. **C**omplex **P**lasma **E**xperimental **D**evice (CPED) has been designed, fabricated and made operational from the individual component level for carrying out the physics studies related to the formation of dust vortices in presence of controlled

density gradients and in absence of any external magnetic field and neutral temperature gradients.

2. A low noise Langmuir probe system, capable of operating at high pressures, is developed for obtaining proper measurements of background plasma density and temperature in dusty plasma environment
3. Poloidal rotation of levitated mono-dispersed dust particles in toroidally symmetric structures is obtained in an unmagnetized dc glow discharge operating at high pressures and the observations are successfully modelled to extract the cause of these rotation.
4. The cause of dust rotation is explained on the basis of the presence of a sharp density gradient at the location of the rotating structure. The radial density gradient gives rise to a radial gradient in the ion drag force directed towards the cathode surface which acts as a torque on the dust structure making it rotate. The velocity profile of dust particles is measured using Particle Image Velocimetry (PIV) techniques, showing a rotating rigid body like behaviour of the rotating structures.
5. Ion drag force as the cause of formation of rotating structure is further verified by conducting experiments with by introducing additional density gradient leading to the formation of additional rotating structure at the location of the second gradient.
6. The direction of rotation of the dust particles is found to be in accordance with the direction of the density gradient.
7. The dust particle dynamic is studied using hydrodynamic formulations. The estimated values of dust vorticity (obtained from these formulations) due to a gradient in the ion drag force is found to be well in agreement with the observed value of the dust vorticity.
8. Parametric variations show that the dust particle rotation velocity increases considerably with increasing the background gas pressure. However, it increases slowly with increasing the discharge current at constant pressure.

References:

- [2] M. R. Akdim and W. J. Geodheer, Phys. Rev. E 67, 056405 (2003).
- [3] D. A. Law, *et al.*, Phys. Rev. Lett. 80, 4189 (1998).

- [4] T. M. Flanagan and J. Goree, Phys. Rev. E, 80, 046402 (2009).
- [5] S. Mittic, *et al.*, Phys. Rev. Lett. 101, 235001 (2008).
- [6] M. Schwabe, *et al.*, New Jour. of Phys. 13, 083034 (2011).
- [7] O. S. Vaulina, *et al.*, Plas. Phys. Rep. 30, 918 (2004).
- [8] Samarian, *et al.*, Physica Scripta T98, 123 (2002).
- [9] G. Uchida, *et al.*, Phys. Plasmas 16, 053707 (2009).
- [10] Tim Bockwoldt, *et al.*, Ply. Plasmas 21, 103703 (2014).
- [11] Modhuchandra Laishram, *et al.*, Phys. Plasmas 21, 073703 (2014).
- [12] Manjit Kaur, *et al.*, Phys. Plasmas **22**, 033703 (2015).

LIST OF FIGURES

Figure 1.1: Schematic of the various dust charging mechanisms.....	21
Figure 1.2: Image a) shows the case when the dust particles are separated by a large distance and do not interact with each other, i.e., $a > \lambda_D$, and b) shows the case of dust particles interacting with each other, i.e., $a < \lambda_D$	28
Figure 1.3: The above images correspond to an example of: a) a solid state where the dust particles are bound very strongly to each other for $\Gamma \gg 170$, b) a liquid-like state where the dust coupling is weak i.e., $1 < \Gamma < 170$, and c) the gaseous state where the dust particles do not interact with each other for $\Gamma \ll 170$	31
Figure 2.1: Front view of the experimental system with various sub-parts attached to it.	46
Figure 2.2: Three-dimensional view of the experimental system. The camera is directed in the x-direction, vertical Laser sheet enters the experimental region of interest in the y-direction and z represents the (vertical) direction of electrode axis.	46
Figure 2.3: (a) shows the photographs of the anode covered using BN cup and (b) represents the specially designed water cooled cathode.....	47
Figure 2.4: The image of a sample of melamine formaldehyde (MF) condensation resin particles being used in experiments having average diameter as $6.48 \mu\text{m}$, obtained using a microscopic shows that the dust particle are spherical in nature (to a very good approximation). The size distribution is extremely narrow (standard deviation is $0.1 \mu\text{m}$).	51
Figure 2.5: Typical arrangement showing the different steps of PIV techniques.....	60
Figure 3.1: Typical I-V characteristics of a single Langmuir probe.....	64
Figure 3.2: The schematic showing the orbital motion of the ion inside sheath region in a collisionless regime. The sheath boundary is well-defined and outside the sheath region, the plasma is assumed to be perfectly neutral.	67

Figure 3.3: The schematic shows the influence of ion-neutral collisions on the probe collection current; a) represents the destruction of orbital motion of the ions inside the sheath leading to an increase in the collection current whereas, b) represents the elastic scattering of ions inside the sheath leading to a decrease in the probe current.	68
Figure 3.4: The different Probe theory regimes for plasma density determination under different operating conditions.	70
Figure 3.5: Picture of the Single Langmuir probe employed for determining the plasma parameters.	74
Figure 3.6: Light microscope image of Langmuir probe (a) before use and after use (b) in complex plasma [79].....	75
Figure 3.7: A Single cycle of triangular wave superposed on the DC bias applied to the Langmuir probe.....	75
Figure 3.8: The effect of dust contamination on the ion saturation part of the probe I-V characteristics under similar discharge conditions	77
Figure 3.9: (a) A typical Langmuir probe circuit, (b) Equivalent circuit of the Langmuir probe circuit, (c) Equivalent probe circuit after neglecting cable inductance (L_c), cable resistance (r_c) and cable conductance (G_c).	78
Figure 3.10: Various arrangement of a triax cable for carrying out the Langmuir probe current measurements.	79
Figure 3.11: The schematic of the Langmuir probe circuit for measuring the probe IV characteristics.....	80
Figure 3.12: Circuit of a High Voltage amplifier.	82
Figure 3.13: Langmuir probe characteristics at a pressure of 133 Pa and discharge current as 20 mA.....	83
Figure 3.14: Flow chart for the determination of plasma density (n_i) at a pressure p using “modified TALBOT and CHOU theory”.....	84

Figure 3.15: A graph of the double Langmuir probe at a height of 9.5 mm above the surface of cathode.	88
Figure 3.16: Radial profiles of electron temperature at different heights at a discharge current of 25 mA and an operating pressure of 105 Pa	89
Figure 4.1: The diametrically opposite poloidal cross-sections of the dust torus in the vertical $r - z$ plane at different pressures; (a) 70 Pa, (b) 76 Pa, (c) 100 Pa, and (d) 110 Pa, respectively. The laser sheet is passed along the diameter of the cathode through the side radial port and the camera is placed perpendicular through the axial port.....	92
Figure 4.2: Top view of the arrangement of the camera and the vertical laser sheet, scanned horizontally to capturing the whole area of the torus.	94
Figure 4.3: The different cross-sections of the dust toroidal structure illuminated by the vertical laser sheet when the cathode diameter is scanned from centre towards its end.	95
Figure 4.4: A schematic of the co-ordinate system where z represents the direction opposite to g , φ represents the toroidal direction and θ represents the direction of the poloidal rotation of the dust particles above the metallic ring.....	96
Figure 4.5: a) The still image of the poloidal cross-section of the dust torus taken with the help of sCMOS camera, and b) The dust particle velocity profile in the poloidal cross-section.....	97
Figure 4.6: Radial density profiles a) in the absence of dust particles and b) in the presence of dust particles at two different heights above the surface of cathode.....	100
Figure 4.7: A two-dimensional schematic of the experimental set-up, clearly showing the evacuation and gas insersion through the bottom port.....	102
Figure 4.8: The still images taken with the help of sCMOS camera at a pressure of 124 Pa and discharge current of 26 mA represents; (a) the case when the rotary pump as well as the needle valve are disconnected to the vacuum vessel whereas (b) the case when both of these are connected to the vacuum vessel.....	104

Figure 5.1: The picture shows the concentric metallic disk placed on the cathode surface along with the concentric metallic ring. The annular region between the ring and disk is covered by MF dust particles..... 107

Figure 5.2: (a) A still Image showing the poloidal cross-sections of the double tori captured by a DSLR camera, illuminated by a laser sheet along the diameter of both the tori. Here, “I” and “II” represents the cross-section of the dust torus formed at the edge of the metallic disk and near the metallic ring, respectively. This image shows the radial extent of the vertical plane from centre to ~ 60 mm away from centre. (b) The radial profile of the plasma density at a height of 10 mm above the cathode surface at a pressure of 133 Pa and discharge current as 20 mA in the presence of a concentric metallic disk and ring..... 108

Figure 5.3: Radial profiles of a) dust charge and dust charge gradient and, b) ion drag force and its gradient at a height of 10 mm above the surface of cathode..... 114

Figure 5.4: (a) The image of the poloidal cross-sections of the double dust tori while the laser sheet is passed along the diameter of both tori captured with the help of sCMOS camera at an exposure time of 4.9 ms in plasma formed with pressure of 133 Pa and discharge current as 20 mA. The spatial resolution of the image is as 1 pixel= $38.9 \mu\text{m}$. (b) Velocity vectors showing the direction of rotation of the dust particles is obtained using Davis software; the colour bar shows the value of dust velocity in cms^{-1} . The left cloud shows the dust rotation in anti-clockwise direction and right hand cloud in the clockwise direction. (c) shows the vorticity profile associated with the rotation; the colour bar shows the value of vorticity in s^{-1} 116

Figure 6.1: The still images taken with the help of sCMOS camera show the evolution of the poloidal cross-section with the a variation in the discharge current; a) $I_{\text{dis}} = 20$ mA, Voltage drop across electrodes (V_{drop})= 254 V , b) $I_{\text{dis}} = 25$ mA, $V_{\text{drop}} = 258 \text{ V}$, c) $I_{\text{dis}} = 30$ mA, $V_{\text{drop}} = 260 \text{ V}$ and d) $I_{\text{dis}} = 35$ mA, $V_{\text{drop}} = 262 \text{ V}$ for a background pressure of 156 Pa. On the right hand side, the images with primes show the velocity profiles of the dust particles corresponding to different values of discharge current; different colours in the colorbar show the different magnitudes of dust velocity in cms^{-1} 120

Figure 6.2: Langmuir probe measurements show an increase in the radial density gradient with an increase in the discharge current..... 121

Figure 6.3: The variation in the poloidal cross-section of the dust torus with an increase in the background pressure at a discharge current of 25 mA: a) 92.9 Pa, b) 126 Pa, c) 184 Pa, d) 196 Pa, e) 213 Pa and f) 220 Pa. The colorbar shows the velocity in cm s^{-1}	123
Figure 6.4: The variation in the poloidal cross-section of the dust torus with an increase in the background pressure at a discharge current of 37 mA: a) 84 Pa, b) 90.5 Pa, c) 115 Pa, d) 124 Pa, e) 205 Pa and f) 253 Pa. The colorbar shows the velocity in cm s^{-1}	125
Figure 6.5: The decrease in dust particle cloud above the cathode with an increase in the background gas pressure at a fixed discharge current of (a) 25 mA and (b) 37 mA. ...	126
Figure 6.6: The evolution of the dust particle vortex dimensions with an increase in the background gas pressure at a fixed discharge current of (a) 25 mA and (b) 37 mA. ...	127
Figure 6.7: Increase in the particle velocity in the dust cloud with an increase in the background gas pressure at a fixed discharge current of (a) 25 mA and (b) 37 mA. ...	129
Figure 6.8: The radial variation in the plasma density with increase in pressure at a discharge current of 25 mA. The probe measurements are taken at a height of ~ 10 mm above the cathode surface.	130

LIST OF TABLES

Table 1.1: Order of magnitudes of different forces experienced by a levitated dust particle in plasma.	40
Table 2.1: The details of the cylindrical lens used for converting the laser beam into a vertical plane.	50

1 CHAPTER: INTRODUCTION

This chapter starts with a very general motivation for the study of dust vortices in section 1.1. Thereafter, in section 1.2, some relevant topics of this subject and the basic concepts of dusty plasma are presented which are essential for the understanding of the experimental results and physics presented in this dissertation. In section 1.3, the review of the relevant works on dust rotation has been summarized. Finally, in section 1.4, the scope and the structure of this thesis are provided.

1.1 Motivation

In 1928, Langmuir, for the very first time, used the term “Plasma” to describe the inner region of a glowing ionized gas produced by means of an electric discharge in a tube. Conventionally, plasmas are quasi-neutral systems of electrons, ions and neutral particles (atoms, molecules), exhibiting collective behaviour. In most cases, plasma coexists with the micron sized charged dust particles, be it space plasma or laboratory plasma. Thus, a mixture of charged dust particles, electrons, ions and neutrals is called as “Dusty plasma” where the charged particles exhibit collective behaviour.

Initial interest in dusty plasmas arose in the field of astrophysics as dust particles are present in many astrophysical environments [1] such as Saturn's rings, cometary tails, interstellar medium, nebulae, etc. These dust particles present in space plasmas can acquire large charges and have been found to determine many properties of interstellar media, stars and planet formation regions, properties of planetary rings [2,3], cometary tails, etc. Another field of interest in dusty plasmas is the semiconductor industry. The dust particles are very much unwanted in semi-conductor chip industries because they destroy/deteriorate the quality of the chips [4]. Dust appears to be a critical issue in the

development of microelectronics. Another area showing high interest in dusty plasmas is the solar cell industry. Incorporation of nanometer-sized dust particles in the amorphous silicon film increases the stability of the solar cells substantially [5]. In catalysis too, the deposition of small clusters of palladium (a good catalyst) on the particle surface grown in plasma results in efficient cauliflower morphology for catalysis [6]. Apart from their industrial impact, dusty plasmas appear to be of fundamental interest too. Dusty plasma is an analogue for molecular physics where each dust particle represents a molecule. Due to their bigger sizes as compared to the electrons and ions, the dust particles have very high masses and very low mobility that present an advantage of direct imaging. They can be illuminated using a low power laser and can be easily seen through naked eyes and captured using a visible camera. Their individual positions [7] as well as their velocities [8] can be measured to a great degree of accuracy using the still images recorded by the camera. Therefore, dusty plasma offers an excellent medium for investigating many interesting and important phenomena at a macroscopic level that conventionally occur on a microscopic scale in molecular or solid state physics.

Due to the presence of high charges present on dust particles, they interact very strongly with each other. Thus, they possess large electrostatic Coulomb energy which, in most cases, exceeds their thermal energy. In complex plasma due to the strong dust-dust coupling, it is possible to observe transitions from a disordered gaseous-like phase to a liquid-like phase and to ordered structures of dust particles – called as plasma crystals. The charge acquired by the dust particles is not a constant quantity but varies with time due to the time variation in the surrounding plasma parameters. Therefore, the dust charge becomes another dynamical variable that distinguishes complex (dusty) plasma from conventional plasma (where the particle charge does not vary with time).

In 1986, Ikezi [9] predicted the possibility of dust crystallization in a non-equilibrium gas discharge plasma which was then achieved in RF discharge [10,11,12,13] as well as in DC glow discharge [14] in ground-based experiments. The experimental discovery of plasma crystals triggered an enormous increase of interest in the field of complex plasmas. Presently, it covers various fundamental aspects of plasma physics, hydrodynamics, kinetics of phase transitions, nonlinear physics, solid state physics, as well as astrophysics. Extensive experimental, theoretical and simulation work has been carried out to understand the different aspects of complex (dusty) plasmas. Dusty plasmas provide an excellent opportunity to study the charging mechanism of dust particles, waves and instabilities, crystal formation, vortex formation etc.

The observation of dust plasma crystals on ground-based experiments encouraged the researchers to perform experiments under the conditions where gravity does not play a significant role. One such initiative was to do experiments under microgravity conditions. The results of the sounding rocket (TEXUS) experiments with around *6 min* of microgravity time were reported [15] in 1999, which lead to the establishment of “Plasma Crystal” (PKE-Nefedov) laboratory under the Russian-German Scientific Cooperation program for doing experiments onboard the International Space Station (ISS). The main objectives of PKE-Nefedov included the investigation of dusty plasma crystals, phase transitions, wave phenomena, properties of boundaries between different plasma regions, etc. in a three-dimensional isotropic dusty plasma at the kinetic level under microgravity conditions. In these experiments, a dust-free region— called void (i.e., no dust particles present) is observed in the central region of the discharge. The void is separated by a sharp boundary from the regions containing dust particles. Away from the central axis, there are toroidally symmetric vortices in the absence of any external magnetic field. The dust free regions, i.e., voids get formed due

to the competition of electrostatic force arising due to the electric field in the discharge, pointed towards the centre and the ion drag force which pushes the dust particles away from the centre (towards the periphery) [16,17]. However, the dust vortices are formed due to the non-conservative nature of the plasma forces arising due to the spatial variation in electron temperature and plasma density [18]. In complex (dusty) plasmas, the dust particles are subject to many conservative and non-conservative forces, such as force due to gravity and electric field, ion drag force, neutral drag force and thermophoretic force. Together, all these forces make their dynamics quite complicated and results in many interesting phenomena including dust rotation. The aim of this thesis is to give an insight about the mechanisms of dust rotation, with and without void at the centre.

The study of dust vortices in complex (dusty) plasmas continues to be and has been an active area of research during past several years. Vortices occur in a wide range of physical phenomena in nature. Smoke rings, whirlpools, tornadoes, hurricanes, the Great Red Spot of Jupiter and Saturn's hexagon formed at its north pole are some of the examples of vortices observed in nature. These are the regions within a fluid (liquid, gas or plasma) where the flow spins around an imaginary straight or curved axis. The dust vortices occurring in complex (dusty) plasma experiments are an ideal test bed for studying turbulence in fluids with low Reynolds number. The studies related to dust vortex formation are very important and would lead to proper understanding of many physical phenomena such as fluid flow through a regular porous medium [19], and in the flow of elastic polymer solutions [20]. Also in dusty plasmas, the dynamics of appearance of vortices can be analysed on kinetic level which is of practical importance for the physics of vortices when these are created by the flows around an obstacle.

1.2 Basics of Complex (Dusty) Plasma

In the following, some of the very fundamental properties of dusty plasmas starting with the mechanisms of dust charging, its characteristic lengths, frequencies, quasi-neutrality, coulomb coupling parameter and basic forces acting on the dust particles are discussed.

1.2.1 Dust Charging Processes

When the dust particles are inserted in plasma constituting electrons, ions and neutrals, the dust particles act as small probes, collect charged particles from the plasma and become positively or negatively charged depending upon the charging processes involved. For the sake of simplicity, we consider the case of an isolated dust grain that means the dust shielding length (Debye length) less than the inter-dust separation is considered, as it is easier to discuss the charging phenomena for single particles than many particles at a time. The different dust charging processes have been discussed below:

1.2.1.1 Collection of Charged Particles

Let us consider a micron-sized neutral dust particle immersed in unmagnetized cold plasma whose constituents are electrons and ions. The electrons, because of their lower masses possess much larger thermal speeds than the ions and reach the dust surface earlier than the ions. Thus, the dust particle acquires much more electrons than the ions, and as a result its surface potential becomes negative with respect to the rest of the plasma. This negative potential repels the further coming electrons and attracts the ions so that the electron flux towards its surface diminishes and the ion flux increases. Eventually, the negative potential at the dust grain surface becomes large enough in magnitude to equalize the rate at which the electrons and ions hit the surface. As a

result, a state of dynamical equilibrium is reached such that the net current at the dust grain surface becomes zero. This is basically a phenomenon of sheath formation at the dust particle surface. However, the charge of the dust grain surface is never constant. It always keeps on fluctuating which is a one of the very interesting topics of research in Dusty Plasmas.

1.2.1.2 Secondary Electron Emission

The energetic primary plasma particles may bombard the dust grain surface and may cause a release of secondary electrons from the dust surface. This process can occur in two ways: (i) by electron impact (ii) by ion impact.

When an energetic electron approaches a dust grain surface: (i) it may be scattered/reflected by the dust grain before it enters into the dust surface, (ii) it may enter into the dust and stop immediately, (iii) it may enter into the dust particle, interact with the scattering centre and pass a part or all of the dust material, wherein it may lose its energy. A portion of this energy can go into exciting other electrons which in turn escape from the dust surface.

If the ions approaching the dust particle have low kinetic energies below 1 keV , they will be neutralized by the electrons which tunnel through the potential barrier of dust surface. The potential energy released in neutralization of ions will excite additional electrons which can then be emitted from the dust surface. When the ions have enough energy above 10 keV , the secondary electron yield due to ion impact will be substantially larger than unity. The behaviour of such high energy ions falling on the dust surface may be same as that of the electrons falling on it.

1.2.1.3 Thermionic Emission

When a dust surface is heated to a high temperature, electrons or ions may be thermionically emitted from its surface, as shown in Figure 1.1. The thermionic emission may be induced by Laser heating or thermal infrared heating or by hot filament surrounding the dust particles. Generally, this process charges the dust positively.

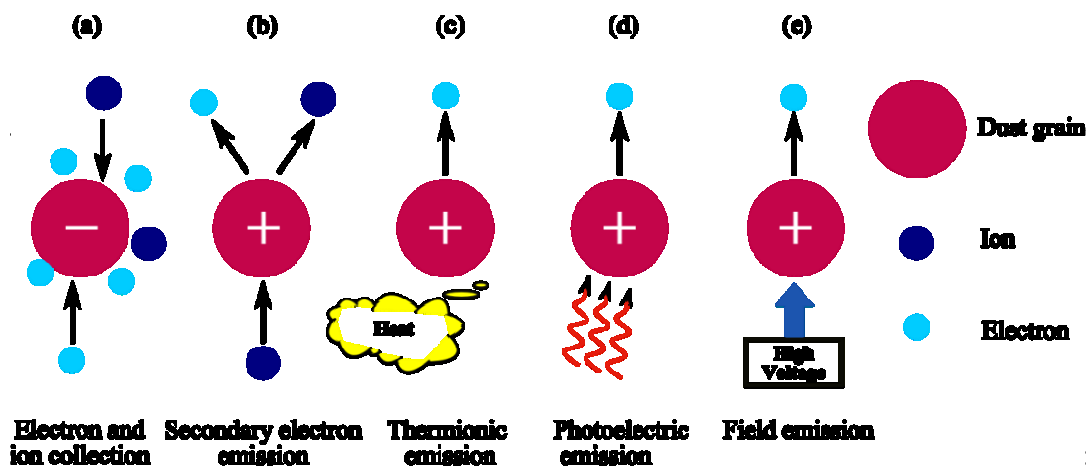


Figure 1.1: Schematic of the various dust charging mechanisms.

1.2.1.4 Photoemission

Photons falling on the dust grain surface, with energy ($h\nu$) larger than the work function of the dust grain surface, may also eject photoelectrons from its surface. This photoemission of electrons depends on:

- (i) Wavelength of the incident photons
- (ii) Surface area of dust
- (iii) Properties of the dust surface

This mechanism also contributes to make the dust particles positively charged.

1.2.1.5 Field Emission

Sometimes, micron or submicron sized dust particles may acquire a very high negative (or positive) potential and emit electrons (or ions) from their surface due to field emission. Generally, the onset of electron emission from the dust surface occurs when the electric field is of the order of 10^6 Vm^{-1} .

1.2.2 Dust Surface Potential and Charge

Let us consider that the dust particles are immersed in unmagnetized cold plasma. Initially the ion current is very small as compared to the electron current because of larger masses and hence smaller mobility of ions as compared to electrons which results in negative charge acquired by the dust surface. This further increases the ion current until the net current to the dust surface becomes zero.

Due to the higher mobility of the electrons, the dust particles generally get negatively charged and their surface potential becomes roughly proportional to the electron temperature; i.e.,

$$\phi_d = -\alpha T_e/e, \quad (1.1)$$

where α is a numerical coefficient of the order unity. The traditional and apparently the most frequently used method for estimating the surface potential of a floating particle, when kept in plasma, is by using the Orbital Motion Limited (OML) theory, where collection cross-sections for ion-dust and electron-dust collisions are determined from the conservation of angular momentum and energy over corresponding (usually Maxwellian) velocity distribution. OML theory is applicable as long as the dust particle

radius is small compared to its Debye length. In case of OML theory, the value of α lies in the range of 2 – 4. However, OML theory does not take into account the effect of ion-neutral collisions which predominates at moderate and higher pressures. As the ion collisionality increases ($\ell_i/\lambda_D \geq 10$), the ion-neutral collisions increase the ion flux towards the surface of the dust particle due to the destruction of the orbital motion of ions. As a result of it, the value of α starts decreasing and reaches a minima when the ion-neutral collision mean free path, ℓ_i becomes of the order of the plasma screening length, λ_D . Here, λ_D represents the dusty plasma Debye length which is approximately equal to the ion Debye length.

As the ion-neutral collisionality increases further, the ion-neutral collision mean free path becomes smaller than the plasma Debye length ($\ell_i/\lambda_D < 1$). At this stage, ion motion becomes mobility-limited whereas, the electrons still can be considered collisionless. In this regime, the ion mobility is suppressed by their collisions with neutrals, ion flux to the dust particle surface decreases, and α increases with increasing ion collisionality. However, the magnitude of α does not keep on increasing as the electron transport to the particle surface also becomes collisional after a certain pressure value. Both electron and ion fluxes to the dust particle surface are then equally reduced by their collisions with neutrals, and the dust particle potential saturates to a value which is independent of plasma collisionality. This “fully collisional” regime is, however, beyond the scope of the present work and hence, will not be discussed here.

Using the electric potential around the dust particle to follow the Debye Huckel form, the expression for the ion flux in the weakly collisional limit [21] is given by

$$I_i^{wc} \cong \sqrt{8\pi} r_d^2 n_0 v_{Ti} \left[1 + \alpha\tau + 0.1(\alpha\tau)^2 \left(\lambda/\ell_i \right) \right]. \quad (1.2)$$

In an isotropic plasma with $T_e \gg T_i$, we have $\lambda_D \approx \lambda_{Di} = \sqrt{T_i / 4\pi e^2 n_i}$.

The electrons can be assumed collisionless due to the higher values of electron-neutral mean free path length than the plasma screening length. Thus, the electron flux can be determined using the OML approach which is given by

$$I_e = \sqrt{8\pi} r_d^2 v_{Te} n_i \exp(-\alpha). \quad (1.3)$$

The dust surface potential is calculated by equating the electron and ion flux to the surface of the dust particles. In the equilibrium state, when the dust surface has attained a constant potential, the net current to the dust surface will be zero. By equating both the electron and ion fluxes, at $T_e = 2$ eV, $T_i = 0.03$ eV, $n_i = 3 \times 10^9 \text{ cm}^{-3}$, $\ell_i = 22.6$ μm , the value of α comes out to be 1.158.

After equating both fluxes, the value of ϕ_s becomes $1.158 T_e / e$. In ambient plasma with screening length as λ_D , the capacitance [22] of the dust particle can be estimated as follows

$$C_d = 4\pi\epsilon_0 r_d \left(1 + \frac{r_d}{\lambda_D}\right). \quad (1.4)$$

From equation (1.1) to (1.4), the formula for charge acquired by the dust particle becomes

$$|Z_d| = 4\pi\epsilon_0 r_d \alpha \left(1 + \frac{r_d}{\lambda_D}\right) \frac{T_e}{e}. \quad (1.5)$$

Therefore, the charge on the dust particle (Z_d) depends upon its size and number density, background plasma density and electron and ion temperature. It is estimated to

be typically $8 \times 10^3 e^-$ for Argon discharge with a typical electron temperature of $2 eV$ and plasma density $3 \times 10^9 cm^{-3}$ for a dust particle size of $6.48 \mu m$ at a pressure of $133 Pa$.

1.2.3 Charging Time

Charge on a dust particle is not fixed, it varies with time. This fluctuation can be because of varying plasma parameters of the surroundings. Charging time, τ_{ch} , indicates how rapidly a particle's charge can vary, when plasma conditions vary. It has been observed that hypothetically dust particle has no charge but after being immersed in plasma, its charging time can be defined as the time required for a particle's charge to reach a fraction $(1 - e^{-1})$ of its equilibrium value [23]. Like a capacitor, dust particles also take some time to get fully charged. The charging time varies inversely with plasma density and particle size.

1.2.4 Quasi-neutrality Condition

In equilibrium (in the absence of any external force), the net electric charge in a dusty plasma is zero. Therefore, the equilibrium quasineutrality condition in dusty plasma is

$$q_i n_i = q_e n_e + q_d n_d, \quad (1.6)$$

where n_i , n_e and n_d are the unperturbed number density of ions, electrons and dust grains respectively. $q_i = Z_i e$ is the ion charge. For the sake simplicity, let us consider the case of singly charged ions for which $Z_i = 1$. For the case of dust particles, $q_d = Z_d e$ for positively charged dust grain and $q_d = -Z_d e$ for negatively charged dust grain. Now let us take the case of a negatively charged dust grain where equation (1.6) can be written as

$$en_i = en_e + Z_d en_d,$$

$$\frac{n_e}{n_i} = 1 - Z_d \frac{n_d}{n_i}. \quad (1.7)$$

In equation (1.7), the term $Z_d \frac{n_d}{n_i}$ i.e., the ratio of dust charge density to ion density, is defined as the Havnes' parameter P . When $P \ll 1$, i.e., $Z_d n_d \ll n_i$, the number density of dust grain particles is very small as compared to the number density of ions, the charge and floating potentials approach the values for an isolated particle. Hence, the dust particles can be treated as 'Isolated'. Whereas, in the opposite limit, i.e., $P > 1$, there are enough number of dust grains. Due to their large number density, they can interact with each other and do not remain isolated, can be called as non-isolated dust particles. As a result, the dust particle charge and floating potential are significantly diminished.

1.2.5 Characteristics Lengths

It is possible to define three different scale lengths for a combined dust and plasma mixture, a) plasma Debye length, b) dust grain radius, and c) average inter-dust separation. The details of these characteristics are given below:

1.2.5.1 Plasma Debye Length

A fundamental characteristic of plasma is its ability to shield the electric field of an individual charged particle or of a surface that is at a non-zero potential. This shielding of electrostatic fields is a consequence of the collective effects of the plasma particle. Let us consider plasma consisting of ions, electrons and charged dust grains and applying an electric field by inserting a charged ball in the plasma. Now the plasma will try to shield this electric field. If the ball is positively charged then a cloud of electrons and dust grains (if they are negatively charged) will surround the ball. In case of cold

plasmas, there would be just as many charges in the cloud as in the ball. Poisson's equation can be written as

$$\nabla^2 \varphi = 4\pi(en_e - en_i - q_d n_d),$$

$$\nabla^2 \varphi = \left(\frac{1}{\lambda_{De}^2} + \frac{1}{\lambda_{Di}^2} \right) \varphi,$$

$$\nabla^2 \varphi = \frac{1}{\lambda_D^2} \varphi,$$

where

$$\lambda_D = \frac{1}{\sqrt{\left(\frac{1}{\lambda_{De}^2} + \frac{1}{\lambda_{Di}^2} \right)}} \quad (1.8)$$

is a measure of the shielding distance or the thickness of the sheath around the dust particle. For a dusty plasma with negatively charged dust grains, we have $n_e \ll n_i$. The loss of electrons on the dust has to be compensated by increased ionisation due to strengthened electron acceleration. Thus, the presence of dust leads to an increase in electron temperature as compared to the dust free case to compensate the electron losses i.e. $T_e > T_i$ which leads to $\lambda_{De} \gg \lambda_{Di}$. Accordingly, we have $\lambda_D \cong \lambda_{Di}$. It means that λ_D for such dusty plasmas can be determined by the temperature and the number density of the ions. However, when the dust particles are positively charged i.e. $n_e \gg n_i$ and $T_e \cong T_i$ or where $T_e n_i \ll T_i n_e$ we have $\lambda_{De} \ll \lambda_{Di}$ which results into $\lambda_D \cong \lambda_{De}$. That means Debye length of such a positively charged dust grain containing dusty plasma can be determined by the temperature and the density of the electrons.

1.2.5.2 Dust Particle Radius (r_d)

The dimensions of the dust particles are an important characteristic length in dusty plasma. The dust particle size determines the magnitude of the dust charge as $Z_d \propto r_d$

and the collision cross-section between various species present in the plasma. It is also a crucial parameter in deciding the magnitude of various forces acting on the dust particles such as gravitational force ($F_g \propto r_d^3$), electrostatic forces ($F_E \propto r_d$), etc. For example, for a micron or submicron size particle the exact balance between downward gravitational force and upward electrostatic force due to electric field existing in the plasma sheath region decides the height at which the particle will levitate and thus, determines the equilibrium characteristics of the dust cloud.

1.2.5.3 Inter-particle spacing (a)

As the name indicates, it is the minimum distance between one dust particle centres to another dust particle centre. The coulomb field is a long range field and is usually screened in plasmas. The screening substantially changes the dust-dust interaction. Assume, for example that the coulomb field of the dust particles is completely screened upto (some sphere) the distance λ_D . Then, the strong interaction is absent outside this sphere and the dust particles “feel” each other only when the distance between them is equal to or less than the screening distance. Otherwise they behave as a kind of “hard sphere” “not interacting until they touch (contact) each other.

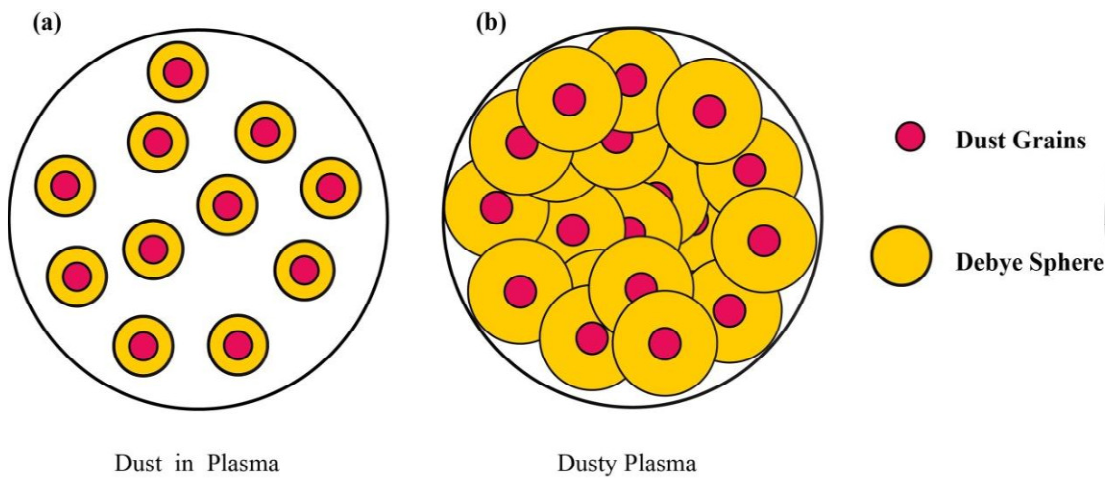


Figure 1.2: Image a) shows the case when the dust particles are separated by a large distance and do not interact with each other, i.e., $a > \lambda_D$, and b) shows the case of dust particles interacting with each other, i.e., $a < \lambda_D$.

Depending upon the relative values of these three characteristic lengths, the plasma constituting dust particles can be termed as either “dust in plasma” or “dusty plasma”, as shown in Figure 1.2. So, the case $r_d \ll \lambda_D \ll a$, in which charged dust particles are considered as a collection of isolated hard spheres, corresponds to “dust in plasma” while in the situation $r_d \ll a \ll \lambda_D$ where the dust particles participate in the collective behaviour, corresponds to “dusty plasma”.

1.2.6 Characteristics Frequency

Being quasi-neutral in nature, a slight displacement of particles from their equilibrium position in dusty plasma will result into a space charge field which pulls the particles back to their equilibrium positions to restore the original charge neutrality. But their inertia causes them to overshoot and again pulled back to their equilibrium positions by space charge field of opposite polarity. This gives rise to (electrostatic) oscillations of dust particles around their equilibrium positions. In such a case the system of electrostatic oscillations of the dust particles can be described by the continuity equation

$$\frac{\partial n_d}{\partial t} + \nabla \cdot (n_d v_d) = 0, \quad (1.9)$$

the momentum equation

$$\frac{\partial v_d}{\partial t} + (v_d \cdot \nabla) v_d = -\frac{q_d}{m_d} \nabla \varphi_d, \quad (1.10)$$

And the Poisson's equation

$$\nabla^2 \varphi_d = -4\pi q_d n_d. \quad (1.11)$$

Assuming the dust oscillations to possess infinitely amplitude and all charged particles to be at rest under equilibrium conditions, the above system of equations can be linearized to get

$$\frac{\partial^2}{\partial^2 t} \nabla^2 \varphi_d + 4\pi \frac{n_d q_d^2}{m_d} \nabla^2 \varphi_d = 0. \quad (1.12)$$

Integrating the above equation (1.12) twice with respect to space $r(x, y, z)$, we obtain

$$\frac{\partial^2 \varphi_d}{\partial^2 t} + \omega_{pd}^2 \varphi_d = 0, \quad (1.13)$$

where

$$\omega_{pd}^2 = \frac{4\pi n_d q_d^2}{m_d} = \frac{n_d q_d^2}{\epsilon_0 m_d}, \quad (1.14)$$

is the dust plasma frequency with which the dust particles with charge $q_d (= Z_d e)$ oscillate about their respective equilibrium positions. Like electron and ion plasma frequency, dust plasma frequency also depends upon the charge acquired by the dust particles in plasma, their mass and number density. For an inter-dust separation (a) of 0.5 mm , i.e., $n_d = a^{-3} = 8 \times 10^9 \text{ m}^{-3}$, the dust-plasma frequency comes out to be 13.21 Hz . Thus, it is clear that the dust plasma frequency is the much smaller than the electron plasma frequency (of the order of MHz) and ion plasma frequency (\sim few hundreds of kHz). Due to the bigger size ($\sim \mu\text{m}$) of the particles and their slower time scales, they can be seen through naked eyes and their dynamics can be easily captured and studied using a normal visible camera.

1.2.7 Coupling Parameter

Due to the high charges acquired by each dust particle in plasma, they interact very strongly with each other and give rise to many new phenomena. Crystalline structure

formation is one such phenomenon which generally occurs in plasma when the interaction energy between the adjacent dust particles exceeds their thermal energy. Thus, a dimensionless parameter is defined in this regard for providing information about the extent of coupling between the particles and is called as the Coulomb Coupling parameter (Γ).

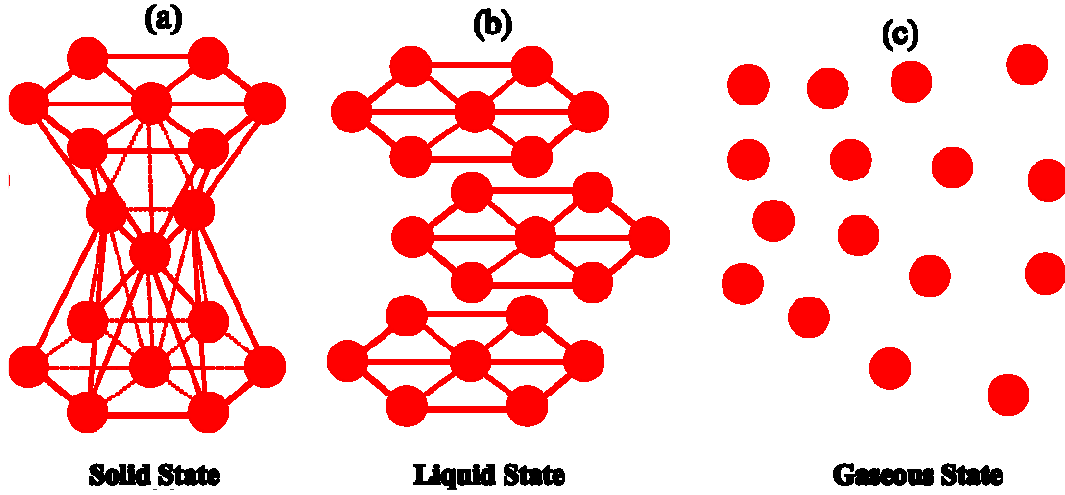


Figure 1.3: The above images correspond to an example of: a) a solid state where the dust particles are bound very strongly to each other for $\Gamma \gg 170$, b) a liquid-like state where the dust coupling is weak i.e., $1 < \Gamma < 170$, and c) the gaseous state where the dust particles do not interact with each other for $\Gamma \ll 170$.

It is defined as the ratio of potential energy of interaction between the dust particles, having charge ($Z_d e$) and separated from each other by a distance a to their kinetic energy. Thus, the expression for Coulomb coupling constant is given by

$$\Gamma = \frac{q_d^2}{4\pi\epsilon_0 a k_B T_d} \exp\left(-\frac{a}{\lambda_D}\right), \quad (1.15)$$

where $4\pi\epsilon_0 = 9 \times 10^9$ and T_d is the dust particle temperature in eV . From the above equation, it is clear that the coupling parameter reduces with an increase in the inter-particle separation and an increase in the plasma density. Depending upon the strength of the coupling constant, the complex (dusty) plasma can be categorized as:

- a) $\Gamma \gg 170$, the dust particles interact very strongly with each other and are said to be in the solid state, as shown in Figure 1.3 (a).
- b) $1 \ll \Gamma \ll 170$, the inter-dust interactions are weak and they are said to be in the liquid state, as shown in Figure 1.3 (b).
- c) $\Gamma \ll 1$, the dust particles are in the gaseous state with feeble interactions among each other, as shown in Figure 1.3 (c).

Let the inter-dust particle separation (a) be 1 mm and dust particles are at room temperature (i.e., $T_d = 0.03\text{ eV}$) and possess a charge of $Z_d = 5.18 \times 10^3$, then the value of the Coulomb coupling constant in such a case becomes $1200 > 170$. Thus, in the above case the dust particles will be strongly coupled to each other.

1.2.8 Forces on the dust particles

The main forces on dust particles in plasma, namely electric field force, ion drag force, thermophoretic force and neutral drag force are mostly irrelevant in the context of usual plasmas as these forces comes into picture only in the presence of dust particles. So it is important to discuss these forces as these may govern the entire dynamics of the dust particles in plasma. For the sake of simplicity, the forces acting on an isolated, spherical and dielectric dust particle in an unmagnetized cold plasma are discussed.

1.2.8.1 Electric field force

These micron-sized particles after getting charged experience repulsion due to the sheath electric field and get levitated. The force due to sheath electric field on the dust particles is given by

$$\vec{F}_E = Z_d \vec{E}. \quad (1.16)$$

Since $Z_d \propto r_d$, so F_E also depends linearly upon the dust size when $r_d \ll \lambda_D \cong \lambda_{Di}$.

1.2.8.2 Gravitation Force

The gravitational force is simply as

$$\vec{F}_g = m_d \vec{g} = \frac{4\pi}{3} r_d^3 \rho_d \vec{g}, \quad (1.17)$$

where g is the acceleration due to gravity and ρ_d is the mass density of the dust particles. The force obviously scales as the third power of radius of the dust particle sphere. Thus, it is the dominant force for particles whose radius lies in the micro-meter range whereas for nano-meter sized particles, gravitational force becomes negligible. For a dust particle size of $6.48 \mu m$ having density as $1.51 gcm^{-3}$, the dust mass becomes $2.15 \times 10^{-13} Kg$ and hence, the gravitational force on such a particles becomes $2.15 \times 10^{-12} N$. For levitating such a dust particle in the sheath electric field, one needs an electric field around $3.75 Vcm^{-1}$ for a dust charge of $3.5 \times 10^4 e^-$.

1.2.8.3 Ion Drag Force

Drag is a mechanical force. It is generated due to the interaction or contact of a solid body with a fluid (liquid or gas). It is not generated by a force field, like a gravitational field or an electromagnetic field, where one object can affect another object without being in physical contact with it. For a drag to be generated, the solid body must be in contact with the fluid. If there is no fluid, there is no drag. Drag is generated by the difference in velocity between the solid object and the fluid. Therefore, there must be motion between the object and the fluid. If there is no motion, no drag gets generated. It makes no difference whether the object moves through a static fluid or whether the fluid moves past a static solid object.

Ion drag force is an exceptionally important example of ion-dust interaction which arises due to the momentum transferred by the ions flowing past the dust particles [24].

It is responsible for a number of phenomena occurring in plasma like in the formation of voids – dust free regions in experiments under microgravity conditions, in the rotation of dust particle clusters in the presence of magnetic field etc. Ion drag force affects the properties of low-frequency waves, contributes to the inter-dust interactions and leads to the vertical alignment of dust particles in the presence of ion wake. Therefore, a good understanding of this force is necessary for studying the physics behind a wide variety of phenomena occurring in space plasmas and under laboratory conditions. For determining the ion drag force on the dust particles, generally two main theoretical approaches are used.

The traditional method to determine the ion drag force is based on the “binary collision formalism”. It is generally used in collisionless plasmas with the assumptions of an isotropic attractive Debye-Hückel (Yukawa) interaction potential between the ion and the dust particle and a shifted Maxwellian velocity distribution function for ions. It makes use of the standard theory of Coulomb scattering that is basically a linear approximation where it is assumed that the characteristic length of the ion-dust interaction is much shorter than the plasma screening length (i.e., the ion screening length) and most of the ions are scattered with small angle within the Debye sphere. This theory considerably underestimates the momentum transfer cross-section and resulting in underestimating the ion-drag force. The reason behind this is that the dust surface potential is of the order of the electron temperature and the ions are strongly coupled to the dust particles in a wide surrounding region, provided the electron-to-ion temperature ratio is large. This implies that the characteristic length of the ion-dust particle interaction can be comparable and even more than the plasma screening length. However, the Coulomb scattering theory neglects all collision events with impact parameter larger than the plasma screening length. There were attempts to improve the

situation by postulating the plasma screening length to be equal to the electron screening length [25] which in turn enhances the ion drag force to a great extent.

Khrapak proposed an extension of the Coulomb scattering theory to the regime of moderate ion-dust coupling [26]. The force depends upon the thermal scattering parameter $\beta_T = Q_d e / \lambda_D T_i$. For sub-thermal flows at moderate coupling strength $\beta_T \lesssim 5$, the expression for ion drag force is given by

$$F_i = \frac{1}{3\sqrt{2}\pi} \left(\frac{T_i}{e}\right)^2 \Lambda_{di} \beta_T^2 M_T, \quad (1.18)$$

where Λ_{di} is the dust-ion Coulomb coupling logarithm. In the linear regime $\beta_T \ll 1$, the logarithm reduces to $\Lambda_{di} \simeq 2 \ln \beta_T^{-1}$, which is identical to that obtained from the standard Coulomb scattering theory. In the opposite regime of strongly nonlinear scattering, $\beta_T \gg \beta_{cr} \simeq 13$, we obtain the following expression for ion drag force

$$F_i \cong \frac{2}{3} \sqrt{\frac{2}{\pi}} \left(\frac{T_i}{e}\right)^2 \ln^2 \beta_T M_T. \quad (1.19)$$

The above approach for calculating the ion drag force suffers some limitations too. Some of them are summarized here:

- In this approach, ion-neutral collisions are completely neglected. So this approach should not be used at pressures where the ion-neutral mean free path starts affecting the ion flux to the dust particle surface.
- The above approach presumes a certain potential distribution around the test charge, although the potential is a self-consistent function of the surrounding plasma parameters (e.g., ion collisionality, ion flow velocity, etc.).
- The approach presumes certain velocity distribution for the flow of ions.

Ivlev *et al.* [27] [28] proposed a kinetic model that accounts for the effects of ion-neutral collisions on the ion drag force experienced by a dust particle when kept in plasma. Following assumptions were taken into account:

- Electrons are assumed to be following Boltzmann distribution.
- Ions are described by the kinetic equations with the collisional integral in the Bhatnagar-Gross-Krook (BGK) form with constant ion-neutral collision frequency.

The ion and electron density perturbations are coupled to the Poisson equation. The polarization field induced by the dust particle at its origin can be obtained by linearizing this system of equations. The product of the polarization field with the dust particle charge yields the ion drag force experienced by a non-absorbing dust particle.

For sub-thermal ion velocities, ($v_i \ll v_{thi}$ or $M_T \ll 1$), in the bulk quasineutral, collisional plasma, the expression for the ion drag force acting on the dust particles with Maxwellian collisional ions is given by

$$F_i \cong \frac{1}{3} \sqrt{\frac{2}{\pi}} \left(\frac{T_i}{e} \right)^2 \left[\ln \beta_T^{-1} + \frac{1}{\sqrt{2\pi}} \mathcal{K} \left(\lambda_D / \ell_i \right) \right] \beta_T^2 M_T + O(M_T^3), \quad (1.20)$$

where $\mathcal{K}(x) = x \arctan x + \left(\sqrt{\frac{\pi}{2}} - 1 \right) \frac{x^2}{1+x^2} - \sqrt{\frac{\pi}{2}} \ln(1+x^2)$ is the “collisional function”. For $\ell_i \geq \lambda_D$, the function $\mathcal{K}(\lambda_D / \ell_i)$ is negligibly small compared to the Coulomb Logarithm and hence, can be neglected. If the collisions become “very frequent”, $\ell_i \leq \beta_T \lambda_D$, the kinetic effects completely disappear and the resulting ion drag force is given by

$$F_i \cong (1/6) \left(\frac{T_i}{e} \right)^2 \left(\lambda_{Di} / \ell_i \right) \beta_T^2 M_T, \quad (1.21)$$

where $M_T = v_i / v_{thi}$, is the ion thermal Mach number, $\beta_T = Z_d e^2 / \lambda_D T_i$, is the ion-dust interaction parameter and $\lambda_D \cong \lambda_{Di} = \left(\frac{T_i}{4\pi e^2 n_i} \right)^{1/2}$ is the effective plasma Debye length. After putting the value of β_T in the above equation, the expression for ion drag force takes the below mentioned form

$$F_i \cong \frac{1}{6} \left(\frac{Z_d e}{\lambda_D} \right)^2 \left(\frac{\lambda_{Di}}{\ell_i} \right) M_T \quad (1.22)$$

Z_d , n_i , T_i , v_i and v_{thi} are dust particle charge number, plasma (ion) density, ion temperature, ion drift velocity and ion thermal velocity, respectively.

Since the inequality $m_i / m_e \gg T_e / T_i$ is valid for any plasma, the electron drag can be neglected [29], because electron and ion flows on a dust particle are equal to each other and the momentum transfers are determined by the quantities $\sqrt{m_e T_e}$ and $\sqrt{m_i T_i}$.

1.2.8.4 Neutral Drag force

Neutral drag force is the measure of the rate of momentum exchange between dust particles and the surrounding gas neutrals during their collisions with each other. For the estimation of neutral drag force, the whole working regime is divided into two parts depending upon the value of the dust Knudsen number (K_n); which is defined as the ratio of the neutral mean free path to the dust particle radius. When $K_n \ll 1$, the working regime is called as the hydrodynamic (high-pressure) regime where the neutral drag force can be determined using Stokes' law. For $K_n \gg 1$, kinetic regime comes into

pictures. For most of the experiments involved in the complex (dusty) plasmas, $K_n > 1$ i.e., kinetic regime should be used. In such a case the neutral drag force can be determined by considering a Maxwellian distribution of surrounding neutrals. Generally, the relative velocity of dust particles (v_d) with respect to the neutrals (u_n) is found to be very small than the thermal velocity of the neutrals (v_{Thn}) i.e., $|v_d - u_n| \ll v_{Thn}$. Therefore, according to Epstein friction [30], the neutral drag force experienced by the dust particles, for a perfect diffuse reflection, is given by

$$F_{dn} = m_d \nu_{nd} (v_d - u_n), \quad (1.23)$$

where ν_{dn} is the dust-neutral collision frequency.

$$\nu_{dn} = -\frac{8}{3} \left(1 + \frac{\pi}{8}\right) \sqrt{2\pi} r_d^2 \frac{m_n}{m_d} n_n v_{Thn} \quad (1.24)$$

When the neutrals are in the diffused state, $u_n \approx 0$. In this case the expression for the neutral drag force becomes

$$F_{dn} = -m_d \nu_{nd} v_d \quad (1.25)$$

For a dust particle velocity of 4 cm s^{-1} and neutral gas density of $3 \times 10^{16} \text{ cm}^{-3}$ at a pressure of 134 Pa , the neutral friction will be $1.4 \times 10^{-12} \text{ N}$.

1.2.8.5 Thermophoretic force

Let us consider plasma with a finite temperature gradient in the neutral gas. Then the neutrals present in the high temperature region will exert more momentum on the dust particles than those present in the lower temperature region, resulting in a net momentum transferred to the dust particles. The rate of net momentum transferred to the dust particles by the neutral temperature gradient is called as the thermophoretic

force (F_{Th}). The magnitude of this force is directly proportional to the gas temperature gradient and is directed in the direction of the heat flux. At high neutral pressure, when the characteristic lengths of the dusty plasma is much larger than the neutral mean free path (few microns), the thermophoretic force can be assumed to be independent of the neutral pressure and mass of the neutral gas. The expression for thermophoretic force under such conditions can be written as below [30]:

$$F_{Th} = - \frac{5}{4\sqrt{2}} \left(\frac{r_d}{\sigma_{LJ}} \right)^2 k_B \nabla T_n, \quad (1.26)$$

where k_B is the Boltzmann's constant and σ_{LJ} is the Lennard-Jones collision diameter of the gas. For Argon gas, it is equal to 3.4 Å.

The thermophoretic force experienced by the dust particles for a temperature gradient of $\nabla T_n \approx 1 \text{ K cm}^{-1}$ is $1.0 \times 10^{-13} \text{ N}$, which is one order less compared to the gravitation force (and other forces as mentioned above).

After discussing the different forces experienced by the dust particles present in plasma, the order of magnitude of these forces is estimated for typical conditions of a dc glow discharge at high pressure. The results are given below in a tabular form:

Force	Formula	Magnitude (in N)
Gravitational force, F_g	$\frac{4\pi}{3} r_d^3 \rho_d \vec{g}$	$\sim 10^{-12}$
Electrostatic force, F_E	$4\pi\epsilon_0 r_d \alpha \left(1 + \frac{r_d}{\lambda_D} \right) \frac{T_e}{e} \varphi_d \cong F_g$	$\sim 10^{-12}$
Ion drag force, F_{id}	$\frac{1}{6} \left(\frac{Z_d e}{\lambda_D} \right)^2 \left(\frac{\lambda_{Di}}{\ell_i} \right) \frac{v_i}{v_{Thi}}$	$\sim 10^{-12}$

Neutral drag force, F_{dn}	$\frac{8}{3} \left(1 + \frac{\pi}{8}\right) \sqrt{2\pi} r_d^2 \frac{m_n}{m_d} n_n v_{Thn} v_d$	$\sim 10^{-12}$
Thermophoretic force, F_{Th}	$\frac{5}{4\sqrt{2}} \left(\frac{r_d}{\sigma_{LJ}}\right)^2 k_B \nabla T_n$	$\sim 10^{-13}$

Table 1.1: Order of magnitudes of different forces experienced by a levitated dust particle in plasma.

For the calculations given in the above Table 1.1, Argon gas plasma at a pressure of 133 Pa with ion temperature as equal to room temperature is considered. Mono-dispersed dust particles of diameter $6.48 \mu m$ and mass density as $1.51 gm cm^{-3}$ are assumed to be moving with a velocity of $4 cms^{-1}$. The electron temperature is considered as 2.15 eV and plasma density as $3 \times 10^9 cm^{-3}$ with a neutral gas temperature gradient as $\sim 1 K cm^{-1}$.

1.3 Overview of Earlier Works

Dusty plasmas are low temperature plasmas which, in addition to electrons, ions and neutrals, contain micron sized dielectric particles. When immersed in plasma, these particles acquire large charges depending upon their size and background plasma parameters. Because of the ability of the dust particles to acquire large charges, their presence in plasma increases the complexity of the whole system. The presence of charged dust grains not only modifies the existing low-frequency waves [31,32], but also supports the formation of crystalline structures [11,10], voids and self-organized structures [15,33], waves [34,35,36] and rotation of dust particles [15,37]etc.

Dust rotation is an interesting fundamental issue which has been addressed in many laboratory experiments. In some of these experiments, magnetic field was applied [38,39,40,41,42,43,44] where the common feature was the magnetic field perpendicular to the existing electric fields inside the plasma induces an azimuthal ($E \times B$) rotation of

ions which further causes the levitated dust particles to rotate in azimuthal direction. The rotating ions, in addition to interacting with the dust particles directly, may also interact with them via neutrals. In this case, part of the momentum transferred to the neutrals by the ions may be imparted by the neutrals to the dust particles causing them to rotate [43] in the direction of the ions.

Rotation of dust particles and convective vortex motion in the absence of magnetic field in laboratory plasmas as well as under microgravity conditions has also been reported in many experiments. Under microgravity conditions, a dust-free region called – void is observed in the central region of the discharge [15], around which dust vortices get formed. Later, it is shown in a simulation work [18] that the dust vortices around the void [15] get generated due to the non-conservative nature of the forces, such as ion drag force, electric force, and screened Coulomb force, acting on the dust particles. In ground-based experiments, the dust rotation in crystalline structures was observed to be induced by a biased probe immersed in plasma [45] where it was suggested that ion wake fields generated due to the biased probe give rise to a local space charge accumulation; the variation in the space charge leading to the formation of a non-uniform electric field is proposed to be the origin of dust circulation. In an inhomogeneous plasma, the dust charge gradient [46,33,47,48,49] in the presence of a non-electrostatic force orthogonal to it may cause an instability which further leads to the formation of the dust vortices. In a dc plasma, a two-dimensional dust vortex flow near the edge of a metal plate can be generated due to an asymmetry of ion drag force near the metal plate [50]. Also, the presence of temperature gradient in the background gas, can give rise to two types of gas convection; (a) free (Rayleigh-Benard) convection at high (almost atmospheric) gas pressures and (b) convection induced by thermal creep at low pressures [51]. At low pressures, the dust vortices are observed to form in a low

frequency discharge produced in an inhomogeneously heated vertical glass tube due to the presence of a thermal creep flow (TCF) [52]. Later on, a special experiment was designed to isolate the thermal creep flow (TCF) from other temperature gradient effects and the role of TCF on vorticity formation was verified at low pressure [53]. The role of ion drag force in the formation of dust vortices as well as its importance has been further stressed in two recent publications. In one publication [37], it is shown that the dust vortices, under microgravity conditions, may arise as a result of the balance between the driving torques due to ion drag force and dust charge and the loss of torque by friction on the neutral gas. In another publication [54], it is shown through an analytical formulation that a shear in the ion flow leads to vortex generation in a bounded setup.

In a nutshell, one can notice that there are different mechanisms that can cause dust rotation. In this thesis, the observation of poloidal rotation of dust particles in toroidal structures formed in parallel plate dc glow discharge plasma is presented. The subtlety in our experiments is that the dust particles are kept on the lower electrode (not sprinkled from top) with a concentric metallic ring surrounding them. The metallic ring induces non-homogeneity in the plasma whereas the presence of dielectric dust particles enhances this inhomogeneity. We suggest that the dust rotation may arise due to a gradient in the ion drag force, caused by a gradient in the plasma density (which is evident from Langmuir probe measurements) in the presence of an electric field force. This was arrived at by carefully eliminating other probable causes in our experiments. The cause of rotation is then confirmed by conducting another set of experiments where the introduction of an additional density gradient leads to the formation of an additional dust vortex. The direction of rotation of dust particles in vortices is also observed to follow the direction of the density gradient. Additionally, the dust particle velocity is found to be very high ($\sim 4 - 5 \text{ cm s}^{-1}$) with a radial gradient in it. The observed

rotation/vortices in this kind of structures may have interesting relation to various processes involving rotational flow of matter, ranging from those at the astronomical scales, like galactic star formation [55], to those at the micro- or nano-scales, like mixing of heterogeneous fluids [56]. Vortex flow is fundamental to fluid dynamics as the vortices are analytic building blocks in a scale-free dynamical formulation of the fluid turbulence [57]. The vortices forming in laboratory dusty plasmas provide the opportunity to study these dynamic building blocks at the microscopic level of the medium which is impossible in any other conventional fluid medium [58,59].

1.4 Scope and Outline of the Thesis

Dust vortices/rotation has been reported in numerous experiments due to the dust charge gradient or thermal effects (such as thermal creep flow, free convection) in the absence of any external magnetic field. The cause of rotation (in the absence of thermal effects) in most of these experiments is supported either by qualitative explanations or by producing simulation studies. The effect of the different discharge parameters on the dust vortices has also not been studied in details. As mentioned earlier, this thesis deals with the study of dust vortices, with and without void at the centre, discovered in experiments performed using micron-sized mono-dispersed dust particles immersed in dc glow discharge plasma at high gas pressure. The investigation of the phenomena aims at the better understanding of the principle driving mechanisms behind the dust rotation.

This thesis consists of seven chapters and is organized as follows:

The main features of experimental set-up, in which the experiments are performed, have been described in Chapter 2. This chapter also gives an overview of the working of the

sCMOS camera and the PIV analysis that has been used for determining the different parameters associated with the rotating dust structures.

Chapter 3 gives a short review of the different existing theories that can be used for extracting out the useful data from the I–V characteristics of a Langmuir probe at different pressures and densities. This chapter also explains the instrumentation involved for preventing the dust contamination and for removing the capacitive current.

The experimental observations of the rotation of mono-dispersed dust particles and the probable cause are conjectured in Chapter 4. This chapter also discussed the various properties of the rotating dust structures.

Chapter 5 provides the experimental evidence supporting the model based on the ion drag gradient, arising due to density gradient, as the principal cause of dust rotation (as conjectured and elucidated in chapter 4). The dust dynamics is described using hydrodynamic formulations. It is observed that the vorticity of the dust fluid is in good agreement with that provided by the ion drag.

Chapter 6 discusses the experiments performed related to the evolution of the toroidal dust structures with the background neutral pressure and discharge current. The effect of discharge current and pressure on the dust vortices have been investigated as well as some behavioural changes such as transition of filled to hollow and then again to filled vortices are presented. The increase in the dust velocity with an increase in the pressure is observed, contrary to an increase in the neutral friction. An analysis in order to understand the mechanism responsible for this behaviour of dust particle velocity is attempted.

Chapter 7 summarizes the major findings of this research, and concludes with an outlook for future studies.

2 CHAPTER: EXPERIMENTAL SET-UP

In this chapter, section 2.1 introduces the basic experimental set-up, along with the various sub-systems, employed to perform experiments using mono-dispersed dust particles. Thereafter, section 2.2 gives a brief overview of the working of the sCMOS camera. The PIV technique used for determining the different parameters associated with the rotating dust structures is described in section 2.3, followed by a summary in section 2.4.

2.1 Experimental Set-up

2.1.1 Vacuum Vessel and Electrode Arrangement

The experimental set-up consists of a cylindrical vessel of diameter 31 cm and length as 50 cm. It has two axial and four radial ports, as shown in Figure 2.1. The bottom radial port is being used for evacuating the system as well as for inserting the bottom electrode. The bottom radial port has two perpendicular KF 25 ports attached to it. One of these KF 25 ports is being used for introducing the working gas inside the system through a needle valve. A convectron gauge is used at the same port to measure the gas pressure. Another KF 25 port is being used for taking out connections of the thermocouple attached to the bottom electrode. To evacuate the vacuum vessel, a rotary pump with pumping speed of 600 *litres/min* is used. The ultimate vacuum, which is achieved with this rotary pump, is 5×10^{-3} *mbar*. The top radial port is used for inserting the upper electrode and its electrical connections inside the system. For inserting the laser sheet to illuminate the dust particles, one of the side radial ports is used and another side radial port is used for inserting the probe diagnostics to determine the plasma properties, as shown in Figure 2.2.

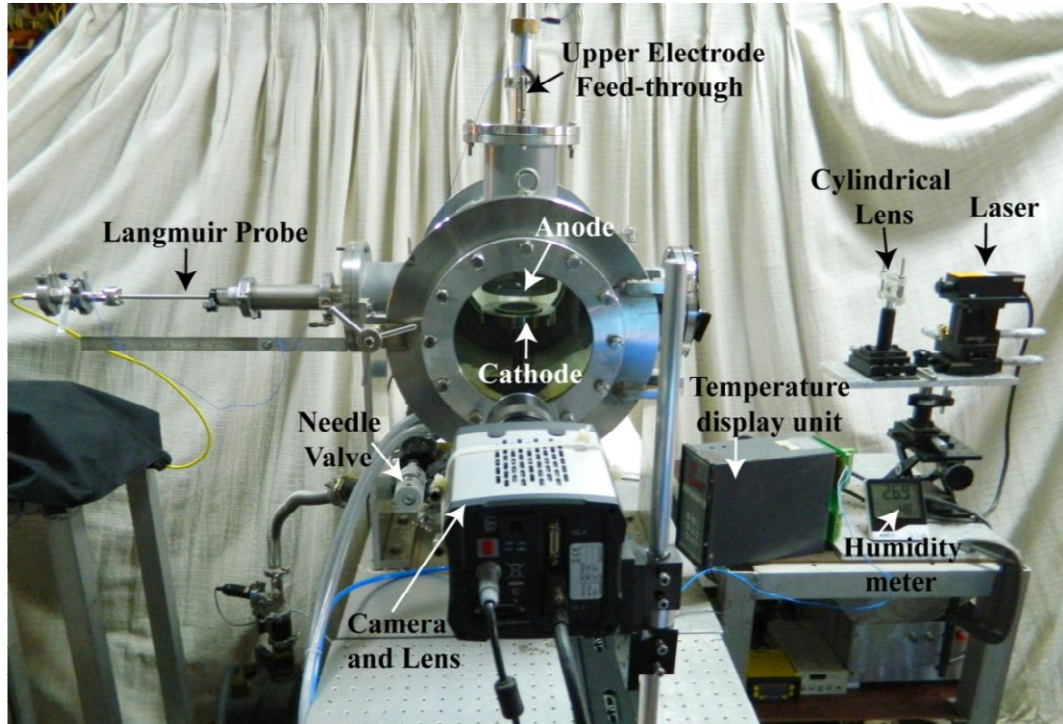


Figure 2.1: Front view of the experimental system with various sub-parts attached to it.

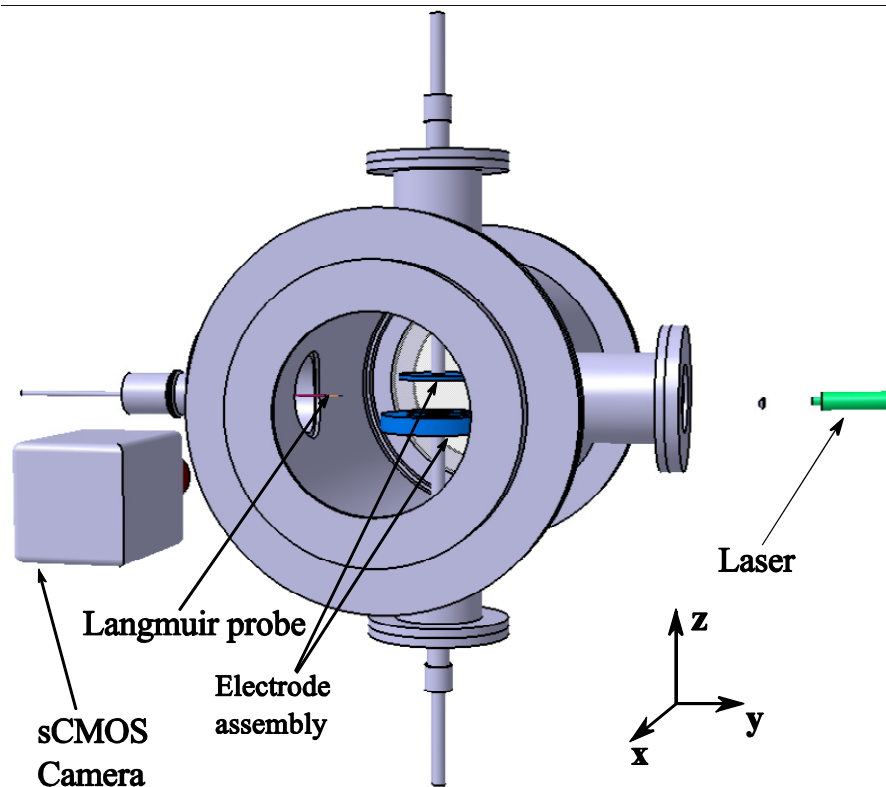


Figure 2.2: Three-dimensional view of the experimental system. The camera is directed in the x-direction, vertical Laser sheet enters the experimental region of interest in the y-direction and z represents the (vertical) direction of electrode axis.

There are two axial ports on the cylindrical vessel with glass flanges of outer diameter 20 cm attached to them. On one of the axial ports, a sCMOS camera is permanently installed for capturing/imaging the dynamics of the dust particles illuminated by a laser sheet. The other axial port is being used for capturing the colored images of the plasma conditions using a DSLR camera. It can also be used either for inserting other electrical diagnostics or beam probes, etc.

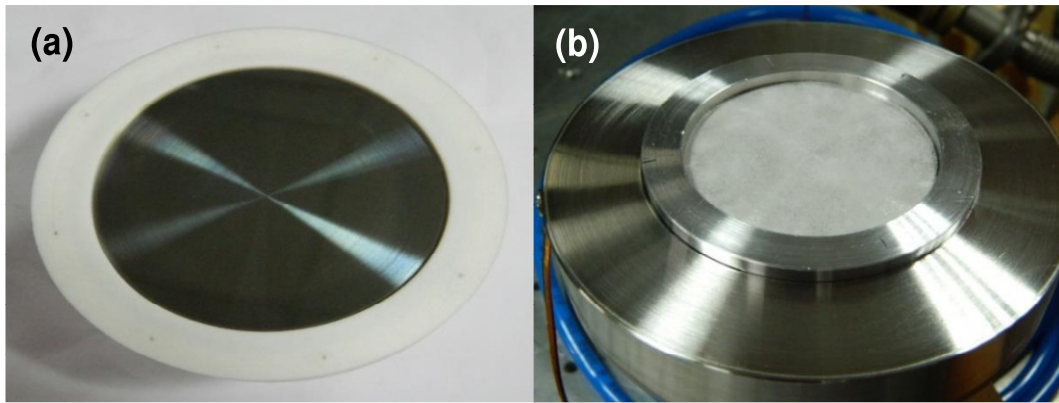


Figure 2.3: (a) shows the photographs of the anode covered using BN cup and (b) represents the specially designed water cooled cathode

The discharge is being produced between two parallel plate SS304 electrodes. The upper electrode is a disk of outer diameter as 10 cm and act as anode, as shown in Figure 2.3 (a). Its edges have been covered by an insulator which allows only the front part of anode to take part in the plasma production and the exposed diameter to the anode is 90 mm. The lower electrode, which is a grounded cathode, is a disk of diameter 13 cm, as shown in Figure 2.3 (b). The lower electrode has a provision of water cooling. A thermocouple has been installed on it. For the better confinement of the dust particles, an Al ring with inner diameter as 63 mm, outer diameter as 82 mm and height 3.5 mm has been kept on the lower electrode in a groove on it which makes the height of the metallic ring above cathode as 3 mm and is in electrical contact with

the lower electrode. The whole body of the cylindrical system along with the lower electrode is acting as a grounded cathode. The inter-electrode separation can be varied from 1 – 10 cm but for the present experiments it has been fixed as 4 cm. The discharge voltage is varied between 270 V to 470 V with discharge current ranging from 1 mA to 50 mA. No magnetic field has been used in these experiments. Mono-dispersed Melamine Formaldehyde particles of diameter 6.48 μm has been used and kept on the lower electrode inside the confinement ring. The dust particles are being illuminated by using a vertical laser sheet of thickness around 2 mm. A green laser of wavelength 532 nm and power as 100 mW is used for illuminating the dust particles. For converting the laser beam into a sheet, it is followed by a cylindrical lens. The laser sheet is being introduced in the system from one of the side radial port. The light scattered from the dust vortices is being captured by a sCMOS Neo camera which has been installed on one of the axial ports.

2.1.2 Laser Sheet Formation Optics

A circular laser beam can be converted into a thin sheet by means of a cylindrical lens to illuminate the micron or submicron sized dust grains present in the plasma forming different structures. A lens is generally characterised by its three basic parameters:

1. Focal length of a lens
2. Aperture number
3. Image magnification

The aperture of a lens is a hole or opening through which the light travels. The aperture is the ratio of its focal length to diameter of the opening, whereas image magnification of given by the ratio of image distance to the object distance. A cylindrical lens is a lens which focuses the light passing through it on to a line unlike the spherical lenses which

focus on to a point. The curved face or faces of a cylindrical lens are sections of a cylinder and focus the image passing through it onto a line parallel to the intersection of the surface of the lens and a plane tangent to it. The lens compress the image in the direction perpendicular to this line, and leaves it unaltered in the direction parallel to it (in the tangent plane). When a cylindrical lens acts as a magnifier, it magnifies only in one direction. The plano-concave cylindrical lens expands the laser beam in the vertical direction leaving the horizontal direction constant followed by a spherical lens. The resulting system acts as a beam expander in the vertical direction. This arrangement is generally used where uniform illumination along the propagation direction is required. However, this arrangement cannot be used where long regions for illumination are needed because for that one needs large aperture spherical lenses.

A laser provides a light beam of very small diameter. To convert this beam in the shape of a sheet (for illuminating a large dust particle cloud), various types of cylindrical lenses are used. In our experiments, we have made use of a Vertical Cylindrical Lens which converts the laser beam into a vertical sheet of light.

The cylindrical lens used for the present experiment has the following specifications:

Lens Type	PCX cylinder
Glass Type	BK7
Size (Height \times Length)	$\sim 25 \text{ mm} \times 25 \text{ mm}$
Effective Focal Length	25 mm
Back Focal Length	$\sim 18 \text{ mm}$

Radius	~ 13 mm
Centre Thickness	~ 11 mm
Edge Thickness	~ 1.5 mm

Table 2.1: The details of the cylindrical lens used for converting the laser beam into a vertical plane.

2.1.3 Selection of Dust Particles

In dusty plasma, the gravitational pull is balanced by the repulsion because of sheath electric field. So, it is always tempting to choose smaller dust particles. The advantage with small particles is that the weight of these particles is small. They require less sheath electric field for levitation. However, it is very difficult to illuminate using visible light sources as well as image the dust particles having small sizes generally below 1 micron. So from the point of view of cameras, one may choose to work with bigger particles. The advantage of using bigger particles is that they are easy to record using a camera, but they pose a problem when we go to work with particle sizes above 10 micron as to levitate these particles, stronger sheath electric fields are required. From the above discussion one can conclude that it is always better to work with the dust particles sizes lie in the range 3 – 9 micron.

In experiments, mostly, dielectric particles are used than metallic particles as it is much easy to work with them. Dielectric particles can be kept on one of the electrodes while in case of metallic particles, one has to sprinkle these particles from the top so that they can get suspended in plasma. In general the metallic particles are heavier than the dielectric particles of the same size because of their higher mass densities, thus require higher electric fields for levitation. Metallic particles have one very important

advantage too. Because of the conduction, whatever charge they acquire, it gets distributed on the whole body of the dust particle which does not happen in case of dielectric particles. In case of dielectric particles, in addition to the particle size it is always advisable to use the dust particles with good chemical and physical properties.



Figure 2.4: The image of a sample of melamine formaldehyde (MF) condensation resin particles being used in experiments having average diameter as $6.48\ \mu\text{m}$, obtained using a microscopic shows that the dust particle are spherical in nature (to a very good approximation). The size distribution is extremely narrow (standard deviation is **$0.1\ \mu\text{m}$**).

Based on the considerations discussed above and depending upon the availability of standard sizes of mono dispersive melamine formaldehyde (MF) particles of diameter $6.48\ \mu\text{m}$ are used in the present experiments due to their excellent mono-dispersivity ($CV < 3\%$) and highly uniform spherical shapes. An image of the mono-dispersed particles taken with the help of a microscope is shown in Figure 2.4. Approximately ~ 1 gm of mono-dispersed MF dust particles are spread on the cathode surface inside the metallic ring uniformly using a mesh as the levitation of dust particles is found to be sensitive to the distribution of dust particles on the cathode. These particles have a low

mass density ($\sim 1.51 \text{ gcm}^{-3}$) and are resistant up to high temperatures ($\sim 300^\circ \text{C}$) and they do not agglomerate easily. Apart from MF particles, Silica particles of approximately same size as that of the MF particles are also used in some of the experiments. Silica particles also have a low mass density ($\sim 1.8 - 2 \text{ gcm}^{-3}$) and resistant to high temperatures ($\sim 1000^\circ \text{C}$).

2.2 Camera

2.2.1 Principle of Operation

A Charge Coupled Device (CCD) camera does four basic tasks for generating an image.

These tasks are

- Charge generation
- Charge collection
- Charge transfer
- Charge measurement

The first operation relies on a process named as photoelectric effect when light quantas with some energy strike certain surfaces, give rise to the generation of electrons known as photoelectrons. In the second step these photoelectrons are collected in the nearest discrete collecting sites. The collecting sites are defined by an array of electrodes formed on the CCD chip and are called as gates. This step depends upon three different parameters: 1) the area and number of pixels present on the CCD chip, 2) the total number of photo generated electrons that a pixel can hold and 3) the ability of the “target pixel” to efficiently collect the photo-generated electrons.

The third operation which is charge transfer is executed by manipulating the voltage on the gates in a systematic way so that the electrons move down the vertical registers

from one pixel to next in a conveyor-belt like fashion. At the end of each column there is a horizontal register of pixels, which collects one line at a time and transports each packet to an on chip amplifier in a serial manner. The last step is executed when an individual charge packet is converted into an output voltage. This voltage of each pixel can be amplified off-chip and digitally encoded and stored in a computer. Camera is one of the major diagnostic tools for dusty plasma experiments. Thus, it is very important that one determines the required camera very carefully. The probable procedure that can be followed, while choosing the right camera for imaging the micron sized dust particles in complex (dusty) plasma, is as follows.

2.2.2 Selection of Camera and Accessories

In order to study the physics underlying the formation of dust vortices, three-dimensional structures, waves and oscillations, it is not sufficient just to produce them, but sophisticated diagnostics and analysis tools are also required to extract the accurate information from the experimental data. Depending upon the physics problem to be studied, the choice of camera depends on three very important parameters (other than the full well capacity, dynamic range, etc.). These three basic parameters are: (1) Number of pixels on the camera chip, (2) Size of each pixel and (3) Frame rate of the camera. The field of view is decided by the number of pixels, pixel size and the camera lens used.

The main physics issue for which this camera would be used is the dust rotation where locating each and every particle for PIV analysis is of prime importance. In this experiment, the dust particles are expected to rotate in the circular orbits at very high speeds $\sim 2-10 \text{ cm s}^{-1}$. To resolve the particles moving with such high speeds, the exposure time of the camera should be sufficiently small otherwise the particles can travel over a number of pixels in a single exposure time and will appear as lines. At the

same time, in order to capture the complete dust structures large field of view is necessary. In the CPED system, depending on the cathode and ring dimensions, field of view of $\sim 85 \times 40 \text{ mm}^2$ is required. Apart from the rotation studies, locating the dust particles precisely and accurately to determine the inter-particle separation between them is also important in studies related to various types of crystalline structures. The pair correlation function that tells about the various states of the dust structures (like fcc, hcp etc) critically depends on the inter particle distances that needs to be measured very accurately. Therefore, to capture the rotating structures of dust particles, a fast camera with a high frame grabbing rate (inverse of exposure time) and high resolution with pixel size comparable to the size of the particles and large number of pixels, is required.

The second physics problem, which is widely studied in complex plasmas, is the wave study. In this case, a camera with high frame rate, not high resolution, is used. Typically, the dust plasma frequency lie in the range 1 - 50 Hz for particle sizes of the order of few microns. In case of wave study in complex plasmas, the region of interest will be of the order of around $50 \text{ mm} \times 50 \text{ mm}$. Considering all the above prerequisites, a black & white sCMOS Neo[®] camera containing $2560 \times 2160 \text{ pixels}$ with each pixel of size $6.5 \text{ }\mu\text{m}$ has been chosen for the experiments in CPED.

In addition to these requirements, the dynamic range, full well capacity and dark noise should be taken into account very carefully. Depending upon the requirements of our experiments, some primary experiments are performed to check whether the full well capacity, dynamic range, signal to noise ratio etc. of the camera are in accordance with the experimental requirements or not. For doing so, an optical beam probe is used to collect the light coming from the plasma and the illuminated dust particles. The number of photons are determined from the data obtained using the beam probe.

$$\text{The number of photons} = 2.09 \times 10^{14} \frac{\text{photons}}{\text{cm}^2 \cdot \text{sr} \cdot \text{nm} \cdot \text{sec}}.$$

$$\text{Let the area of one pixel} = 6.5 \mu\text{m} \times 6.5 \mu\text{m}$$

$$= 42.25 \mu\text{m}^2$$

$$= 0.4225 \times 10^{-6} \text{ cm}^2$$

$$\text{Let the frame rate of the camera} = 100 \text{ fps}$$

$$\text{Let focal length } (f) \text{ of the lens} = 16 \text{ mm}$$

$$\text{Let the F- number of the lens be } (N) = 4$$

$$\text{then the solid angle of the lens} = \pi \left(\frac{1}{2N} \right)^2$$

$$\text{Thus, the solid angle} = \pi \left(\frac{1}{8} \right)^2 = \frac{\pi}{64} \text{ sr} = 0.049 \text{ sr}$$

Since we intend to calculate the number of photons striking each pixel for each frame,

$$\begin{aligned} \text{The number of photons} &= 2.09 \times 10^{14} \frac{\text{photons}}{\text{cm}^2 \cdot \text{sr} \cdot \text{nm} \cdot \text{sec}} \\ &\times \frac{0.4225 \times 10^{-6} \text{ cm}^2 \times 0.049 \text{ sr}}{100 \text{ fps}} \end{aligned}$$

$$= 4.326 \times 10^4 \frac{\text{photons}}{\text{frame} \cdot \text{pixel}}.$$

(Omitting nm)

$$\text{The quantum efficiency of the camera} = 50\%$$

$$\text{Thus, the number of photoelectrons} = 4.326 \times 10^4 \frac{\text{photons}}{\text{frame.pixel}} \times \frac{50}{100}$$

$$= 2.163 \times 10^4 \frac{\text{photons}}{\text{frame.pixel}}$$

This camera gives $0.48 e^-$ per count.

So, the number of photo-electrons,

$$n = 2.163 \times 10^4 \frac{\text{photons}}{\text{frame.pixel}} \times 0.48 e^- \text{ per count}$$

$$= 10382.4 \frac{\text{photoelectrons}}{\text{frame.pixel}}$$

Thus, enough electrons are available as compared to the full well capacity of the camera photo-site.

$$\text{The full well capacity of the camera} = 30,000 e^-$$

$$\text{The read out noise} = 10 e^-$$

$$\text{Then the signal to noise ratio becomes} = \frac{30,000}{10} = 3,000$$

$$\text{The dynamic range} = 75 \text{ dB}$$

We know that

$$\text{Dynamic range} = 20 \log_{10} (\text{signal to noise ratio}) \text{ decibel}$$

$$\text{Levels} = 70 \text{ dB} = (20 \log_{10} G) \text{ dB}$$

$$\text{Signal to noise ratio (SNR)} = 10^{70/20} = 3162.2778$$

If a 14 – bit A/D converter is used then there will be $2^{12} = 4096$ levels.

So the minimum requirements for our camera are full well capacity 30,000 e^- , dynamic range 70 dB and 12 – bit A/D converter which are being fully satisfied by the camera that has been chosen for doing experiments.

2.2.3 Interfacing media

The camera being used possesses a maximum resolution of 2560×2160 pixels at a frame rate of $100s^{-1}$. The size of each pixel is approximately equal to $6.5 \mu m$. So, the rate at which the camera can produce images is given by

$$\text{Image production rate} = 2560 \times 2160 \text{ byte} \times 100 s^{-1} = 552.96 \text{ MB/s.}$$

The transfer rate of the interfacing media should be more than the production rate of the camera. According to Nyquist Criteria, the highest camera frame transfer rate should be at least four times the production rate. If the camera does not has an on-head memory for momentary saving the data, then the data has be to transferred to the computer. The data transfer can be done using three modes: GigE Vision, CameraLink base and CameraLink Full. GigE Vision can transfer at a rate of around 120 MB/s, CameraLink Base around 200 MB/s while CameraLink Full can transfer at a rate more than 370 MB/s. Thus Camera Link full is the better option for a camera with no on-head memory. However, if the camera has an on-head memory then the connector with less transfer speed can be used. In the present case, the camera being used in our experiments has an on-head memory capacity of 4 GB.

The computer should also be capable to store/write the data at the same rate at which it is reading it. PCI cards have a transfer speed of 130 MB/s. So they cannot be used.

Whereas, PCI express cards that transfer the data, faster than PCI cards, are selected for transferring the data from camera to the computer. The suitable card in this case is PCIe $\times 4$ card which has a speed of $1GB/s$.

The camera can deliver sustained $30\ fps$ or up to $100\ fps$ in burst mode at full resolution. The camera is equipped with 4 GB of on-head memory buffer. The on-head memory buffer can store 400 to 500 frames corresponding to 4 to 5 seconds of videos having maximum frame grab rate capacity at full resolution of the camera. For studying faster dust dynamics, the frame rate can be further increased by reducing the camera resolution (i.e., the effective number of pixels), for example frame grabbing rate of $\sim 405\ fps$ can be achieved for the present camera at a resolution of $512 \times 512\ pixels$. For a fixed region of interest, higher kinetic series lengths are possible by lowering frame grabbing rates. But if both, the frame grabbing rate and kinetic series length, are required to be increased (like for determining the dust temperature), then the data must be spooled continuously to either the computer hard drive or computer RAM with greater than 4 GB capacity.

The data from the camera is transferred to the computer hard-drive from the on-head buffer through a CameraLink cable of required transfer speed. The speed of data transfer is limited by the writing speed of computer hard-drive. To increase the writing speed, the unused RAM of the computer is converted into a virtual hard drive with much faster (~ 50 times faster than the physical hard-drive) writing speeds using a special software RAMDisk. Later, the data is transferred to the conventional hard-drive.

To obtain the required field of view (i.e., $\sim 85 \times 40\ mm^2$), the camera is being used with a Carl Zeiss made macro-lens of focal length of $100\ mm$. To increase the signal-to-noise ratio, a band pass laser-line filter has been used in-between the camera and the

macro-lens, which attenuates the background plasma light and allows the laser light scattered from the dust particles to pass through it.

2.3 Data Analysis Using PIV Technique

Particle Image Velocimetry (PIV) technique is a cross-correlation technique for determining the displacement of particles between pair of images. An image is decomposed into “interrogation cells” that are square of size $n \times n$ pixels, where n typically varies between 8 and 128. Within each cell, a finite number of particles are present. A two-dimensional Fourier transform is performed on a cell in Image 1 and Image 2. Then, the cross-correlation is constructed for the corresponding cells on two images. The peak of the cross-correlation represents the most probable displacement of the group of particles in the cell. It should be noted that the cross-correlation calculation can result in multiple peaks. The “quality” of the PIV analysis is measured as the ratio of the heights of the first and second cross-correlation peaks. For fluid systems, a ratio of 1.5 or greater is typically considered a good measurement. In practice, these studies have used ratios of 4 or greater for analysis of dusty plasmas.

There are additional refinements that can be used to improve the quality of the results generated in the PIV analysis. The first technique involves the overlapping evaluation regions. In the present work, 50% overlap is used. This is more than double the number of independent vectors that are computed and more accurately maps the velocity field. It is noted that a 50% overlap is the maximum overlap that can be used and still obtain independent PIV vectors. The second technique is multi-pass correlation. In this process, the correlation analysis is repeated m times. In the first pass, a displacement map is generated. In the next pass, when the correlation analysis is repeated, the sub-region extracted from the second image used in the correlation analysis is offset in the

direction of displacements that were computed in the first correlation analysis. This process is then repeated until m iterations. For each iteration, the displacement field that was generated in the previous correlation analysis is used to generate the image shift for the sub region in the second image. Finally, it is important to remember that PIV is not a particle measurement technique. Each vector constructed using PIV represents the motion of a group of particles within the interrogation cell. The cells are fixed in space and the particles flow in and out of the cells

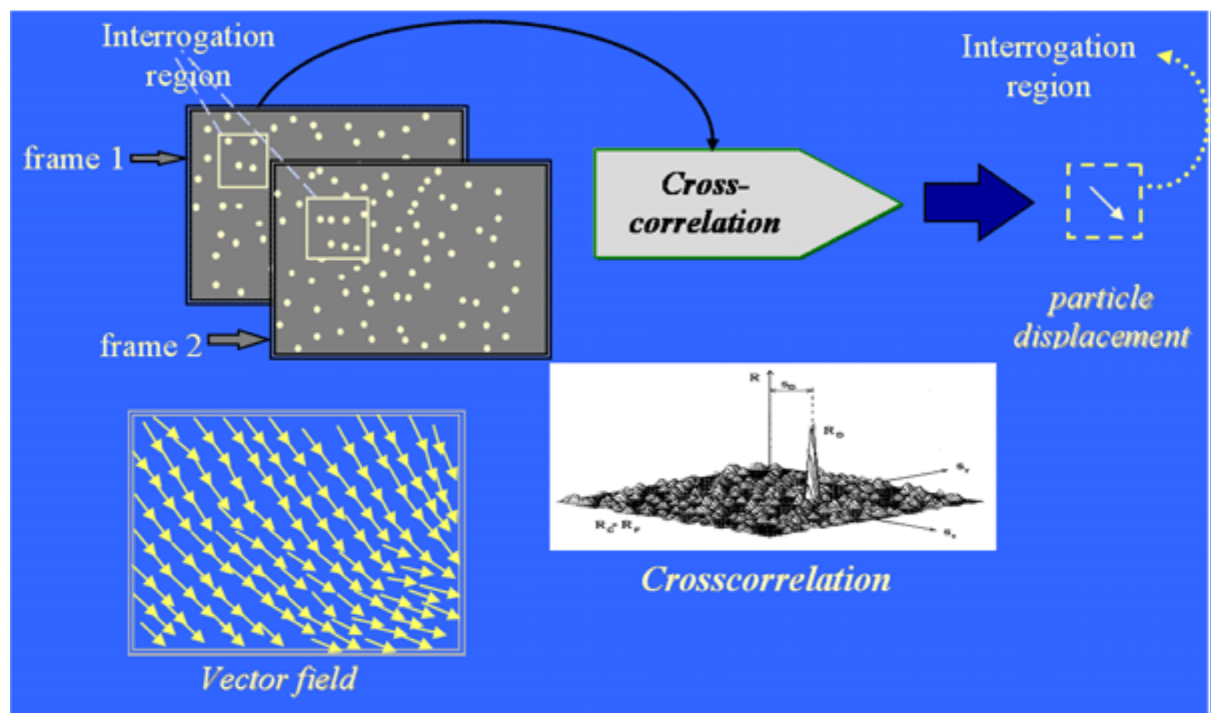


Figure 2.5: Typical arrangement showing the different steps of PIV techniques.

2.4 Summary

In this chapter, the main features of the experimental set-up developed for the study of dust vortices is described. An overview of the working of the sCMOS camera and the determination of its different parameters through calculations is provided. The PIV technique, that has been used for determining the different parameters associated with the rotating dust structures, has also been described.

3 CHAPTER: LANGMUIR PROBE FOR MEASUREMENTS IN DUSTY PLASMA AT HIGH PRESSURE

Langmuir probe is routinely used for the local measurements of plasma parameters. However, its use at high pressures in a dusty plasma environment is very complicated. This chapter is divided into eight sections. In section 3.1, we briefly describe the issues pertaining to the use of the Langmuir probes at high pressures and in a complex (dusty) plasma environment followed by a brief description of the basic Langmuir probe I-V characteristics and the different terms used to describe it in section 3.2. Section 3.3 describes the theories that may be used to interpret the probe characteristics keeping in mind the requirements of dusty plasma experiment. In section 3.4 we have discussed the probe design and its construction. The prevention of probe contamination and Langmuir probe instrumentation are discussed in section 3.5. Processing of the Langmuir probe data is discussed in section 0. In section 3.7, a double Langmuir probe used for the determination of electron temperature is described followed by discussion and summary in section 3.8.

3.1 Issues Pertaining the Use of Single Langmuir Probe

Langmuir probes are one of most widely used plasma diagnostics used for measuring plasma parameters. A Langmuir probe, in its simplest form, consists of a single electrode which is inserted into the plasma and biased at various potentials with respect to a reference electrode. The current collected by the probe is measured as a function of the probe bias and is called as its I-V characteristics. This I-V characteristics of the Langmuir probe is analysed to determine the various plasma parameters such as floating

potential, plasma potential, electron temperature, plasma density, electron energy distribution of the plasma, etc. Unfortunately, the theory underlying the probe response used for interpreting the I-V characteristics is not always straight forward but rather complicated. Probes are basically boundaries to the plasmas, and near the boundaries, the equations that govern the plasma behaviour get altered. This complicates the analytical treatment. Quasi-neutrality does not hold near the boundaries; a thin layer exists where electron- and ion- number densities differ significantly, which is often called the Debye sheath. The sheath region can sustain large electric fields which affect the motion of electrons and ions approaching towards the probe, hence the current collection. Occurrence of electron-neutral and ion-neutral collisions in the sheath region at high operating pressures makes the prediction of electron and ion trajectories even more difficult. The ratio of parameters like probe radius to Debye length, mean free path to probe radius determines the regime of operation of Langmuir probe. While designing a probe, one has to carefully choose the probe dimensions such that a well-defined theory exists for predicting the current collection by an attractive probe correctly in the regime of operation.

Probe operations in dusty plasma require special consideration, such that the disturbance caused by the probe to the local plasma parameters is minimal and the measured parameters faithfully represent the plasma parameters in the absence of the probe. One of the ways to minimize the disturbance to the plasma is to use a very fine probe tip and operate the probe mostly in the ion attracting mode such that the current collection by the probe is minimal. The usage of a fine probe tip reduces the current collected by the probe. A very low probe current increases the demand on the measuring circuit, which further requires special attention to ensure a good signal to noise ratio.

In a dusty plasma environment, the negatively charged dust particles easily get attracted by the positively biased probe. These dust particles tend to stick to the surface of the probe and reduce its conducting surface area. This leads to an alteration of the probe I-V characteristics which makes determination of density from the probe current difficult.

Our experiments in dusty plasma are being carried out at high gas pressures. The probe operation at high pressures demands to consider the effect of ion-neutral collisions that may increase or decrease the probe collection current depending upon the relative values of ion-neutral mean free path and sheath thickness. The Langmuir probe system used in our experiments for measuring the plasma parameters addresses all the above stated problems comprehensively. The different solutions that have been employed to solve the above mentioned problems are discussed in this chapter.

3.2 Single Probe I-V characteristics

The variation of the current collected by a Langmuir probe with different bias potentials is represented by the I-V characteristics. Figure 3.1 shows the I-V characteristics of a typical Langmuir probe operated in collisionless plasma. I-V characteristics can be qualitatively understood by inspecting the motion of electrons and ions to the probe at different probe potentials. If an electrically isolated Langmuir probe is placed in the plasma, then the probe will charge negatively until reaching a potential at which the net current to the probe becomes zero. This potential at which the net probe current becomes zero is called the “floating potential” (V_f). At floating potential, the electron and ion flux to the probe becomes equal. When the probe potential is more negative than the floating potential then the probe attracts ions and repels electrons more strongly resulting in a net current dominated by ions. As the negative bias to the probe is increased further, the probe current saturates since the probe repels all the nearby

electrons and collects all the ions reaching probe sheath. This maximum ion current is called the ion saturation current.

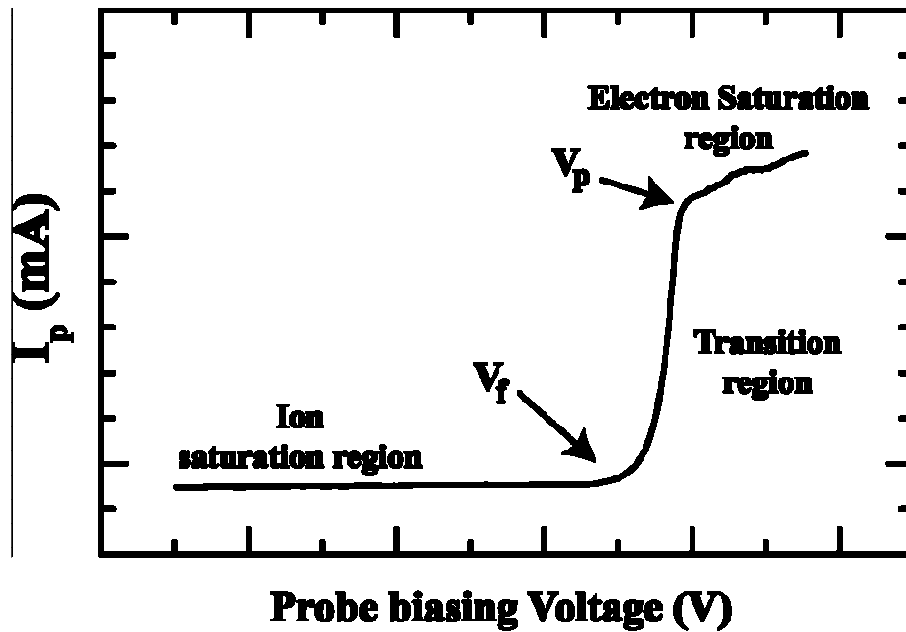


Figure 3.1: Typical I-V characteristics of a single Langmuir probe

When the probe potential is made more positive with respect to the floating potential, the electron current collected by the probe increases rapidly whereas the ion current gets decreased. This region of the I-V characteristics is called the transition region. On increasing the probe potential further, the probe acquires a potential equal to the plasma (space) potential (V_p). At this potential, no electric field (no sheath) exists between the probe surface and the plasma. Both ions and electrons impinge upon the probe surface by the virtue of their random motion. Because of higher mobility of electrons, the current collected by the probe is dominated by electrons at plasma potential. Plasma potential is represented by the knee of electron saturation region as shown in Figure 3.1. At potentials higher than the plasma potential, the probe starts attracting the electrons very strongly. All the electrons reaching the probe sheath are collected by the probe. The current collected by the probe saturates and this region of the I-V characteristics is

called the electron saturation region. However, unlike the ion saturation region, the probe current is not parallel to the voltage axis in electron saturation region, rather the probe current increases slowly with an increase in the probe potential. This is due to expansion of the probe sheath at higher probe potentials. As a result of which the effective current collecting area of the probe increases.

Over the years different theories have been formulated based on the trajectory of electrons and ions in the vicinity of a probe to quantitatively estimate the current collected by the probe at different operating regimes of the Langmuir probe for the determination of plasma parameters. The motion of the electrons and ions collected by a Langmuir probe depends on the parameters mentioned below:

1. Dimensions of the probe (for cylindrical probe, its radius (r_p) and length (l_p))
2. Mean-free-path of ions (ℓ_i) and electrons (ℓ_e)
3. Debye length of the plasma (λ_{De})
4. The anisothermicity parameter ($\tau = \frac{T_e}{T_i}$)

Except the above mentioned parameters, the shape of the Langmuir probe also significantly alters the analytical formulations describing the current collection by the probe. Langmuir probe is generally constructed in many geometric shapes: spherical probe, cylindrical probe and planar probe etc. But out of these different geometries, the cylindrical geometry is widely used as it is easy to make. Hence, depending on the geometry of the probe and the above mentioned parameters one may select a suitable probe theory to interpret the I-V characteristics and determine the plasma parameters.

3.3 Theories for interpreting Langmuir probe characteristics

Considering that DC glow discharge plasma can be operated over a wide range of operating pressure and plasma density, it is very important to wisely choose a suitable probe theory for accurate interpretation of the probe data. In this section, a brief description of the various probe theories available and their validity at intermediate pressure range ($\sim 90\text{--}350\text{ Pa}$) and low densities ($10^8 - 5 \times 10^9\text{ cm}^{-3}$) for the interpretation of the probe data is provided.

Over the past several decades, a number of theories have been formulated for interpretation of the I-V characteristics of Langmuir probe. In 1926, Mott-Smith and Langmuir [60] proposed the Orbital Motion Limited (OML) theory for interpreting the Langmuir probe data as shown in Figure 3.2. They assumed the orbital motion of charged particles, moving with constant energy and momentum in low-density plasmas, around the probe in the space charge sheath. It is assumed that the probe radius r_p is much smaller than the Debye length λ_{De} and the mean free path is much greater than Debye length.

Allen, Boyd and Reynolds (ABR) [61] performed calculations for spherical probes for two situations namely thin sheath for which $\lambda_{De} \ll r_p$ and a thick sheath for which $\lambda_{De} \sim r_p$. They assumed the ion to be cold and considered ions to perform radial motion towards the probe surface after entering into the sheath region at Bohm velocity. Hence, every ion entering the sheath gets collected by the probe. In 1965, Chen [62] extended ABR model of cold ion collection for cylindrical probe geometries, thus, making it possible to interpret cylindrical Langmuir probe characteristics using ABR theory.

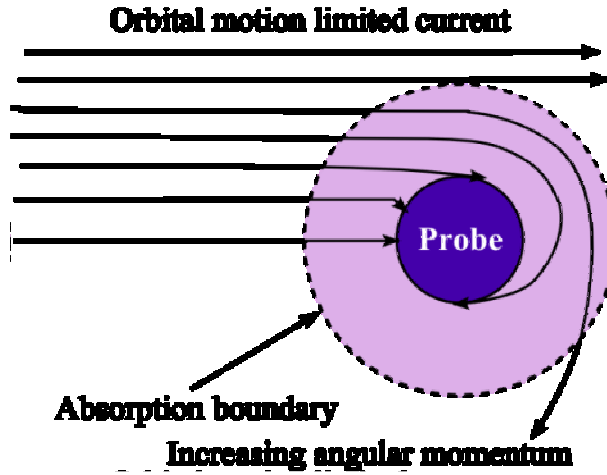


Figure 3.2: The schematic showing the orbital motion of the ion inside sheath region in a collisionless regime. The sheath boundary is well-defined and outside the sheath region, the plasma is assumed to be perfectly neutral.

Laframboise [63] extended the Langmuir probe theory further by considering ions having Maxwellian distribution in plasma. This represents the most detailed description of current collection by the probe in the absence of collisions. Analytical formulae which fit Laframboise's numerical results were provided by Kiel [64], Peterson and Talbot [65], Steinbrüchel *et al.* [66,67,68], Mausbach [69] and Chen [70]. However, Laframboise's results are not very helpful from the point of view of our experiments as most of the experiments have been carried out at low density and high pressure regime as a result of which collisions are expected to occur within the sheath. Neither of the above mentioned theories takes into account the effect of collisions for determining the current collected by a Langmuir probe. Hence, one must take into account the effect of collisions on the collected probe current.

In general, the ion-neutral collisions can affect the probe collection current in two ways:

1. As the ions collide with neutral in the sheath, they lose their kinetic energy. This result in destruction of their orbital motion and their trajectories become nearly

radial, as shown in Figure 3.3 (a). Thus, the ions after losing their energy get collected by the probe and therefore, results in an increase in the probe current. In this regime, the probe current increases with an increase in the ion-neutral collisionality and reaches maxima when the ion-neutral mean free length becomes equal to the sheath thickness [71,72]. This effect predominates at lower pressures.

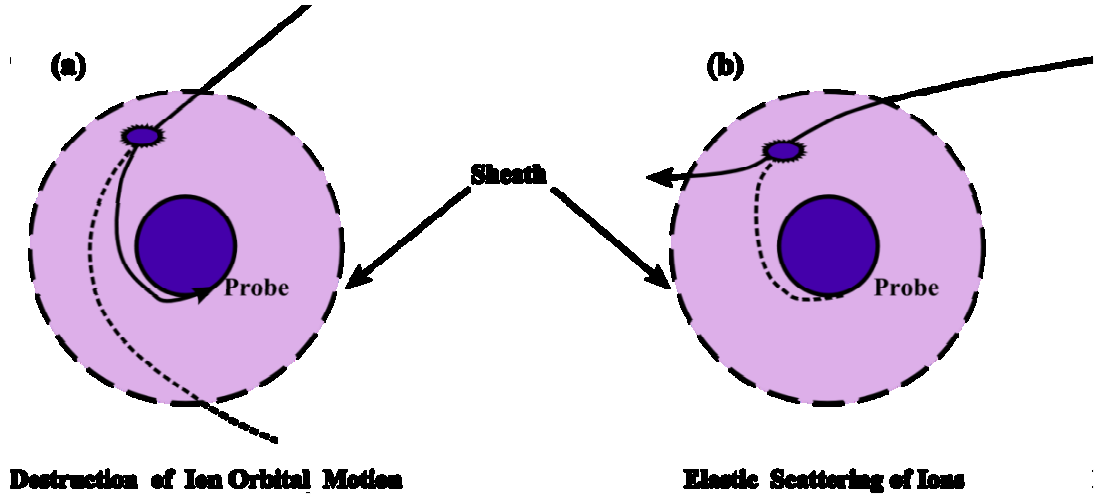


Figure 3.3: The schematic shows the influence of ion-neutral collisions on the probe collection current; a) represents the destruction of orbital motion of the ions inside the sheath leading to an increase in the collection current whereas, b) represents the elastic scattering of ions inside the sheath leading to a decrease in the probe current.

2. As the pressure increases, elastic scattering of the ions inside the probe sheath (as shown in Figure 3.3 (b)) increases due to an increase in the frictional force on the ions and decreases their velocity towards the probe surface. This leads to a decrease in ion current collected by the probe surface [73,74,75,76]. The elastic scattering of ions is more dominant at high pressures.

A number of theories have been formulated to address the effect of collisions under different operating regimes. The various ranges of Knudsen number $\left(K_i = \ell_i/r_p\right)$,

Debye number $\left(D_\lambda = r_p/\lambda_{De}\right)$ and ℓ_i/λ_{De} describes the well-known domains of operation and are mainly classified into two main categories:

A. Classical regime (corresponding to $K_i \gg 1$)

- i. $\ell_{i,e} \gg r_p \gg \lambda_{De}$, collisionless thin sheath
- ii. $\ell_{i,e} \gg \lambda_{De} \gg r_p$, collisionless (orbit limited) thick sheath
- iii. $\lambda_{De} \gg \ell_{i,e} \gg r_p$, collisional thick sheath (low and intermediate plasma density)

B. Continuum regime (corresponding to $K_i \ll 1$)

- i. $r_p \gg \lambda_{De} \gg \ell_{i,e}$, Collisional thin sheath
- ii. $\lambda_{De} \gg r_p \gg \ell_{i,e}$, Collisional thick sheath
- iii. $r_p \gg \ell_{i,e} \gg \lambda_{De}$, Collisionless thin sheath (high plasma density)

From the above classification, it is clear that the condition $K_i \gg 1$ does not necessarily mean that the sheath is collisionless. But it is decided by the relative magnitudes of the $\ell_{i,e}$ and λ_{De} . For example, if $\ell_{i,e} > \lambda_{De}$, then the probe sheath is collisionless whereas for $\lambda_{De} > \ell_{i,e}$, it is collisional. However, in the continuum regime (i.e., $K_i \ll 1$), the probe suffers a large number of collisions with the neutrals, but still the sheath may be collisionless depending upon the relative magnitudes of λ_{De} and $\ell_{i,e}$. A very small value of ion Knudsen number implies collisional plasma while a large value indicates the collision-free regime. The anisothermicity parameter, τ (the ratio of electron temperature to the ion temperature), represents the level of thermal non-equilibrium between the electrons and ions in the plasma; $\tau = 1$ represents a plasma that is in

complete thermal equilibrium, whereas $\tau^{-1} \rightarrow 0$ yields the cold ions with frozen flow situation.

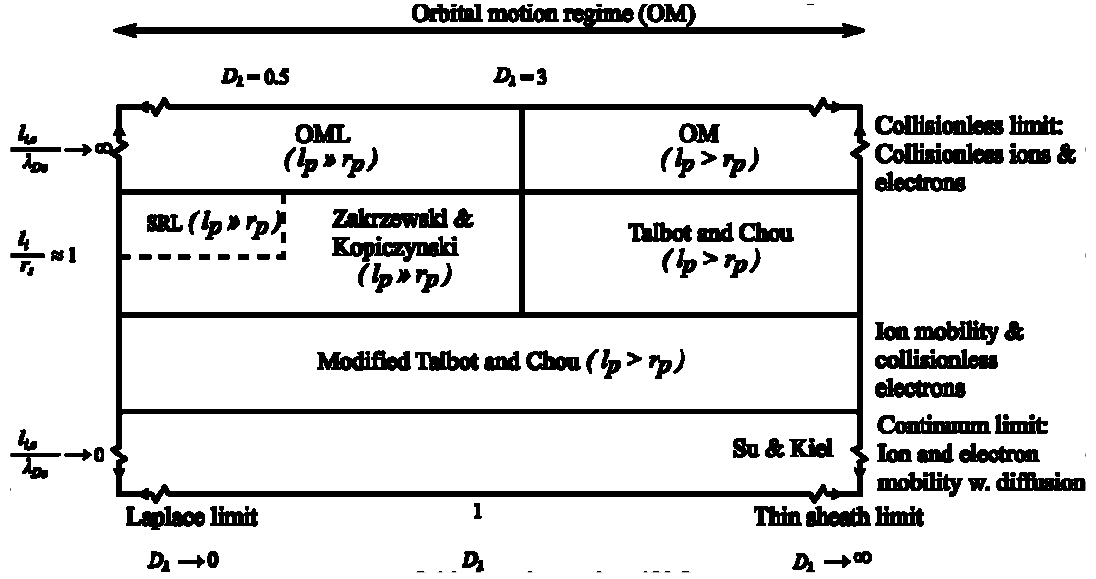


Figure 3.4: The different Probe theory regimes for plasma density determination under different operating conditions.

A complete picture of the different theories that can be used under different conditions is provided in Figure 3.4. Zakrzewski and Kopiczynski [72] described the effect of increase in ion collection by the probe due to destruction of orbital motion for $0.5 \leq K_i < \infty$ and $r_p/\lambda_{De} < 3$. They expressed the collisional probe current in terms of the collisionless Laframboise current so that it can be easily used for determining the plasma density from the experimental data. In their theory, Zakrzewski and Kopiczynski successfully predicted the maxima in the probe ion collection when the ion-neutral mean free path becomes equal to the sheath thickness. However, one cannot use this theory for cases with $K_i < 0.5$. Chou et al [75] proposed a theory for the ion collection by the spherical probes for any arbitrary Knudsen number and a wide range of r_p/λ_{De} that was further extended by Talbot and Chou [76] for cylindrical probes.

However, this theory did not predict any maxima in the probe collection current as it does not take into account the increase in the ion collection because of orbital motion destruction arising due to ion-neutral collisions in the probe sheath. In 1994, Tichy *et al.* [77] combined the Zakrzewski and Kopiczynski theory [72] and the kinetic theory by Talbot and Chou [76] for cylindrical probes and named it as “modified Talbot and Chou” model. The advantage of “modified Talbot and Chou” model is that it is applicable for any arbitrary Knudsen number i.e., $0 \leq K_i < \infty$ as long as the orbital Motion Limited model is valid i.e. $r_p/\lambda_{De} < 3$. This model describes the increase in ion collection to the probe due to destruction of orbital motion in the same way as by Zakrzewski and Kopiczynski theory [72] whereas the decrease in ion collection due to elastic scattering of ions is calculated here using Talbot and Chou theory. In this theory, at an arbitrary value of Knudsen number (K_i), the measured ion current (I_+) is normalized using the factor I^* so that

$$I_+^* = \frac{I_+}{I^*}, \quad (3.1)$$

where I^* is the probe collection current in the absence of ion-neutral collisions and is given by

$$I^* = A_{probe} n_i e \sqrt{\frac{k_B T_e}{2\pi m_i}}. \quad (3.2)$$

with m_i as the ion mass and A_{probe} as the surface area of the probe. I_+^* is a function of Knudsen number, $K_i \left(= \ell_i/r_p \right)$, Debye number, $D_\lambda \left(= r_p/\lambda_{De} \right)$ and the anisothermicity parameter, τ . The continuum regime of probe operation (in case of collisional thin sheath) is discussed by Su *et al.* [78] where both the electrons and ions

are assumed to be mobility limited. However, this regime is out of the scope of this work and will not be discussed here.

Depending upon the surrounding plasma conditions, one can choose to work with any of the above described theories. However, dusty plasma experiments are generally carried out in low density plasmas. In the present case, we are dealing with low plasma densities ($10^8 - 10^9 \text{ cm}^{-3}$) that means large Debye lengths and hence, a broad sheath. Thus, we will mainly concentrate on the theories based on thick sheath model. Also in most of our experiments, the working pressure regime is such that the ions are either partially collisional or in the collisional state *i.e.*, the ion mobility is restricted due to their collisions with the neutral atoms. Whereas, the electrons are always in the collisionless regime as the electron-neutral collision mean-free-paths are usually much larger than that of ions. Hence, for determining the plasma density from ion current collisional thick sheath theory is employed.

3.4 Probe design and construction

The design of a Langmuir probe to be used for measuring plasma parameters in low density cold plasma is governed by a number of factors. The dimensions of the probe to be used for acquiring the I-V characteristics should as small as possible such that current drawn from the plasma by the probe is very less. The lowest value of the current that can be drawn by the probe and hence the lower limit of the characteristic probe dimension is determined by the requirement to enough current such that a substantial signal to noise ratio can be ensured for the entire expected operating regime of the probe. The ratio of the probe dimension and other parameters like Debye length, collisional mean free path should be such that a well-defined theory exists for interpreting the probe characteristics.

The Langmuir probe dimensions must be carefully designed to minimize the effect of the probe holder on the Langmuir probe characteristics. The thickness of the space charge sheath around the insulated probe holder is usually of the order of Debye lengths. Therefore, the length of the Langmuir probe used should exceed this thickness considerably and the diameter of the probe holder should be around the diameter of the probe wire in order to minimize the error that arises due to collection of charged particles from the plasma volume disturbed by the probe holder within reasonable limits.

The experiments have been carried out in high pressure dc glow discharge plasma in grounded cathode configuration. In such experimental conditions, the potential in the positive column with respect to the grounded cathode can be around ~ 250 V. Hence, while designing a Langmuir probe one must ensure that the grounded metallic shaft of the probe feedthrough is never in contact with the plasma. Otherwise, the metallic shaft will act as an electrode and cause local discharge, which may adversely affect the plasma.

In our experiments, the expected plasma density and electron temperature, in the region of dc glow discharge plasma in which the probe measurements are to be carried out, are in the range of $\sim (10^8 - 5 \times 10^9) \text{ cm}^{-3}$ and $\sim (1 - 3) \text{ eV}$. These parameters will result into an electron Debye length of $\sim 0.2 \text{ mm}$. Thus, for satisfying the thick sheath working regime, the probe dimensions should be smaller than 0.2 mm . Thus, we choose the dimensions of the cylindrical Langmuir probe are fixed as diameter $\sim 0.125 \text{ mm}$ and length $\sim 6 \text{ mm}$ (with total probe area, $A_{\text{probe}} \sim 2.37 \text{ mm}^2$). For the pressure range of operation in our experiments, the value of Knudsen number (K_i) varies from 0.5 to 0.2 and the value of Debye number (D_λ) varies from 0.1 to 0.45. This range of plasma operation falls within the range of validity of “modified TALBOT and

CHOU model” [77] of positive ion collection by a cylindrical probe. Thus, the value of plasma density at intermediate and high pressures is estimated using this theory.

The probe is made using a Tungsten wire and is inserted into the plasma using a Huntington made linear translator feed-through. A very thin non-machinable ceramic tube of outer diameter $\sim 0.8\text{ mm}$ and length $\sim 35\text{ mm}$ is used as (non-conducting) probe shaft material to shield the probe for minimizing the disturbance caused by the probe shaft. A picture of the single Langmuir probe along with the insulating ceramic shaft is shown in Figure 3.5. Axis of the cylindrical probe is kept parallel to the plane of the electrode surface for determining the radial variation in the plasma parameters as shown in Figure 2.2.

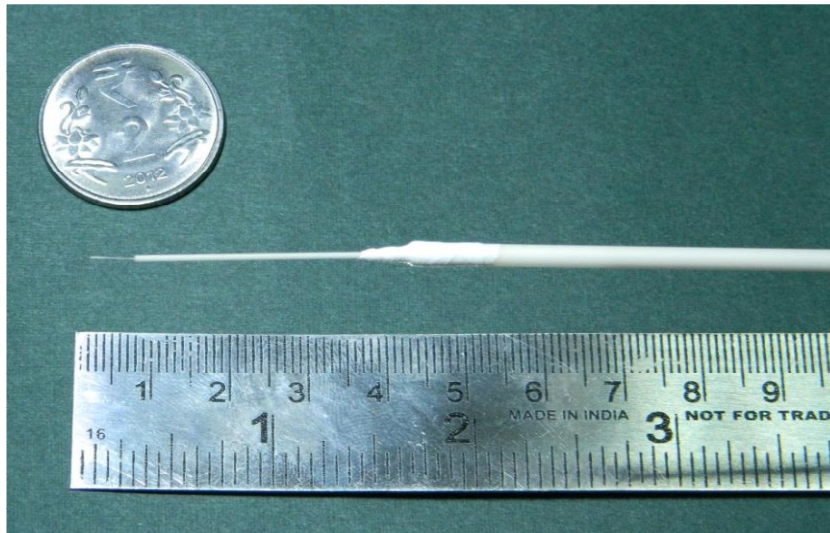


Figure 3.5: Picture of the Single Langmuir probe employed for determining the plasma parameters.

3.5 Specially Designed Langmuir probe circuit to prevent its contamination

The Langmuir system is specially designed for operation in dusty plasma environment. Dust particles present in complex plasma environment generally acquire high negative charges owing to the higher mobility of electrons. These negatively charged dust

particles are easily attracted by a positively biased probe. The dust particles tend to stick on the probe surface and reduce the current collecting area and thus, leading to misinterpretation of the probe data. Figure 3.6 (b) shows the light microscope image of cylindrical Langmuir probe after carrying out measurements in complex plasma [79,80]. Although the depth of the focus is small, single dust particles ($r_d = 1.74 \mu m$) which stick to the surface of the probe tip can be easily identified.

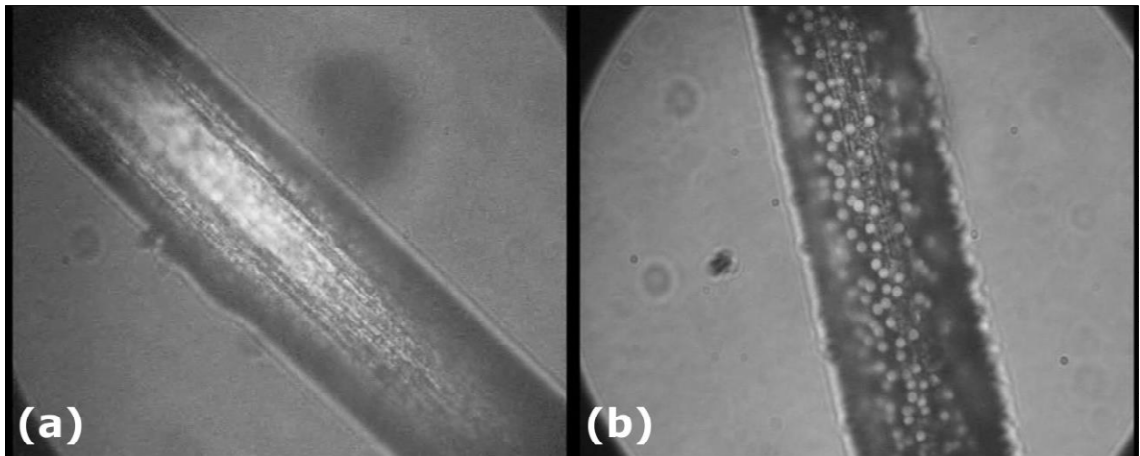


Figure 3.6: Light microscope image of Langmuir probe (a) before use and after use (b) in complex plasma [79]

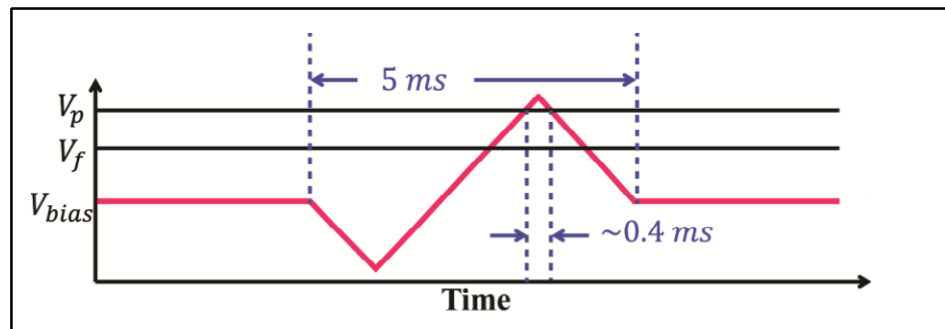


Figure 3.7: A Single cycle of triangular wave superposed on the DC bias applied to the Langmuir probe.

In order to prevent the contamination of the probe surface by negatively charged dust particles, the probe is held at a dc bias much less than the floating potential, such that the probe repels the negatively charged dust particles. Probe I-V characteristics are

acquired by applying a single triangular waveform of frequency much higher than the dust plasma frequency such that the dust particles are unable to respond to the momentary positive potential applied to the probe.

Figure 3.7 shows the triangular waveform applied to the probe. The frequency of the triangular pulse is $\sim 200 \text{ Hz}$, the dust plasma frequency ($f_{\text{dust-plasma}}$) in our case is $\sim 14 \text{ Hz}$ ($f_{\text{dust-plasma}} / f_{\text{RAMP}} \sim 0.07$). Since the fundamental frequency of the triangular waveform is much higher than the dust plasma frequency, the dust particles in the plasma are unable to respond. Additionally, the time for which the probe strongly attracts the dust particles (i.e. the duration of time for which the probe is positive with respect to plasma potential) is $\sim 4.5 \text{ ms}$ which is much faster than the dust plasma response time (i.e., inverse of dust plasma frequency). Thus, the dust particles are not expected to get attracted to the probe anymore, which is found to be true experimentally also. In our experiments, the Langmuir probe bias is varied in the range $\sim (170 - 230) \text{ V}$, depending upon the voltage applied between the cathode and anode electrodes, so that it attracts the pure ion current at voltages much lower than floating potential and a pure electron current at high bias applied to it.

Figure 3.8 shows the effect of dust contamination on the Langmuir probe I-V characteristics on the ion-saturation region under similar discharge conditions. A fast time varying probe potential may introduce an unwanted signal in the probe measuring circuit. For example, time variation of potential on a conductor kept near a grounded conductor generates a displacement current between the conductor connected to the probe and other grounded conductors. This displacement current gets added to the legitimate probe current collected from the plasma and pollutes the measurement of the probe current if not minimized sufficiently.

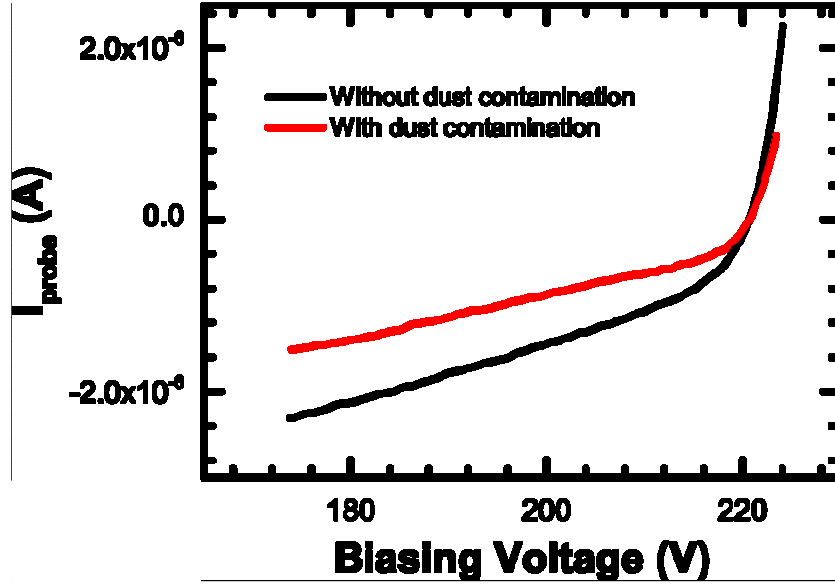


Figure 3.8: The effect of dust contamination on the ion saturation part of the probe I-V characteristics under similar discharge conditions

Figure 3.9 (a) shows a typical single Langmuir probe circuit. The probe circuit consists of a triangular wave generator, a current measuring resistance R_m and a coaxial cable connecting the current measuring resistance to the probe tip. Figure 3.9 (b) shows the equivalent circuit of the Langmuir probe circuit. The coaxial cable is replaced with its equivalent circuit. However, the cable inductance (L_c), resistance (r_c) and conductance (G_c) can be neglected for our frequency of operation. Figure 3.9 (c) shows the simplified equivalent circuit of the Langmuir probe operated by sweeping the bias voltage in the absence of plasma. I-V characteristics are acquired by sweeping the biasing voltage of the Langmuir probe and measuring the probe collection current at different bias voltage. Swift variations of the potential in the central conductor of the coaxial cable with respect to the grounded outer shield results in displacement current is given by $I_{Dis} = C_c \times dV_{in}/dt$, where C_c is the cable capacitance.

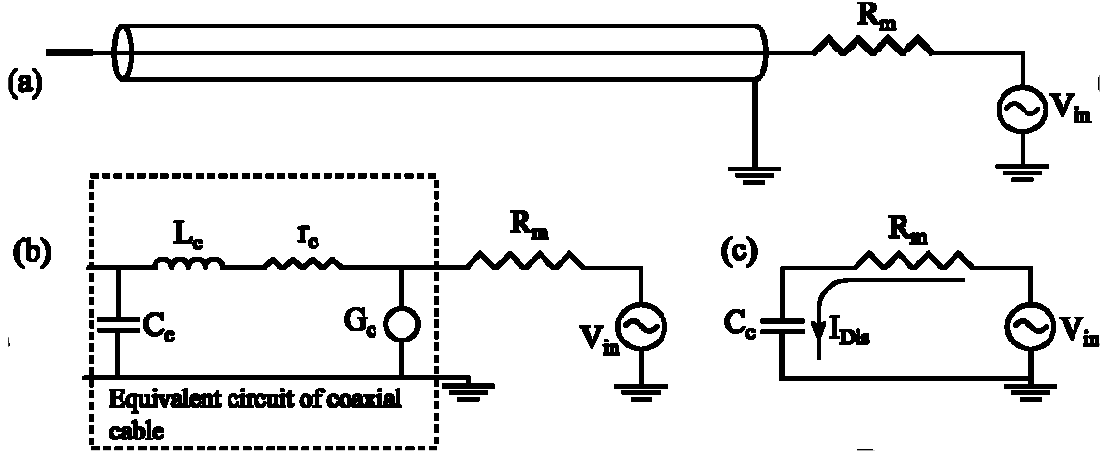


Figure 3.9: (a) A typical Langmuir probe circuit, (b) Equivalent circuit of the Langmuir probe circuit, (c) Equivalent probe circuit after neglecting cable inductance (L_c), cable resistance (r_c) and cable conductance (G_c).

A commonly used coaxial cable for wiring a Langmuir probe circuit has a capacitance 100 pFm^{-1} between the inner conductor and the outer shield. Generally, Langmuir probe cable in the laboratory is few meters long. If one considers a 2 m long Langmuir probe cable and 100 V sweep at a frequency of 100 Hz , the displacement current comes out to be $2 \mu\text{A}$ $\left[I_{Dis} = (200 \times 10^{-12} \text{ F}) \times \left(\frac{100\text{V}}{10^{-2}\text{s}} \right) = 2 \times 10^{-6} \text{ A} \right]$ which is comparable to ion saturation current obtained using a thin probe for low density collisional plasmas.

In the past, some researchers have overcome the displacement current by using the dual cable method [81,82] where one cable, connected to the probe, is active, while the other acts as a dummy cable. Both of these cables of equal lengths laid parallel to each other and are swept simultaneously. By subtracting the signal acquired from the dummy cable from that of the active cable using a differential amplifier. One can measure the probe current free from the displacement current. However, this method requires complicated electronic circuits. So, instead of using the dual cable method, we propose the usage of

a triaxial cable. The implementation of a Langmuir probe circuit using a tri-axial cable is simple and easy to use.

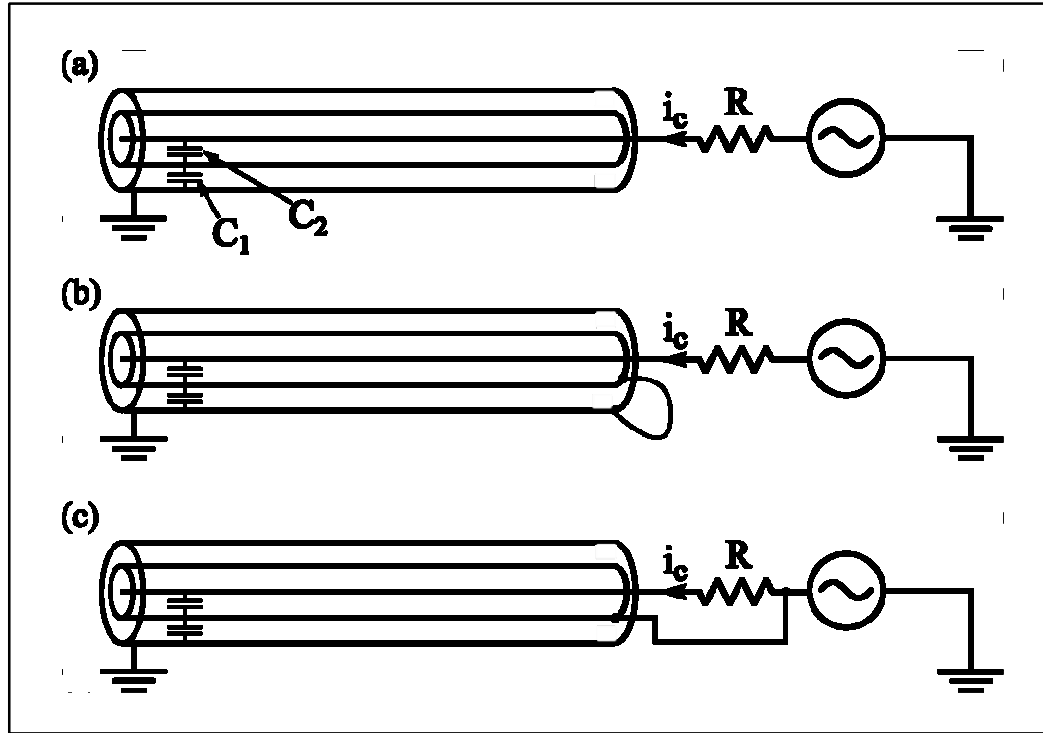


Figure 3.10: Various arrangement of a triax cable for carrying out the Langmuir probe current measurements.

A triaxial cable typically comprises of a central conductor and two coaxially placed outer shields isolated from each other. For simplicity, the inner shield is called as the guard and the outer shield as the shield. The effective capacitance between the guard and shield of a triaxial cable is $[C_1 C_2 / (C_1 + C_2)]$. By driving the guard with the same voltage as the inner conductor, the capacitive current between the inner conductor and the guard can be drastically reduced. We demonstrate it experimentally using a current measuring resistance and a function generator connected in series. Figure 3.10 shows three configurations in which the triaxial cable can possibly be used experimentally for carrying out Langmuir probe current measurements. In Figure 3.10 (a), the inner conductor is driven while the outer shield is maintained at ground potential and the

guard is kept floating. In Figure 3.10 (b), the inner conductor is driven while the outer shield and the guard are maintained at ground potential. In Figure 3.10 (c), both the inner conductor and the guard are driven while outer shield is grounded. In all the above cases, the inner conductor is driven by a sinusoidal signal of amplitude $\sim 6V_{pp}$ and frequency $\sim 1\text{ MHz}$ to determine the capacitive current in all three configurations.

In case (a) the effective capacitance between the inner conductor and the outer shield is a series combination of the capacitance between the inner conductor and the guard, and the guard and the outer shield. In case (b), the capacitance between the inner conductor and the guard is the effective capacitance as the outer and the guard are shorted ($C_{eq} \sim C_1$). In case (c), since the inner shield is driven by the same potential as the inner conductor, the potential difference between the inner conductor and the guard tends to zero. Hence, the capacitive current from the inner conductor to the driven guard tends to zero. Thus, it is expected that the capacitive current for the case (b) is maximum followed by case (a). The capacitive current in case (c) is expected to be minimum. Our experimental results show that capacitive current for case (a) is 2.5 mA , case (b) is 4.57 mA and case (c) is $10\mu\text{A}$, which is in good agreement with the predictions.

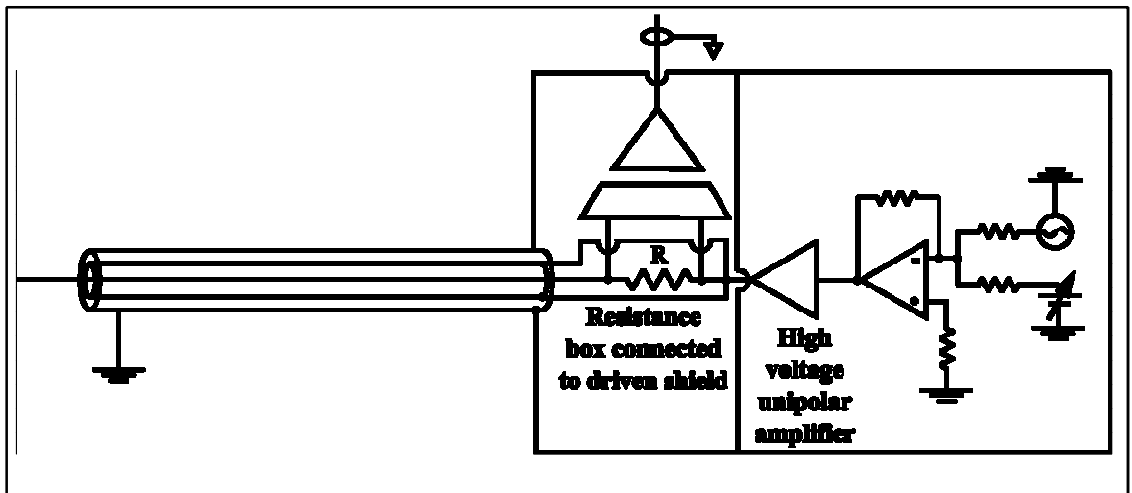


Figure 3.11: The schematic of the Langmuir probe circuit for measuring the probe IV characteristics.

Since the experiments are being conducted in DC glow discharge in grounded cathode configuration, a high plasma potential in the bulk plasma above the cathode sheath region is expected. For a typical DC discharge with anode to cathode voltage being ~ 250 V, the potential in the bulk plasma region is expected to be ~ 210 V. This is because bulk of the voltage drop occurs in the cathode sheath region. Thus, a high voltage low noise Langmuir circuit, as shown in Figure 3.11, is developed. The circuit consists of a single Langmuir probe connected to the inner conductor of a triaxial cable. A shunt resistance is attached in series to the central conductor of the triaxial cable and to a special high voltage triangular wave generating circuit. The voltage drop across the shunt resistance is measured using an isolation amplifier.

The triangular wave generating circuit consists of a high voltage amplifier PA85 being operated in unipolar mode with an adder circuit at its input. The circuit of a high voltage PA85 amplifier is shown in Figure 3.12. In the present scenario, the gain of PA85 circuit has been adjusted as ~ 40 . The adder circuit adds a single cycle triangular waveform to a DC voltage. The DC bias to the probe is kept continuously on to ensure that the probe is always biased at a fixed voltage much below the floating potential. This ensures that the probe does not attract any negatively charged dust particles.

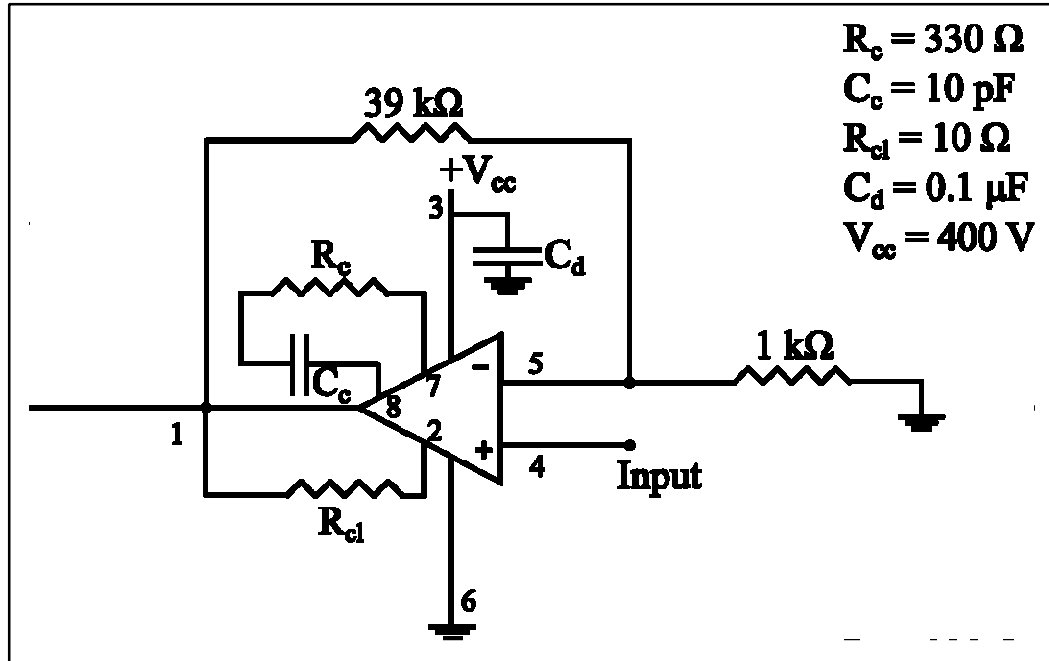


Figure 3.12: Circuit of a High Voltage amplifier.

3.6 Analysis of Single Langmuir probe I-V characteristics

A typical I-V characteristics obtained with the help of the Single Langmuir probe is shown in Figure 3.13. The background discharge parameters corresponding to the data shown in Figure 3.13 are: Argon gas pressure = $133 \, \text{Pa}$, plasma discharge current (I_{dis}) = $20 \, \text{mA}$ and voltage drop between the cathode and anode (V_{drop}) = $235 \, \text{V}$. The respective values of plasma potential (V_p), floating potential (V_f), electron temperature (T_e) and plasma density (n_i) obtained from this curve are $216 \, \text{V}$, $207 \, \text{V}$, $\sim 2 \, \text{eV}$ and $1.4 \times 10^9 \, \text{cm}^{-3}$, respectively. Figure 3.14 shows the typical algorithm, in the form of a flow chat, used to evaluate the ion density n_i at a pressure p .

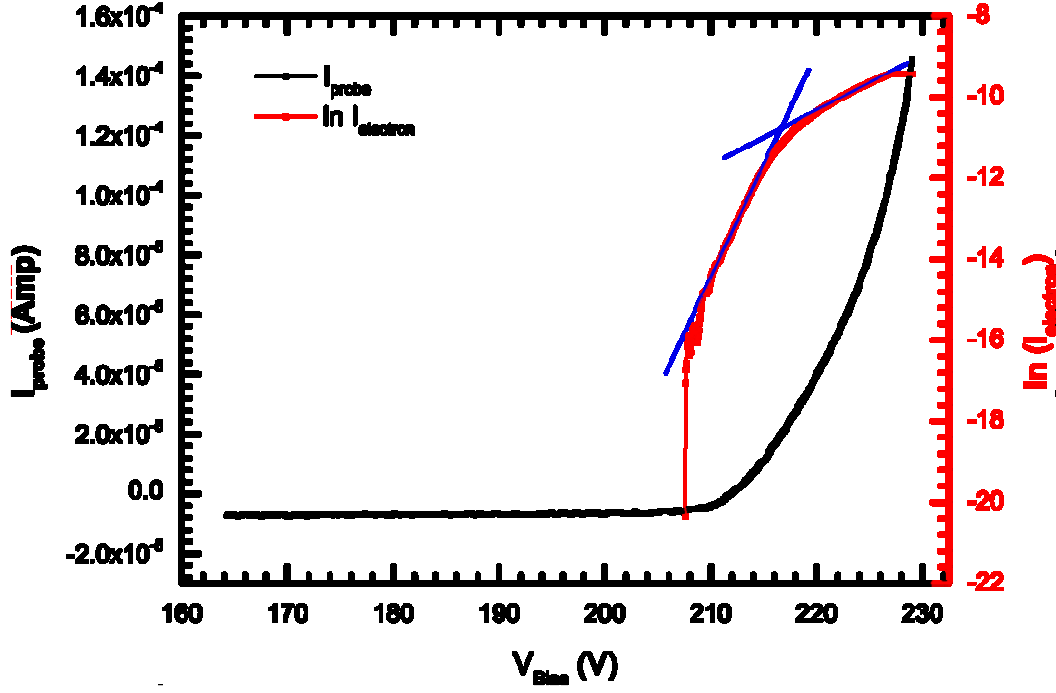


Figure 3.13: Langmuir probe characteristics at a pressure of 133 Pa and discharge current as 20 mA.

First of all, the floating potential (V_f) and plasma potential (V_p) are identified from the IV curve at a pressure p . Then the electron temperature (T_e) is evaluated from the slope of $\ln I_{electron}$ vs V_{Bias} plot at a point near the floating potential (V_f) as the effect of ions collisions with neutrals is minimum near floating potential. For the same pressure, the ion Knudsen number, $K_i \left(= \ell_i / r_p \right)$ is also calculated. Corresponding to the value of K_i , a graph between $I_+^* D_\lambda^2$ vs D_λ using the Tichy's graph [77] for an anisothermicity parameter, τ as 100 is plotted. The value of ion saturation current (I_+) is obtained at a point where $V_{Bias} = V_p - 15T_e$ from the probe IV curve. These values of T_e and I_+ are used in equation (3.1), for obtaining the value of “calculated density” (n_{ic}) using equation (3.2). The value of I_+^* is obtained for an approximate $D_{\lambda a}$ from the $I_+^* D_\lambda^2$ vs D_λ curve; $D_{\lambda a}$ =approximate Debye number.

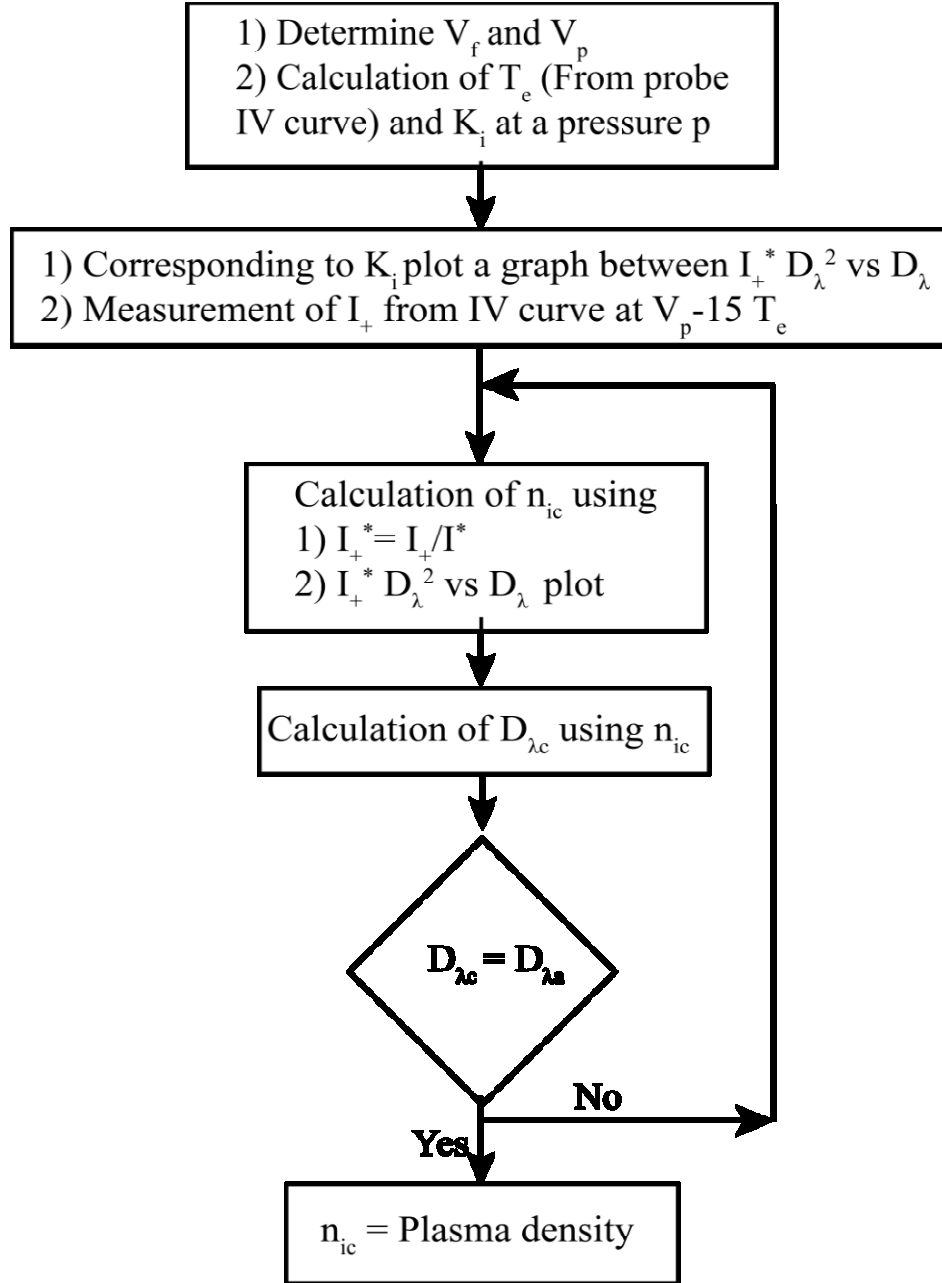


Figure 3.14: Flow chart for the determination of plasma density (n_i) at a pressure p using “modified TALBOT and CHOU theory”.

After obtaining the value of n_{ic} in this way, the value of Debye number $D_{\lambda c}$ is calculated; $D_{\lambda c}$ = calculated Debye number, and is compared with $D_{\lambda a}$. If the two values of Debye number are approximately equal, then the calculated n_{ic} is the actual plasma density otherwise the whole process is repeated again for another value of the

approximate Debye number. Hence, determination of n_i is obtained after few iterations as shown on Figure 3.14.

3.7 Double Probe

Double probe is an arrangement of two equal-sized single probes, separated by a distance (couple of Debye lengths apart), immersed in plasma [83]. When a voltage is applied to these two probes with respect to each other, the obtained IV characteristics resembles the ion current part of the single probe characteristics in both the polarities of the applied voltage. The major advantage offered by the double probe is that it does not require any reference electrode for measurements (unlike the case with single Langmuir probe) and can be employed to work in electrode-less (RF) plasmas. It is usually employed to measure the electric field in plasma, but it can also be used to determine electron temperature and sometimes, plasma density too. In the present work, we have used the double probe for determining the local electron temperature profiles.

Let us consider two probes in the plasma having area A_1 and A_2 . Let a voltage V be applied between the two probes. Let V_1 and V_2 be the potential of probe 1 and 2, respectively such that

$$V = V_1 - V_2 > 0. \quad (3.3)$$

Let i_{1+} , i_{1-} , i_{2+} and i_{2-} be the ion and electron currents to the probes 1 and 2, respectively. The system of these two probes is floating and this demands that

$$i_{1+} + i_{2+} - i_{1-} - i_{2-} = 0. \quad (3.4)$$

Consider the case when current I is flowing in the loop and is given by

$$\text{Current entering probe 2} + \text{Current leaving probe 1} = 2I$$

$$(i_{1+} - i_{1-}) + (i_{2+} - i_{2-}) = 2I. \quad (3.5)$$

Adding equation (3.4) and (3.5), we obtain

$$i_{1+} - i_{1-} = I, \quad (3.6)$$

$$i_{2+} - i_{2-} = I, \quad (3.7)$$

where the expressions for i_{1-} and i_{2-} are

$$i_{1-} = A_1 j_r e^{(eV_1/k_B T_e)}, \quad (3.8)$$

$$i_{2-} = A_2 j_r e^{(eV_2/k_B T_e)}, \quad (3.9)$$

here j_r is the random electron current density.

From equation (3.8) and (3.9)

$$I + i_{1-} = A_1 j_r e^{(eV_1/k_B T_e)} = A_1 j_r e^{(eV + eV_1)/k_B T_e} = \frac{A_1}{A_2} e^{(eV/k_B T_e)}. \quad (3.10)$$

Using equation (3.6) and (3.10), we obtain

$$\frac{I + i_{1-}}{i_{2+} - I} = \frac{A_1}{A_2} e^{(eV/k_B T_e)}. \quad (3.11)$$

If $A_1 = A_2 = A$, then $i_{1+} \cong i_{2+} \cong i_+$

$$I = i_+ \tanh(eV/k_B T_e). \quad (3.12)$$

This formula has been found to fit the experimental plot pretty well. Now for the determination of the temperature assuming that i_+ is independent of V

$$\frac{dI}{dV} = \frac{di_{1-}}{dV} = -\frac{di_{2-}}{dV}. \quad (3.13)$$

Using equation (3.8) and (3.9)

$$A_1 j_r e^{(eV_1/k_B T_e)} \frac{dV_1}{dV} + A_2 j_r e^{(eV_2/k_B T_e)} \frac{dV_2}{dV} = 0. \quad (3.14)$$

Rewriting equation (3.3) gives

$$1 = \frac{dV_1}{dV} - \frac{dV_2}{dV}, \quad (3.15)$$

$$A_1 j_r e^{(eV_1/k_B T_e)} \frac{dV_1}{dV} + A_2 j_r e^{(eV_2/k_B T_e)} \left(\frac{dV_1}{dV} - 1 \right) = 0. \quad (3.16)$$

At $V = 0$, $V_1 = V_2$

$$\left[\frac{dV_1}{dV} \right]_{V=0} = \frac{A_2}{A_1 + A_2}. \quad (3.17)$$

From Equation (3.13)

$$\left[\frac{dI}{dV} \right]_0 = \frac{A_1 A_2}{A_1 + A_2} j_r \frac{e}{k_B T_e} e^{(eV_1/k_B T_e)}. \quad (3.18)$$

Since

$$j_+ = j_r e^{\left(\frac{eV_f}{k_B T_e} \right)}, \quad (3.19)$$

$$\left[\frac{dI}{dV} \right]_0 = \frac{A_1 A_2}{A_1 + A_2} j_+ \frac{e}{k_B T_e}. \quad (3.20)$$

Let $i_{1+} = j_+ A_1$ and $i_{2+} = j_+ A_2$

$$\left[\frac{dI}{dV} \right]_0 = \frac{e}{k_B T_e} \frac{i_{1+} i_{2+}}{i_{1+} + i_{2+}}. \quad (3.21)$$

Equation (3.21) provides an estimation of the electron temperature. The double probe, that has been employed in the present experiments, is made up of a tungsten wire of diameter 0.5 mm and length 1 cm . The I–V characteristics of a double probe obtained at a height of 9.5 mm above the surface of cathode and at a radial location of 5.3 cm , is shown in Figure 3.15.

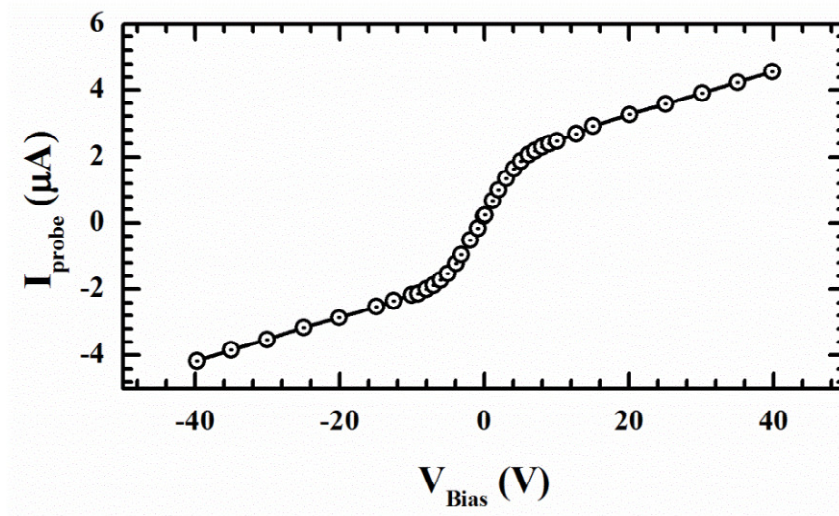


Figure 3.15: A graph of the double Langmuir probe at a height of 9.5 mm above the surface of cathode.

The double Langmuir probe is used at different heights above cathode surface corresponding to different discharge conditions for determining the radial profiles of the electron temperature. One such radial profile corresponding to a background pressure of 105 Pa at different vertical heights above the cathode surface is shown in Figure 3.16 which shows that the electron temperature profile does not possess any significant radial variation above a height of $\sim 9.5 \text{ mm}$.

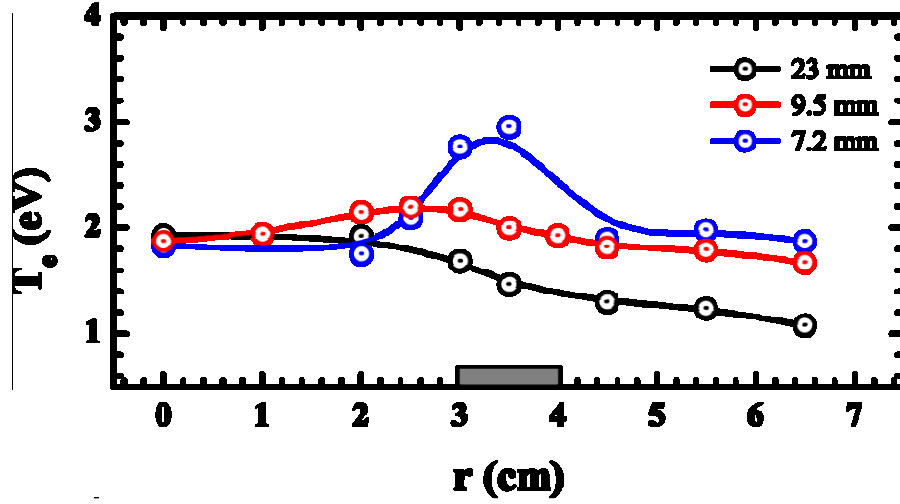


Figure 3.16: Radial profiles of electron temperature at different heights at a discharge current of 25 mA and an operating pressure of 105 Pa

3.8 Summary and conclusions

The Langmuir probe measurements in high pressure dusty plasmas are not straightforward. There exist two major issues which need attention during Langmuir probe measurements in high pressure dusty plasmas. First is the deposition of dust particles on the probe head. Being negatively charged the dust particles get attracted towards it when the probe bias rises above floating potential. The dust deposition alters the probe I–V characteristics significantly leading to gross errors in estimating the plasma parameters. Secondly, when used in high pressure ($p > 100 \text{ Pa}$) plasmas, the elastic scattering of ions due to their collisions with neutrals reduces the ion collection current and substantially decreases the signal to noise ratio. Whereas, the destruction of the orbital motion of the ion, due to their collisions with neutrals, results in an increase in the probe current. The effect of collision on ion current has to be taken into account to interpret the probe data correctly. After taking into consideration the above mentioned complications, a specially designed Langmuir probe system is described here, which is immune to dust contamination and is capable of working at high pressure

and provides us with correct estimates of plasma parameters. The biasing circuit of the probe has been suitably designed to minimize the effects of capacitive current and noise on the probe characteristics using tri-axial cable in a driven guard configuration. The method of analysis of Langmuir probe I-V characteristics is described in this chapter. Additionally, a double Langmuir probe that has been used for carrying out electron temperature measurements has also been described.

4 CHAPTER: DUST PARTICLE ROTATION

In this chapter, the poloidal rotation (vortex) of mono-dispersed dust particles in a toroidal geometry is presented. A systematic investigation on the formation of a single vortex will be presented. In section 4.1, the observation of the formation of single dust vortex is presented. In section 4.2, the PIV analysis of the still images is presented, followed by a detailed Langmuir probe measurement in section 4.3. Finally, a probable cause of the rotation is discussed in section 4.4 and summary and conclusions are provided in section 4.5.

4.1 Observation of Dust Rotation

Experiments are performed using mono-dispersed Melamine Formaldehyde (MF) particles ($6.48 \mu m$) placed on the cathode in a parallel plate DC glow discharge. The cathode is covered with the dust particles from the centre to the inner diameter of the metallic ring. Vacuum vessel is first purged with Argon gas at high pressure (~ 300 Pa) for at least 10 minutes and then pumped down to low pressures. This process is repeated several times before producing the discharge to minimize the background gas impurity level. The discharge is produced at a low pressure ($p = 20$ Pa) with a low discharge current (~ 20 mA) between the two electrodes. Initial observations of the dusty plasma illuminated by laser sheet are made by directly viewing them with naked eyes and are recorded using the sCMOS camera. At low pressures ($p = 20$ Pa), cathode sheath is observed to be more than 1 cm thick and the levitated dust particles are found to oscillate with very high amplitudes in the central region of cathode inside the metallic ring. Cathode sheath thickness decreases as the working gas pressure is increased. As the pressure is increased to 50 Pa, a stationary three-dimensional crystalline structure is visible at the centre and thick dust clouds of very fine particles are visible above the

metallic ring surface. As the particles (in these dust clouds formed above the metallic ring surface) are too small, it is very difficult to resolve the dynamics of the individual dust particles in these clouds. The presence of these fine particles might be due to the breaking of mono-dispersed micro-particles by ion bombardment.

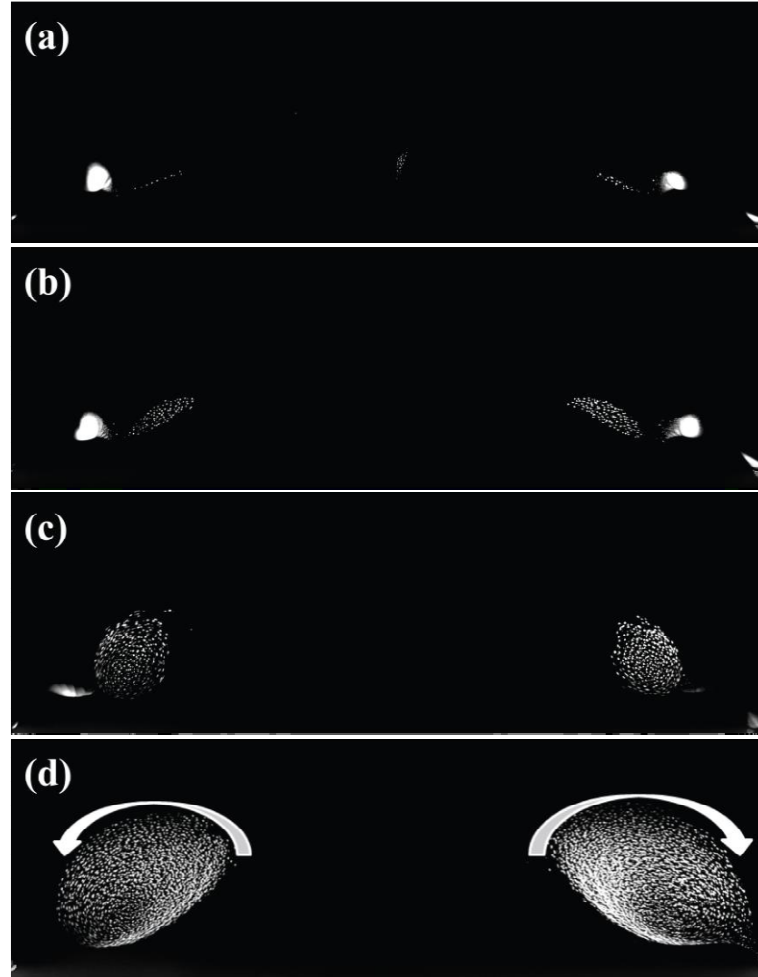


Figure 4.1: The diametrically opposite poloidal cross-sections of the dust torus in the vertical $r - z$ plane at different pressures; (a) 70 Pa, (b) 76 Pa, (c) 100 Pa, and (d) 110 Pa, respectively. The laser sheet is passed along the diameter of the cathode through the side radial port and the camera is placed perpendicular through the axial port.

As the pressure is further increased up to 69 Pa, the cathode sheath thickness decreases further. The mono-dispersed dust particles form slanted horizontal sheets of dust particles above the sheath. In addition, a stationary three dimensional crystalline

structure is observed at the centre. Beyond ~ 70 Pa pressure, the dust particles present in the slanted horizontal sheet start showing mild rotation in the vertical plane as is shown in Figure 4.1(a). At 76 Pa pressure, the dust number density as well as the extent of vertical rotation of dust particles in the slanted sheets increases; the central three-dimensional crystalline structure disappears and the size of the fine-particle dust cloud also decreases with increase in pressure as shown in Figure 4.1(b). At 100 Pa, a clear vertical rotation of the dust particles in the clouds is seen as shown in Figure 4.1(c). Two such fully grown rotating clouds at a pressure of 110 Pa are visible near the diametrically opposite sides of the metallic ring as shown in Figure 4.1(d) in $r - z$ plane [84].

For all the above observations, the vertical laser sheet was passed along the diameter of the cathode. Cathode has a circular symmetry, so it is interesting to know whether the dust clouds also have some kind of symmetry. For that the vertical laser sheet is scanned in the horizontal direction above the surface of cathode, from its centre to its edge. A top view of the schematic of the horizontal scanning of the laser sheet is shown in Figure 4.2. When the laser light is scanned in the horizontal plane from **1** to **2**, the images of two rotating dust clouds get successively closer and merge into one cloud virtually. The images of the merging of dust clouds taken with the help of a DSLR camera are shown in Figure 4.3. When the laser sheet is passed along the diameter of the electrode, two well-separated opposite poloidal cross-sections are seen (in Figure 4.3 (a)). As the laser sheet is scanned horizontally away from the diameter, poloidal cross-sections get successively closer as shown in Figure 4.3 (b)–(e). Figure 4.3 (f) shows the edge of the dust torus. Figure 4.3 confirms that the two rotating dust clouds are basically the two poloidal cross-sections of a torus illuminated by the vertical laser sheet passing along the cathode diameter.

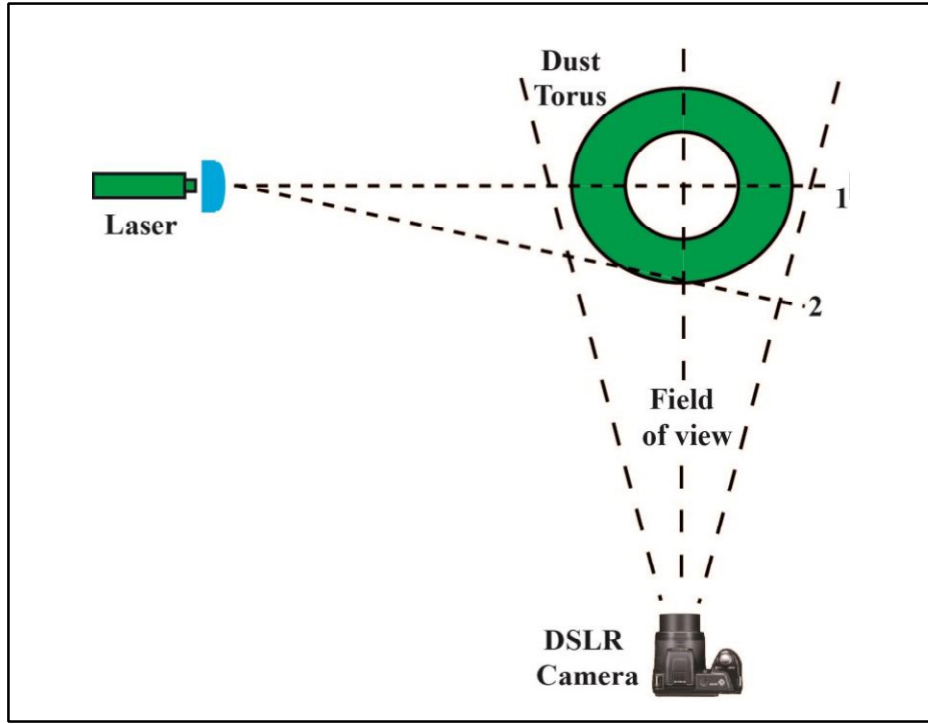


Figure 4.2: Top view of the arrangement of the camera and the vertical laser sheet, scanned horizontally to capturing the whole area of the torus.

From these images, it is clear that the dust cloud structures are toroidally continuous and this toroidal nature arises due to the circular symmetry of the electrode and the metallic ring. The dust cloud (i.e., dust vortex) is a poloidal cross-section of the toroidally continuous structure. Thus, for the rest part of the thesis, the toroidal coordinate system will be followed where z represents the vertical direction (opposite to direction of gravity), φ represents the toroidal direction and θ represents the direction of the poloidal rotation of the dust particles, respectively as shown in Figure 4.4. In the working range of pressure ($p > 100 \text{ Pa}$) and discharge current ($I_{dis} > 20 \text{ mA}$) of the present experiment, the cathode sheath is seen to be very thin (thickness $\leq 6 \text{ mm}$) and covers only a small fraction of the inter-electrode separation. While viewing the discharge through naked eyes, it is observed that the discharge conditions, with and without dust particles, are quite different. It is always desirable to look for any kind of symmetry in the system of interest as it helps us in the simplifying of the problem.

Since the dust clouds have a toroidal symmetry, so one may study any individual poloidal plane and correlate it with the rest of the structure.

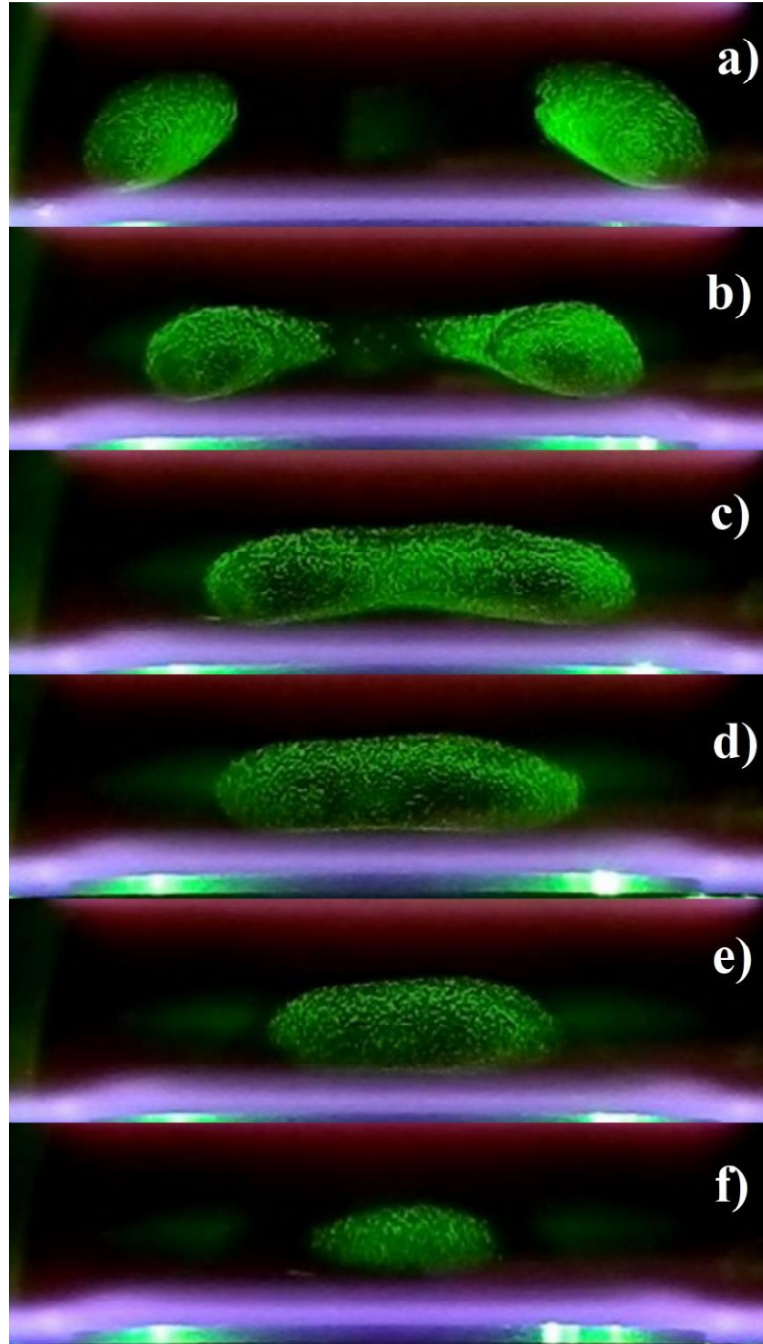


Figure 4.3: The different cross-sections of the dust toroidal structure illuminated by the vertical laser sheet when the cathode diameter is scanned from centre towards its end.

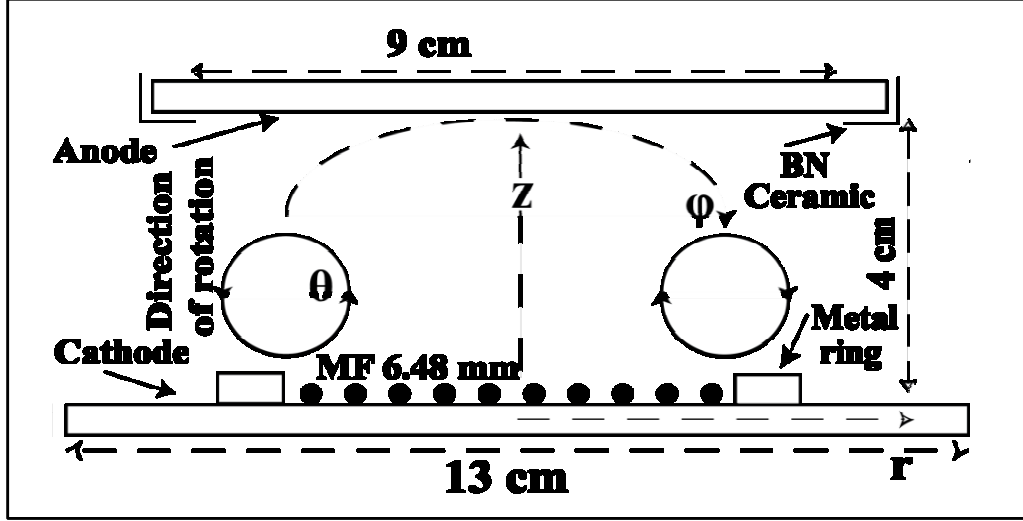


Figure 4.4: A schematic of the co-ordinate system where z represents the direction opposite to \vec{g} , ϕ represents the toroidal direction and θ represents the direction of the poloidal rotation of the dust particles above the metallic ring.

4.2 PIV analysis

In this section, we study the velocity profile of the dust particles in a poloidal plane. To analyse the velocity profile of the rotating dust clouds (vortex), Particle Image Velocimetry (PIV) technique is employed. A number of sequences of still images are stored with the help of sCMOS camera and one of these images is shown in Figure 4.5(a). PIV analysis is performed on these images to measure the particle streaming velocity. The velocity profile can be reconstructed by performing cross-correlation between two consecutive images. On each image, identical regions with the illuminated grains are decomposed into a rectangular grid of interrogation boxes. Each interrogation box is a square of $m \times m$ pixels in size, for example 32×32 pixels, 64×64 pixels, etc. A cross-correlation of two images of a single interrogation box is used to construct a displacement vector for all particles within the interrogation box. Since the time interval between the two images is known, a velocity vector for each interrogation spot can be computed.

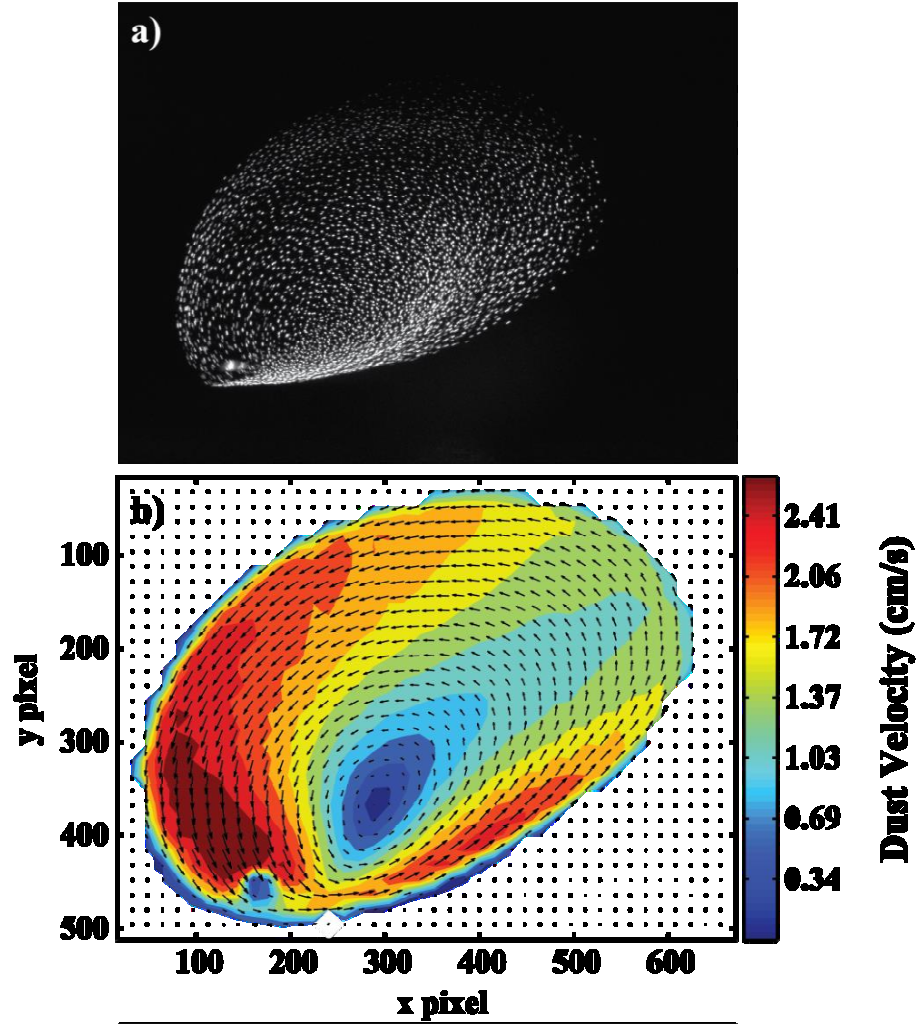


Figure 4.5: a) The still image of the poloidal cross-section of the dust torus taken with the help of sCMOS camera, and b) The dust particle velocity profile in the poloidal cross-section.

For carrying out PIV analysis, MATLAB based free software called openPIV [85] is used. A two-dimensional velocity profile of the rotating dust cloud, in the $r - z$ plane measured using openPIV software, is shown in Figure 4.5 (b). The particle motion is recorded at a frame rate of 200 *frames/s* (exposure time is set at 5 *ms*) and a total of 800 still images are recorded. Here the interrogation window size is taken as 32×32 with a 50% overlapping. PIV analysis provides a total of 799 flow fields for averaging. The average dust flow velocity profile is a representative of the majority of the flow fields. Flow velocity is seen to be rotational as indicated by the velocity vectors. It is observed that the dust velocity is not uniform throughout the cloud poloidally. As the

dust particles move towards the bottom their velocity increases and attain a peak value at the bottom. Since the dust particles move very fast at the bottom of the cloud, so they look like lines (as they travel a number of pixels in a single exposure time) as they reach near the bottom of the cloud and become faint in comparison to rest of the cloud. From the still images, it is seen that the particles appear as faint lines near the bottom of the cloud and as well-defined points at the top. For this reason, PIV analysis gives errors at bottom locations of the cloud and reasons attributed are:

- a) The dust density at locations, like (400, 450), is much higher than that at other locations.
- b) The particle (due to its appearance as a line) occupies large fraction of the interrogation box and moves a considerably large distance in a single exposure time (in two consecutive frames). The PIV velocity profiles are best obtained when the particle moves a small distance (less than 30%) across the interrogation box [8].
- c) In the PIV approach, the most likely displacement of the particles in the interrogation region is obtained by fitting the peak in the correlation plane to a Gaussian. This approach allows for the sub-pixel measurement of the displacement. However, when the streaking is observed in the image data, the result is a peak in the correlation plane that is notably broader. In this case, the Gaussian fit will still provide the most likely displacement but the error in the resulting vector will be significantly larger and the vector may not be valid.

For bottom locations, the dust particle velocity can be estimated by determining its track length in single exposure time. Using this method, the dust velocity at (1150, 650) is estimated as $\sim 7 \text{ cm s}^{-1}$. For the rest of the cloud, PIV analysis provides very accurate results. In the velocity profile analysed with the help of PIV, the dust

particles are moving in the vertical plane with a velocity of around $4 - 5 \text{ cm s}^{-1}$ towards the bottom electrode as shown in Figure 4.5 (b). The dust particle velocity has been found to be varying radially too in the cloud. At the centre of the cloud (which is close to bottom) dust velocity is minimal and increases as one move away from the centre and reaches its maximum value at the edges of the cloud. This is a velocity pattern similar to that of rotating solid bodies. Also, the centre of the dust vortices does not coincide with its geometric centre. It is shifted vertically downwards and horizontally in a direction opposite to the density gradient.

4.3 Langmuir Probe Measurements

In order to understand the cause behind the rotation of the dust particles in toroidal structures, a Langmuir probe is used to characterize the background plasma parameters. Plasma density is measured at different horizontal as well as vertical locations using a Langmuir probe at a pressure of 133 Pa . The results of the measurements are plotted in Figure 4.6. Without dust particles, it is observed that plasma density peaks inside the ring (in between the cathode centre and the ring) and falls off rapidly outside the ring towards the end of the cathode as shown in Figure 4.6 (a). With the dust particles, it is found that the radial profile of the plasma density peaked slightly outside the edge. In addition, the density gradient is steeper as compared to that without dust particles. The density has a vertical variation too. As one moves from cathode to anode, the plasma density is found to decrease (n_i at $z = 9 \text{ mm}$ is more than that at $z = 11 \text{ mm}$), as shown in Figure 4.6 (b). It attains a maximum value at a height above cathode surface (away from sheath) and then again decreases in the cathode sheath region. Presence of dielectric dust particles makes the discharge even more concentrated near the metallic ring. This results in steep density gradient near the metallic ring. Therefore, it would be

interesting to know whether plasma density gradient plays any role in the formation of rotating dust structures.

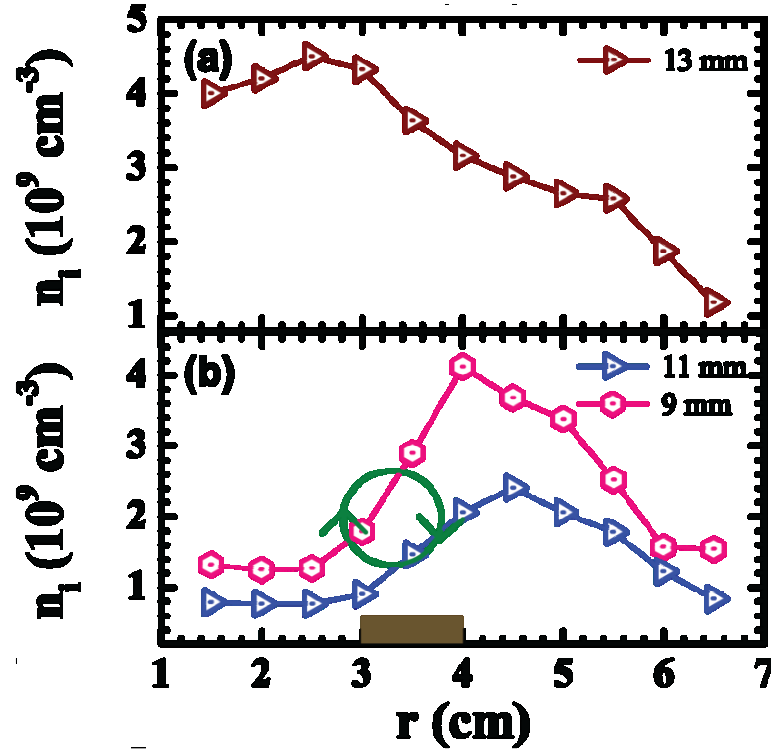


Figure 4.6: Radial density profiles a) in the absence of dust particles and b) in the presence of dust particles at two different heights above the surface of cathode

4.4 Probable Cause of Dust Rotation

Dust rotation can occur as a result of various forces acting on the dust particles in plasma. One of the main forces is due to gravity which arises due to the finite mass of the dust particles. The force due to gravity (F_g) on the micro-particles is estimated to be $2.15 \times 10^{-12} \text{ N}$ and it acts downward. In the ambient plasma with plasma screening length λ_D , the charge on the dust particle can be estimated by taking into consideration the ion-neutral collisionality, using equation (1.5), to be $8.1 \times 10^3 e^-$ for Argon plasma with $T_e \sim 3 \text{ eV}$ and $n_i \sim 3 \times 10^9 \text{ cm}^{-3}$. These micron-sized particles after getting

charged experience a repulsive force upward due to the sheath electric field and get levitated.

Besides the above discussed forces, ion drag force is also one of the very dominant forces experienced by the dust particles. In the case of dc glow discharge, the directed ion flow towards the cathode surface drags the dust particles along their way. The ion velocity has mainly two components: thermal and drift. In quasi-neutral bulk plasma at high pressures ($p \geq 100 \text{ Pa}$), the ion drift velocity is much less than the thermal velocity $v_i \ll v_{Ti}$. For frequent collisions, $\ell_i \leq \beta_T \lambda_D$, the value of the ion drag force can be estimated using equation (1.22). From the equation (1.22), it is observed that there is a strong gradient in the ion drag force ($\sim 1 \times 10^{-10} \text{ Nm}^{-1}$) at the region of strong radial density gradient. Electron temperature is found to be nearly constant radially. The strong radial gradient in ion drag force may exert a torque on the dust cloud present in the vicinity of the gradient.

Due to the ion bombardment on cathode surface, cathode heating takes place and it increases with the discharge current. Presence of finite temperature gradient can give rise to thermophoretic force. This may affect dust dynamics depending on its relative magnitude compared to other forces. In our experiments, the cathode can attain a temperature from 40°C to 65°C without water cooling. It takes more than an hour for the cathode temperature to increase up to the maximum temperature depending upon the discharge current. For example, it takes more than two hours to reach 65°C with a discharge current of 25 mA at a pressure of 120 Pa . However, our experiments are conducted for short periods. Besides, to exclude the effect of temperature gradient, experiments are carried out with actively cooled cathode. The cathode surface is maintained at room temperature. In this scenario too, the dust rotation is observed. Although, with active water cooling, temperature gradient is not expected, a

temperature gradient of $\nabla T_n \approx 1 \text{ Kcm}^{-1}$ is considered to estimate the thermophoretic force. The neutral pressure, in our experiments, is more than 100 Pa , i.e., the distance between the dust cloud and the cathode surface ($\sim 3 - 6 \text{ mm}$) is much larger than the neutral mean free path ($\sim 20 - 30 \mu\text{m}$). Therefore, the thermophoretic force can be assumed to be independent of the neutral pressure and mass of the neutral gas and is estimated, using equation (1.26), to be $1.0 \times 10^{-13} \text{ N}$, which is one order less compared to the all other forces experienced by the dust particles. Therefore, the thermophoretic force is not expected to contribute towards the rotation of dust particles. Additionally, being a conservative force, it cannot give rise to rotation of dust particles as its curl will always be zero.

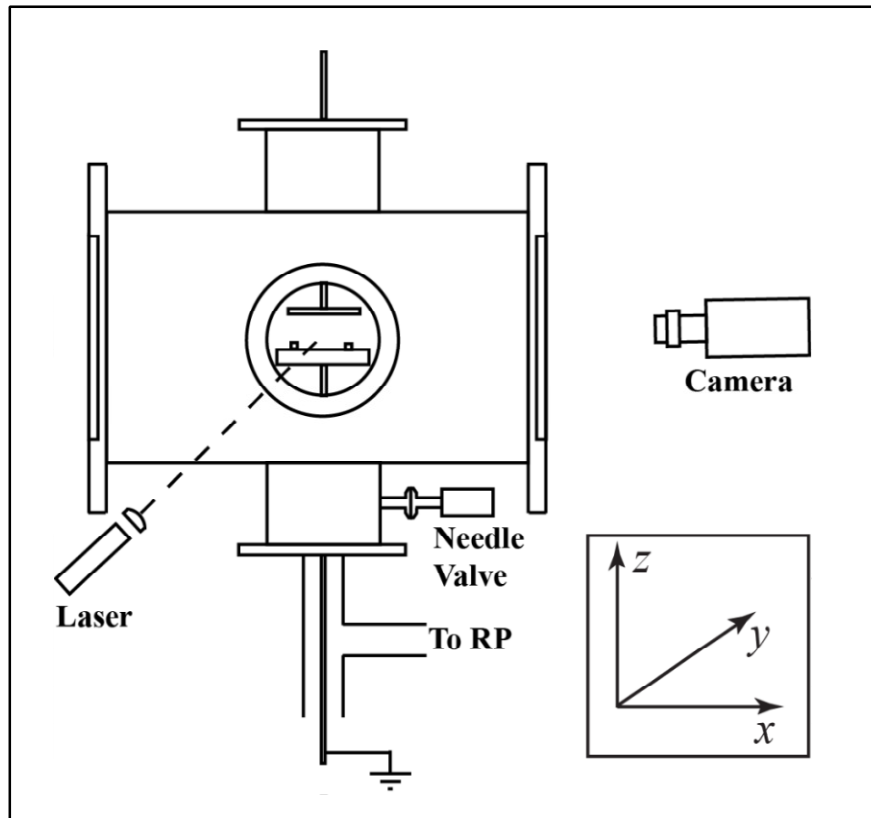


Figure 4.7: A two-dimensional schematic of the experimental set-up, clearly showing the evacuation and gas insersion through the bottom port.

Apart from thermophoretic force, two other phenomena may also occur in the presence of temperature gradient. One of these, thermal creep flow, arises because of non-

uniformly heated gas being in contact with a solid surface. In presence of a non-uniformly heated body in a rarefied gas, the gas starts flowing along the boundary in the direction of the temperature gradient. This phenomenon requires a hot boundary and occurs only at low pressures (less than 90 Pa) [53,52] near the boundary. In our case, thermal creep flow has no role, primarily as the working gas pressure is high. Other phenomenon, free convection flow is driven by buoyancy. Free convection is a phenomenon of heat transport in the fluids generated as a result of the density difference in the fluid due to temperature gradient. For free convection to be the reason behind the rotation of the dust clouds, the Rayleigh number should be of the order of few thousand [51]. Rayleigh number for our experiments is less than 1. Therefore, the working pressure range in presented experiments is high enough for the existence of thermal creep flow and low enough for the existence of free convection.

Dust particle dynamics can be affected by directed neutral flow. To mitigate this, Argon gas is fed through the bottom port. This port is connected to the rotary pump via a gate valve for evacuating the system as shown in Figure 4.7. So, only diffused gas is allowed to enter into the system. During the experiment, both the gate valve located at the mouth of the rotary pump and the needle valve (being used for feeding the gas) are closed, simultaneously. By doing so, no significant effect on the dust cloud formation and rotation is observed, as is also clear from Figure 4.8. This observation rules out the presence of any directed gas flow and its effect on the dynamics of the dust cloud. Thus, the neutral gas can be assumed to be at rest and acting as frictional background on the dust particles, resisting their motion. The value of the neutral frictional force (which is proportional to the instantaneous velocity of the dust particle) can be estimated using equation (1.23). For the observed dust velocity of 4 cm s^{-1} and neutral

gas density of $3 \times 10^{16} \text{ cm}^{-3}$ at a pressure of 133 Pa , the value of the neutral frictional force is $1.4 \times 10^{-12} \text{ N}$.

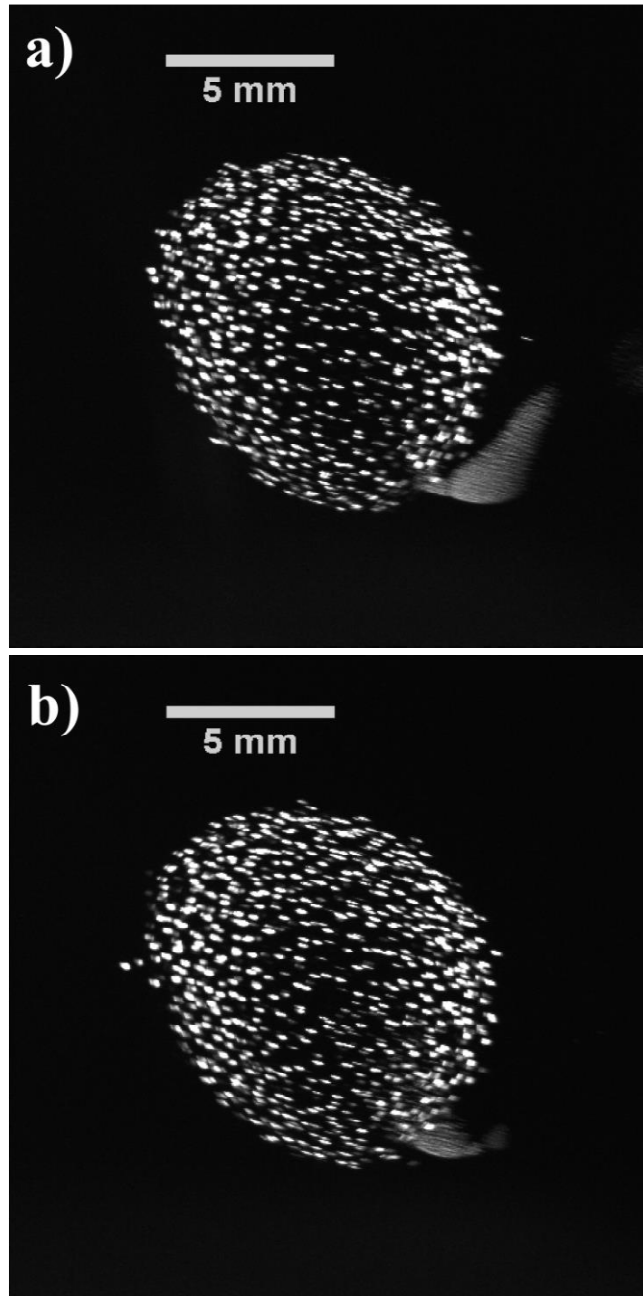


Figure 4.8: The still images taken with the help of sCMOS camera at a pressure of 124 Pa and discharge current of 26 mA represents; (a) the case when the rotary pump as well as the needle valve are disconnected to the vacuum vessel whereas (b) the case when both of these are connected to the vacuum vessel.

From the above analysis, it is clear that the main forces responsible for dust rotation in the system under consideration are downward directed sheared ion drag force, neutral drag force, and the forces due to sheath electric field and gravity. The dust particles in the cloud are observed to be flowing towards the cathode surface against the sheath electric field in a region, where the ion density and hence the ion drag force is maximum. The dust particles start moving upward near the sheath edge, where the ion drag force becomes less.

In the simplest terms, the above observations of dust cloud rotation can be interpreted as follows. The levitated dust cloud is confined effectively by a balance of the non-uniform electrostatic space potential present above the bottom electrode and the gravitational force acting downwards. This is subjected to additional non-conservative forces, e.g., the ion-drag force, neutral friction, etc. As a spatial gradient of the ion drag force is present across the cloud dimensions, the dust cloud experiences a torque which makes it rotate. The electric field present in the cathode sheath region does not allow the negatively charged dust particle to fall on the cathode surface.

4.5 Summary and Conclusions

In a parallel-plate dc glow discharge plasma, the poloidal dust rotation in the vertical plane in absence of any external magnetic field has been observed and studied in detail. A concentric metallic ring is placed on the cathode. Dust particles are placed on the cathode surface unlike other experiments where dust is sprinkled from the top using a dispenser. A stable dust rotation is observed in the poloidal (vertical) plane and it is also toroidally continuous. Plasma behaviour is analysed with 2D profile measurements of plasma density, electron temperature and floating potential using a single Langmuir probe. Probe measurements reveal a strong radial density gradient at the location of the

dust cloud. The radial density gradient causes a shear/gradient in the ion drag force. The gradient in the ion drag force exerts a torque on the dust particle cloud. The dust particles move downwards against the sheath electric field in the regions of high ion drag force and upward in the regions with low values of ion drag force. PIV analysis is also performed to estimate the velocity profile of these vortices. PIV analysis reveals the velocity profile is similar to that of a rotating solid body.

5 CHAPTER: DOUBLE TORI

This chapter presents the observation of double torus. Section 5.1 provides a brief description of the modifications carried out for conducting the experiments and the initial observations with the help of a DSLR camera and Langmuir probe. A theoretical background will be outlined in section 5.2. Detail experimental analysis is presented in section 5.3. Finally, summary and conclusions are given in section 5.4.

5.1 Observation of double torus

Additional evidence that the density gradient is the root cause behind the poloidal rotation of dust particles is done by performing another experiment. In this experiment, in addition to the metallic ring, another metallic disc (diameter ~ 20 mm) is placed at the centre of the cathode concentric to the electrode system, as shown in Figure 5.1. In this case dust particles are kept on the area of the cathode in between the metallic disc and ring.



Figure 5.1: The picture shows the concentric metallic disk placed on the cathode surface along with the concentric metallic ring. The annular region between the ring and disk is covered by MF dust particles.

The presence of the metallic disc at the centre is expected to increase the plasma density at centre. Since the dust particles are dielectric in nature and have been spread uniformly (in this white dust ring shaped area when seen from the top as shown in Figure 5.1) over cathode, so this area is expected to have lesser plasma density than its surroundings. Thus the presence of metallic disc at the centre is expected to give rise to a density gradient near the centre in addition to the density gradient near the metallic ring surface. However, the direction of this new density gradient (at centre) is expected to be in the opposite direction (i.e., radially inward) to that present near the metallic ring (which is radially outward).

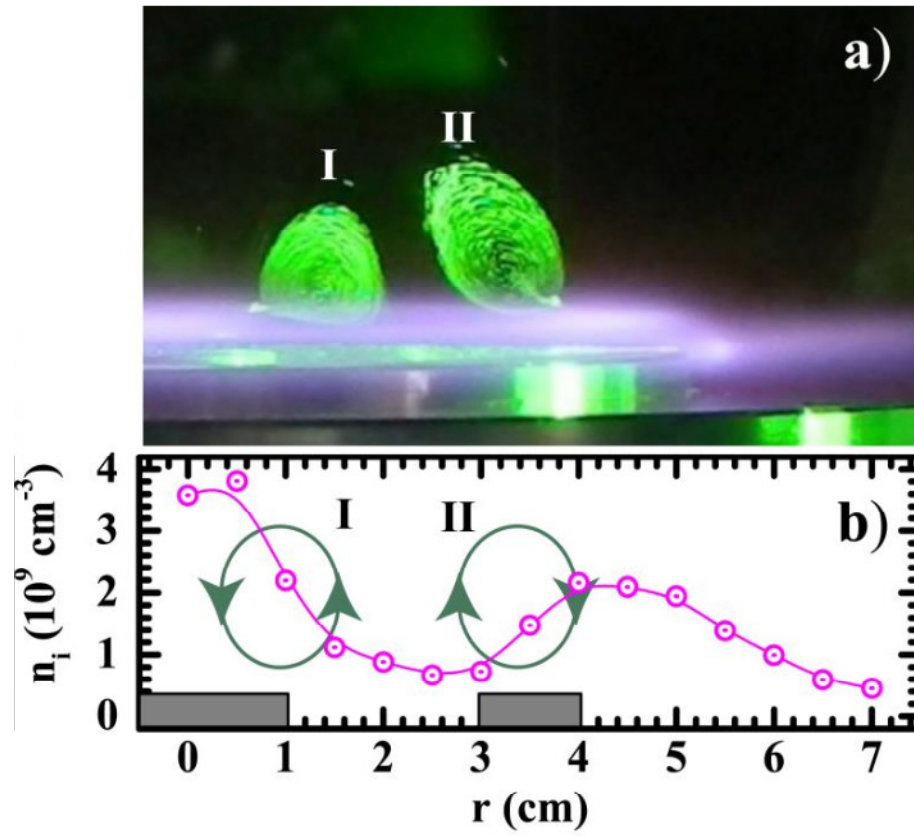


Figure 5.2: (a) A still Image showing the poloidal cross-sections of the double torii captured by a DSLR camera, illuminated by a laser sheet along the diameter of both the torii. Here, “I” and “II” represents the cross-section of the dust torus formed at the edge of the metallic disk and near the metallic ring, respectively. This image shows the radial extent of the vertical plane from centre to ~ 60 mm away from centre. (b) The radial profile of the plasma density at a height of 10 mm above the cathode surface at a pressure of 133 Pa and discharge current as 20 mA in the presence of a concentric metallic disk and ring.

After the placement of a concentric metallic disk on the cathode surface in presence of the metallic ring, additional toroidal dust structure is observed [86], as shown in Figure 5.2 (a), forming near the metallic disc boundary at a pressure of 133 Pa. For the sake of simplicity, this new toroidal structure is called as the inner torus and the older one as the outer torus. The dust particles in inner torus designated as “I” are also found to rotate poloidally but the sense of rotation is opposite to that of the outer one designated as “II”. The radial density profile obtained using the Langmuir probe confirms the existence of another density gradient near the centre in addition to that present at the metallic ring surface. The probe measurements also confirm that the direction of the density gradient near the centre is in the opposite direction to that present above ring surface as shown in Figure 5.2 (b). In both the cases, the dust particles are found to move towards the cathode surface where the ion density is higher and in the opposite direction where it is less. The generation of additional dust torus due to an additional density gradient and the direction of rotation of the dust particles confirms that gradient in the plasma density is playing a key role behind the rotation of dust particles in the poloidal direction.

5.2 Theoretical background for Dust Vorticity Generation

In the present work, we are interested in discussing the phenomenon occurring at a slow time scale at which the dust inertia plays a crucial role. Electrons and ions move so fast relative to the dust particles that they have enough time to equalize their temperature and contribute towards shielding. Electrons and ions can, therefore, be treated as a weakly coupled fluid due to their much smaller electric charges and higher temperatures compared to the dust fluid. For the description of the dust fluid, we adopt the hydrodynamic approach. Thus, the dust particle dynamics, in the presence of various

forces (such as $\vec{F}_g, \vec{F}_E, \vec{F}_i, \vec{F}_{Th}$ and \vec{F}_n) acting on them in plasma, can be described using Navier-Stokes equation:

$$\begin{aligned} m_d n_d \left(\frac{\partial \vec{v}_d}{\partial t} + (\vec{v}_d \cdot \nabla) \vec{v}_d \right) \\ = -\nabla p_E + n_d (\vec{F}_E + \vec{F}_g + \vec{F}_i + \vec{F}_n + \vec{F}_{Th}) + \eta \Delta \vec{v}_d, \end{aligned} \quad (5.1)$$

where, $\vec{F}_E, \vec{F}_g, \vec{F}_i$ and \vec{F}_n are the forces due to electric field, gravity, ion drag and neutral friction, respectively. n_d is the number density of the dust particles, p_E is the electrostatic pressure due to inter-particle interactions and confinement. At high gas pressures ($> 100 \text{ Pa}$), dust viscous friction $\eta \Delta \vec{v}_d$ can be neglected in comparison to the neutral gas friction; η represents the dust viscosity. Temperature driven flow is also neglected as dust vortices form even with actively cooled electrodes.

For determining the most probable cause of dust rotation theoretically, we define a new quantity, i.e., vorticity. The vorticity ($\vec{\omega}$) is defined as the curl of the velocity vector (\vec{v}_d). Thus, after taking the curl of both sides of equation (5.1), and replacing $\vec{\omega} = \nabla \times \vec{v}_d$, we obtain

$$\begin{aligned} \frac{d\vec{\omega}}{dt} &= \frac{\partial \vec{\omega}}{\partial t} + (\vec{v}_d \cdot \nabla) \vec{\omega} \\ &= (\vec{\omega} \cdot \nabla) \vec{v}_d - \vec{\omega} (\nabla \cdot \vec{v}_d) + \frac{1}{\rho_d^2} \nabla \rho_d \times \nabla p_E + \frac{1}{m_d} \nabla \times (\vec{F}_E + \vec{F}_g + \vec{F}_i + \\ &\quad \vec{F}_n) \end{aligned}$$

$$\begin{aligned}
\frac{\partial \vec{\omega}}{\partial t} = & -(\vec{v}_d \cdot \nabla) \vec{\omega} + (\vec{\omega} \cdot \nabla) \vec{v}_d - \vec{\omega}(\nabla \cdot \vec{v}_d) + \frac{1}{\rho_d^2} \nabla \rho_d \times \nabla p_E \\
& + \frac{1}{m_d} \nabla \times (\vec{F}_E + \vec{F}_g + \vec{F}_i + \vec{F}_n)
\end{aligned} \tag{5.2}$$

In the present case, the dust particle velocity is two-dimensional in nature, i.e., it has components which depend upon two coordinates (say y and z , and $v_x = 0$). In this case, vorticity, $(\vec{\omega} = \nabla \times \vec{v}_d)$, has only one component in the x -direction, and $(\omega \cdot \nabla)v$ is identically zero. Using these conditions in equation (5.2), the rate of change of vorticity for a two-dimensional, non-uniform density, viscid, incompressible flow can be written as

$$\begin{aligned}
\frac{\partial \vec{\omega}}{\partial t} = & \underbrace{-(\vec{v}_d \cdot \nabla) \vec{\omega}}_{(i)} + \underbrace{\frac{1}{\rho_d^2} \nabla \rho_d \times \nabla p_E}_{(ii)} + \underbrace{\frac{1}{m_d} \nabla \times (\vec{F}_E + \vec{F}_g + \vec{F}_i)}_{(iii)} \\
& + \underbrace{\frac{1}{m_d} \nabla \times \vec{F}_n}_{(iv)},
\end{aligned} \tag{5.3}$$

where ω is the vorticity experienced by the dust fluid and $\rho_d = m_d n_d$ is the dust particle density in the cloud. In equation (5.3), the different terms $(i) - (iv)$ represent the effects of; (i) change in vorticity along a streamline; (ii) generation of vorticity when the gradient in the dust density and pressure gradient are not aligned; (iii) torques due to non-conservative body forces and (iv) diffusion of vorticity associated with the viscous torque. The dust particle density is not uniform in the cloud. Due to the non-uniformity in the dust density, centre of mass of the dust cloud is displaced from its geometric centre and it can also contribute towards the generation of stream-wise

vorticity. But for the sake of simplicity, we assume the dust density in the cloud to be uniform. Under steady state conditions, the equation (5.3) takes the following form,

$$m_d(\vec{v}_d \cdot \nabla) \vec{\omega} = \frac{1}{m_d} \nabla \times (\vec{F}_E + \vec{F}_g + \vec{F}_i + \vec{F}_n). \quad (5.4)$$

The direction of ion drag force experienced by the dust particles is same as that of (the ion flow and) the electric field as $\vec{F}_i \propto \vec{v}_i$ where $\vec{v}_i = \mu_i \vec{E}$. Thus, the ion drag force can be written as

$$\vec{F}_i = F_i \hat{E}, \quad (5.5)$$

where F_i is the absolute value of ion drag force and \hat{E} is the unit vector in the direction of electric field.

Using equations (1.16), (1.17), (1.25) and (5.5) in equation (5.4), we obtain

$$m_d(\vec{v}_d \cdot \nabla) \vec{\omega} = \nabla \times (Z_d \vec{E} + F_i \hat{E} + m \vec{g} - m_d \nu_{dn} \vec{v}_d), \quad (5.6)$$

$$\nabla Z_d \times \vec{E} + \nabla F_i \times \hat{E} = m_d \nu_{dn} \nabla \times \vec{v}_d. \quad (5.7)$$

This kind of treatment has also been done in Ref [37]. The left hand side (LHS) of equation (5.6), i.e., the convective derivative of vorticity, is neglected in comparison to the neutral friction. In equation (5.7), the RHS represents the dissipative mechanism. Whereas, 1st and 2nd terms on the left hand side (LHS) of equation (5.7) represent the deriving mechanisms associated with the dust dynamics. Thus stationary dust rotation can be driven by a gradient of the ion drag force and/or by a charge gradient when either or both of them are aligned at an angle with the electric field. The presence of stationary rotation of dust particles in these structures indicates that the difference

between the drag force and repelling electric force is continuously being compensated by the dust friction on neutral gas.

5.3 Experimental Analysis

In the following, we estimate the values of all these three terms present in equation (5.7) experimentally and determine the dominant driving mechanism.

1) Gradient in the dust charge

After taking into account the ion-neutral collisionality, the charge on the dust particle, kept on plasma, is given by equation (1.5). For experiments dealing with mono-dispersed dust particles, the charge acquired by particles can vary only due to a variation in the density and temperature of the surrounding plasma. Since the electron temperature is nearly uniform over the radius, a radial variation in dust charge can arise if there is a radial variation in the plasma density. Figure 5.3 (a) shows the radial profile of the dust charge and its gradient, respectively. The dust charge gradient is calculated from every pair of dust charge measurements as $[(Z_d e)_{r_2} - (Z_d e)_{r_1}]/(r_2 - r_1)$ and is plotted versus the radius at $\{(r_2 + r_1)/2\}$. The values of the charge gradient at the location of inner dust torus I and the outer dust torus II are $e\nabla Z_d \approx 1.5 \times 10^5 e^- m^{-1}$ and $e\nabla Z_d \approx 1.4 \times 10^5 e^- m^{-1}$, respectively. In a constricted discharge like ours (inter electrode separation $\sim 40\text{ mm}$ and electrode diameter $\sim 90\text{ mm}$), though small, but substantial electric field $\sim 3\text{--}4\text{ Vcm}^{-1}$ exists in and above the negative glow region [87] where the rotating dust structure is located in our experiments. Hence, taking an ambient electric field of 3 Vcm^{-1} , the value of curl of electric force comes out to be $e\nabla Z_d \times \vec{E} \approx 7.2 \times 10^{-12}\text{ Nm}^{-1}$ for the inner torus I and $e\nabla Z_d \times \vec{E} \approx 6.7 \times 10^{-12}\text{ Nm}^{-1}$ for the outer dust torus II.

2) Gradient of Ion Drag Force

The ion drag force is one of the most dominant forces that come into picture due to the directed flow of ions towards the cathode surface. The major part of the dust cloud resides in the bulk plasma, where the ion velocity, v_i is composed of two parts; drift velocity and the thermal velocity, v_{thi} . At high pressures, the ion drift velocity is much less than their thermal velocity i.e., $v_i < v_{thi}$. Here $v_i = \mu_i E$, $\mu_i \left(= \frac{e}{m_i v_{in}} \right)$ being the ion mobility. However, these slowing drifting ions towards the cathode surface can still impart a considerable momentum on the dust particles present in their way in the bulk plasma. For frequent collisions, $\ell_i \leq \beta_T \lambda_D$, the expression for ion drag force [88], arising due to the sub-thermal ion flow is given by equation (1.22). Ion drag force is a function of dust charge as well as the plasma density at a pressure p .

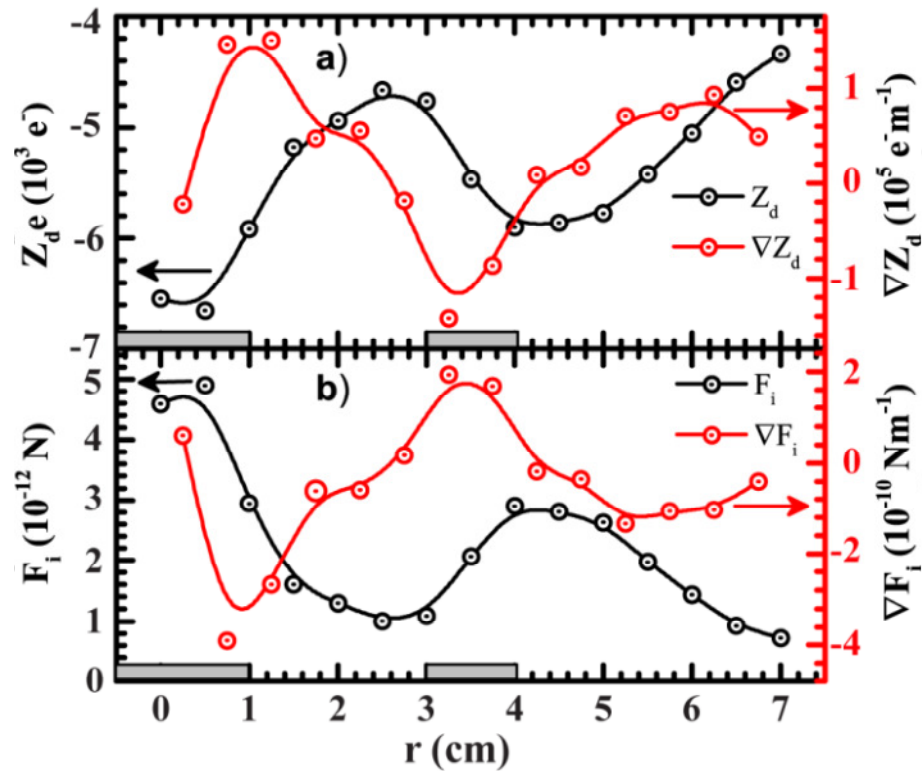


Figure 5.3: Radial profiles of a) dust charge and dust charge gradient and, b) ion drag force and its gradient at a height of 10 mm above the surface of cathode.

As is clear from equation (1.22), the ion drag force is a function of plasma density and charge acquired by the dust particles. The charge on the dust particles is found to be almost constant, whereas the plasma density has a sharp density gradient at the location of the formation of the rotating dust structures. The radial gradient in the plasma density (as shown in Figure 5.2 (b)) gives rise to a gradient in the ion drag force acting on the dust particles, as shown in Figure 5.3 (b). From the experimentally measured plasma density profile and an ambient electric field of $\sim 3 \text{ Vcm}^{-1}$, the radial variation of ion drag force as well as its gradient is estimated and is shown in Figure 5.3 (b). Again, the gradient in the ion drag force is calculated as $\left[\{(F_i)_{r_2} - (F_i)_{r_1}\} / (r_2 - r_1) \right]$ for every pair of estimated ion drag force and is plotted versus the radius at $\{(r_2 + r_1)/2\}$. From Figure 5.3(b), the corresponding values of gradients in the ion drag force for the inner dust torus I and outer dust torus II, are $\nabla F_i \times \hat{E} \approx 4 \times 10^{-10} \text{ Nm}^{-1}$ and $\nabla F_i \times \hat{E} \approx 2 \times 10^{-10} \text{ Nm}^{-1}$, respectively. The ion drag force corresponding to a single height above the cathode surface is determined. However, there might be a variation in the value of the gradient in the ion drag force but since its value is coming out to be of the order of the curl of the neutral friction, so it may be one of the main dominating factors playing a role in the dust rotation.

3) Curl of Neutral friction

At a gas pressure of 133 Pa with neutral temperature of $T_n \approx 0.03 \text{ eV}$, the value of the dust-neutral collision frequency, using equation (1.24), comes out to be $\sim 167 \text{ Hz}$. From the PIV analysis, the vorticity (ω) of the dust fluid possesses a value $\sim 20 \text{ s}^{-1}$ at a height of 9 mm above the cathode surface as shown in Figure 5.4 (c). The dissipative term in the RHS of equation (5.7) comes out to be

$$\nabla \times F_n = m_d \nu_{dn} \nabla \times \vec{v}_d \approx 6 \times 10^{-10} \text{ Nm}^{-1}.$$

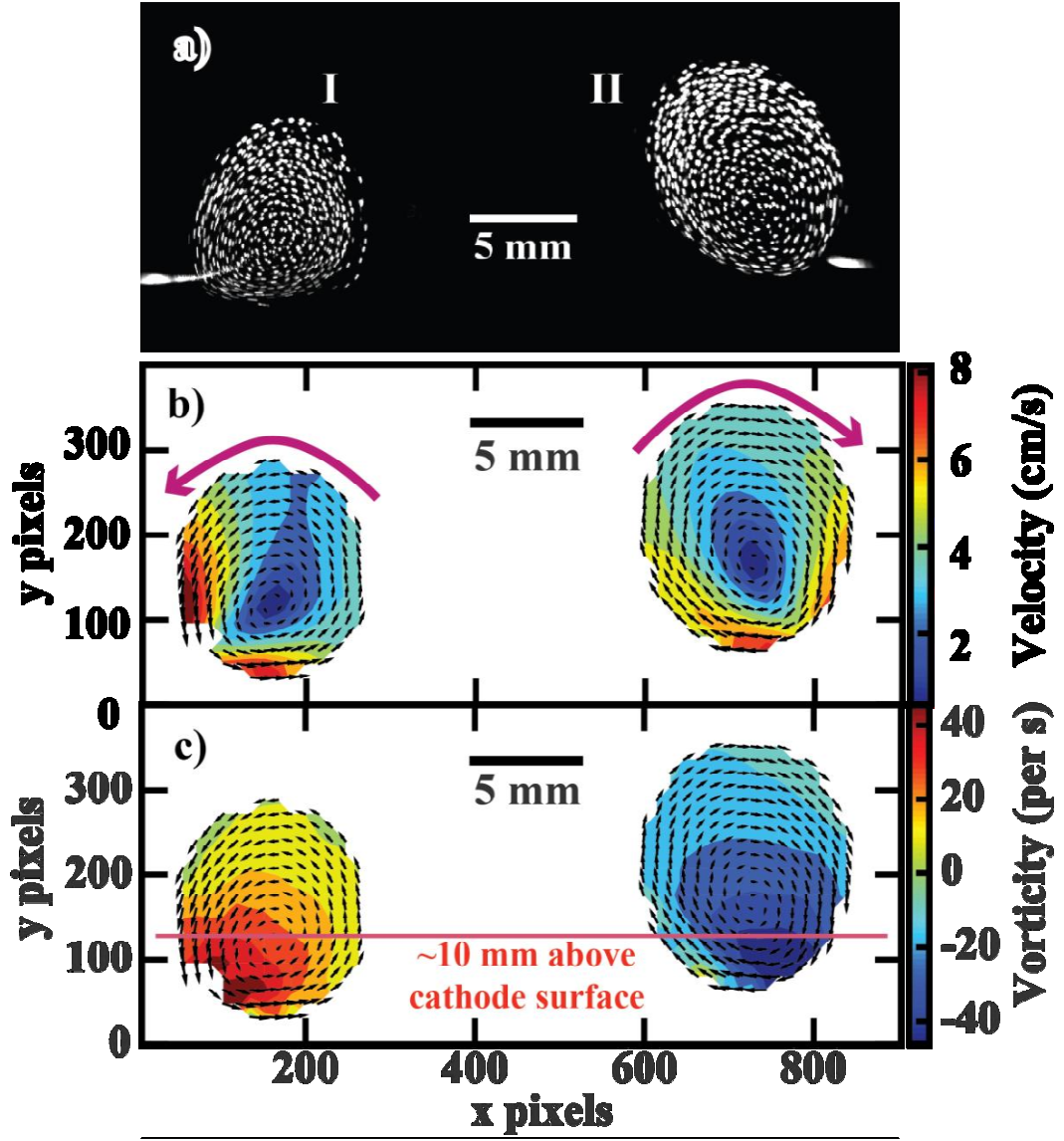


Figure 5.4: (a) The image of the poloidal cross-sections of the double dust tori while the laser sheet is passed along the diameter of both tori captured with the help of sCMOS camera at an exposure time of 4.9 ms in plasma formed with pressure of 133 Pa and discharge current as 20 mA. The spatial resolution of the image is as 1 pixel=38.9 μm . (b) Velocity vectors showing the direction of rotation of the dust particles is obtained using Davis software; the colour bar shows the value of dust velocity in cm s^{-1} . The left cloud shows the dust rotation in anti-clockwise direction and right hand cloud in the clockwise direction. (c) shows the vorticity profile associated with the rotation; the colour bar shows the value of vorticity in s^{-1} .

As mentioned earlier, the stationary dust rotation can be driven by a gradient of the ion drag force and a charge gradient. From the above estimations, it is found that for both the dust tori the value of $e\nabla Z_d \times \vec{E} \sim 7 \times 10^{-12} \text{ Nm}^{-1}$, which is more than one order

smaller to the other two terms in equation (5.7). This implies that the dust charge gradient is not responsible for exciting the dust rotation in the present experiments. However, the gradient in the ion drag force ($\approx 2 - 4 \times 10^{-10} \text{ Nm}^{-1}$) is of the order of the curl in the neutral frictional force ($\approx 6 \times 10^{-10} \text{ Nm}^{-1}$) for both the dust tori, which implies that the gradient in the ion drag force arising due to density gradient is the principal factor causing the dust particle rotation in the presented experiments. Both the results of single and double dust tori have two common features: a) vortices appear only where there is a density gradient and b) the dust particles move towards the cathode surface at locations with higher values of plasma density, while in the opposite direction where plasma density is lesser. The direction of dust rotation in these structures is consistent with the direction of the ion drag gradient arising due to the spatial density gradient. Therefore, the experimental observations and quantitative analysis clearly indicate that the shear in the ion drag force arising due to a gradient in the plasma density is the principal cause of vortex generation.

5.4 Summary and Conclusions

Self-organized poloidally rotating toroidally symmetric dust structure is reported in chapter 4, in unmagnetized parallel plate dc glow discharge at high pressures. In these experiments, a radial density gradient was created by placing a concentric metallic ring on the cathode surface. The location of the rotating dust structure was observed to coincide with the location of density gradient in the background plasma. A shear in the ion drag force arising due to the presence of the density gradient was conjectured to be the principal factor responsible for the poloidal rotation of the dust particles.

In this chapter, in order to further establish the correlation of ion drag force with the formation of dust vortices, an additional concentric metallic disk is placed on the

cathode surface inside the metallic ring to create another density gradient at a different radial location. In this configuration, a (non-monotonic) pair of density gradients, one near the boundary of the disk and another near the ring, lead to the formation of two toroidally symmetric, poloidally rotating dust structures. The direction of rotation of dust particles in the two vortices is also found to be opposite. This consolidates the importance of the role played by a density gradient in the formation of rotating dust structure. The gradient in dust charge and ion-drag force is estimated from the Langmuir probe measurements of background plasma density and temperature. The dust particle velocity in the rotating structures and the associated vorticity are measured using PIV analysis of images acquired with fast camera. The values of measured dust vorticity and estimated gradients of dust charge and ion-drag force are used in the vorticity equation obtained from Navier-Stokes formulation. Doing so, clearly, indicates that among the two possible driving mechanisms (i.e., dust charge gradient and ion drag gradient), the ion drag gradient is the main driving mechanism for the vortex generation. The results presented in the present research work may be of special significance towards the deeper understanding of the cause of generation of dust vortices/rotation observed in different laboratories and microgravity experiments as well as in different astrophysical events.

6 CHAPTER: EVOLUTION OF DUST ROTATION WITH DISCHARGE PARAMETERS

In CPED, numerous experiments are performed covering a wide range of discharge parameters such as gas pressure and discharge current. In this chapter, the results on the parametric study of discharge parameters on the poloidal vortex are presented. This chapter has been divided into three sections. In section 6.1, the evolution of the poloidally rotating structure with respect to the discharge current is discussed. Whereas in section 6.2, the evolution of these structures with background gas pressure is provided which is followed by a brief summary and conclusion in section 6.3.

6.1 Evolution with Discharge Current

In the previous chapter, it is observed that the ion drag force is the main driving parameter behind the poloidal rotation of dust particles in the toroidally symmetric structures. Therefore, with an increase or decrease in the driving factors, the properties of the rotating dust structures are also expected to vary accordingly. In this section, the parametric dependence of the poloidal vortices has been studied with respect to the discharge current by keeping the background pressure fixed. In a typical set of experiments, it is observed that the size of the dust cloud increases with an increase in the discharge current as shown in Figure 6.1. The dust particle velocity in the poloidal cross-section is also found to increase with an increase in the discharge current. Whereas, the dust density (number of dust particles per unit volume) in the poloidal cross-section decreases with an increase in the discharge current.

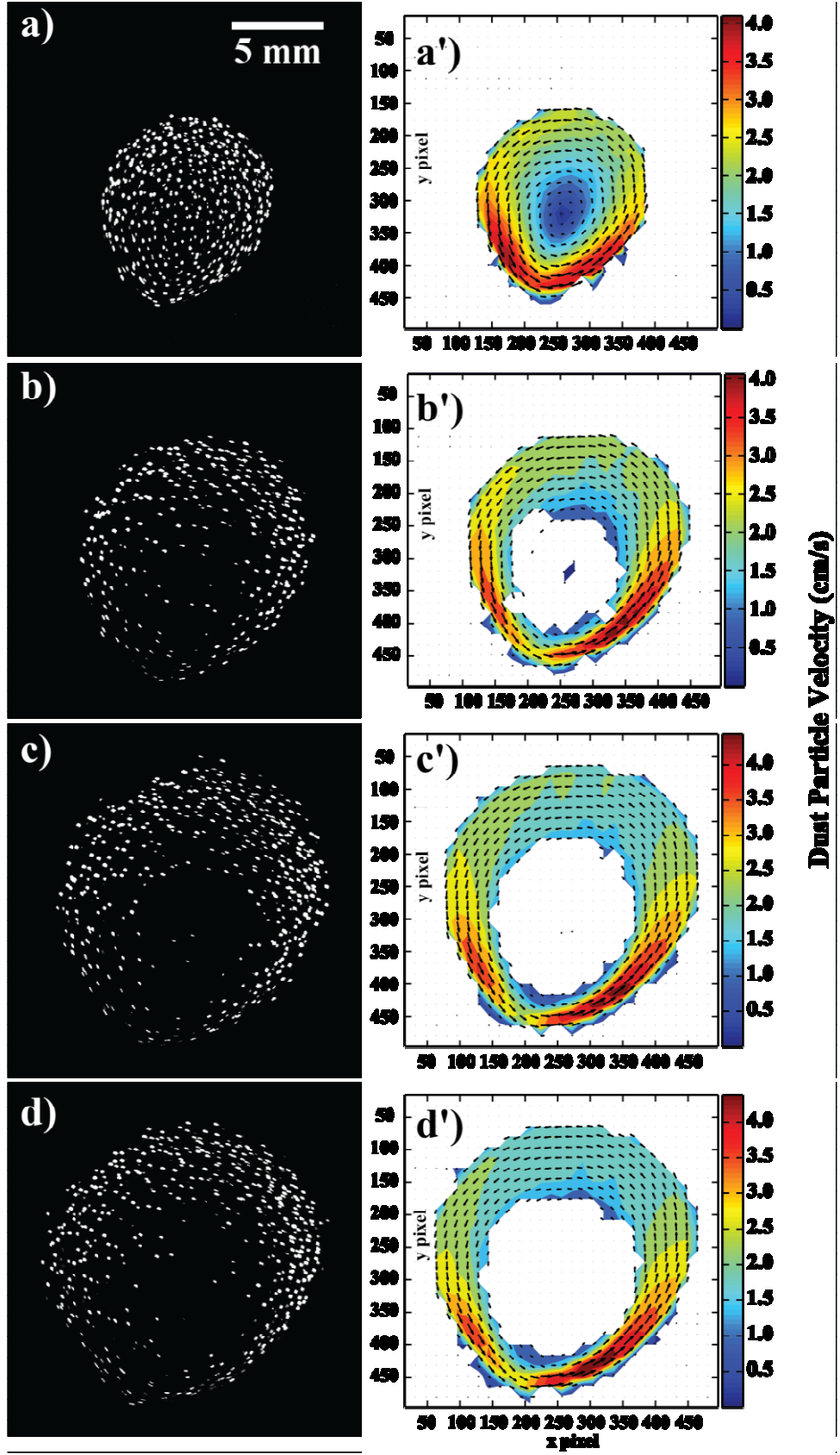


Figure 6.1: The still images taken with the help of sCMOS camera show the evolution of the poloidal cross-section with the a variation in the discharge current; a) $I_{\text{dis}} = 20$ mA, Voltage drop across electrodes (V_{drop}) = 254 V, b) $I_{\text{dis}} = 25$ mA, $V_{\text{drop}} = 258$ V, c) $I_{\text{dis}} = 30$ mA, $V_{\text{drop}} = 260$ V and d) $I_{\text{dis}} = 35$ mA, $V_{\text{drop}} = 260$ V

=262 V for a background pressure of 156 Pa. On the right hand side, the images with primes show the velocity profiles of the dust particles corresponding to different values of discharge current; different colours in the colorbar show the different magnitudes of dust velocity in cm s^{-1} .

To determine the reason behind this behaviour of these parameters, the radial measurements of plasma density are carried out at a height around 10 mm above the cathode surface. The plasma density measurements with the single Langmuir probe show that the plasma density increases as the discharge current is increased by keeping the background gas pressure constant (see Figure 6.2). Additionally, the radial density gradient is also found to increase with discharge current, which contributes towards an increase in the ion drag gradient.

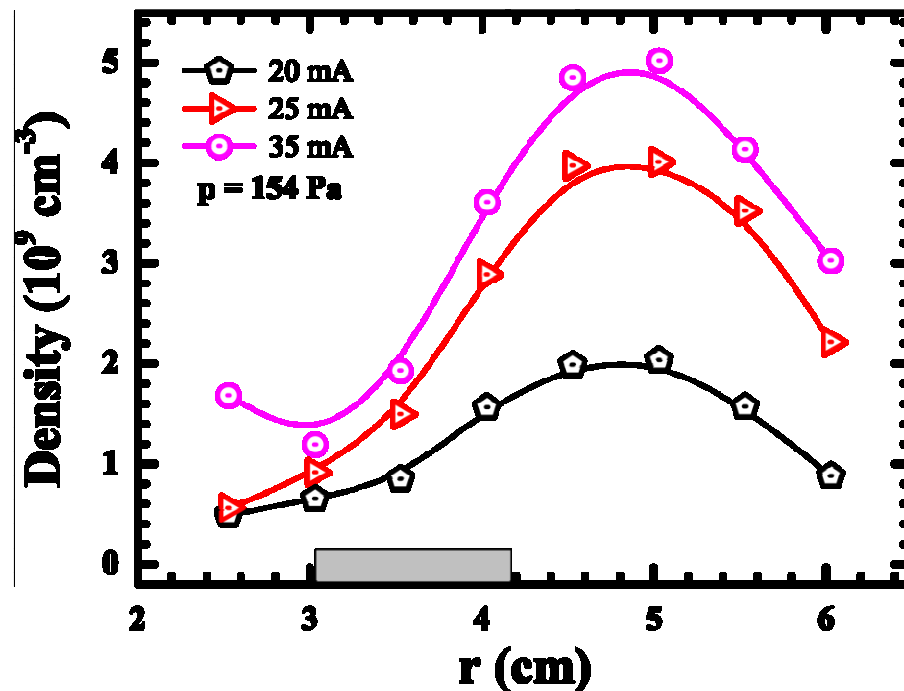


Figure 6.2: Langmuir probe measurements show an increase in the radial density gradient with an increase in the discharge current.

The increase in dust particle velocity may be attributed to the fact that there is an overall increase in the background plasma density and its radial gradient which is

basically the driver of these vortices. As the driving term increases, the dust particles start moving with higher velocity than that possessed by them initially. As the particle gains higher velocity (and hence, energy), it moves to a higher radial location than before. Hence, the dust density at the centre starts diminishing with an increase in discharge current.

Also with an increase in the background plasma density, the charge acquired by each dust particle is expected to increase, leading to an increase in the dust-dust repulsive forces. This may also contribute towards a decrease in the dust density with an increase in discharge current.

6.2 Evolution with Pressure

In this section, the experimental studies associated with the effect of the gas pressure on dust vortex (poloidal cross-section of the dust torus) are provided by keeping the discharge current constant. The poloidally rotating dust cloud forms above the surface of the metallic ring at high pressures. It has already been shown that as long as the dust clouds form with an increase in the pressure, dust particles present in the cloud possess a rotational motion in vertical plane. Due to the low mobility of ions, a high electric field is usually required to make them accelerated. In DC glow discharge, a large potential drops near the cathode for enhancing the ion bombardment on the cathode surface (for the ejection of electrons from its surface) and hence, producing a self-sustained discharge. The electric field, formed at the surface of cathode because of the large cathode potential drop, is high enough to make the negatively charged micron-sized dust particles levitate and thus, it prevents the downward moving particles from falling on the cathode surface.

After the formation of poloidally rotating dust structures, the gas pressure is increased at constant discharge current. With an increase in pressure, depending upon the discharge current and the density of the levitated dust particles, two types of distinct phenomena can be observed as shown in Figure 6.3 and Figure 6.4.

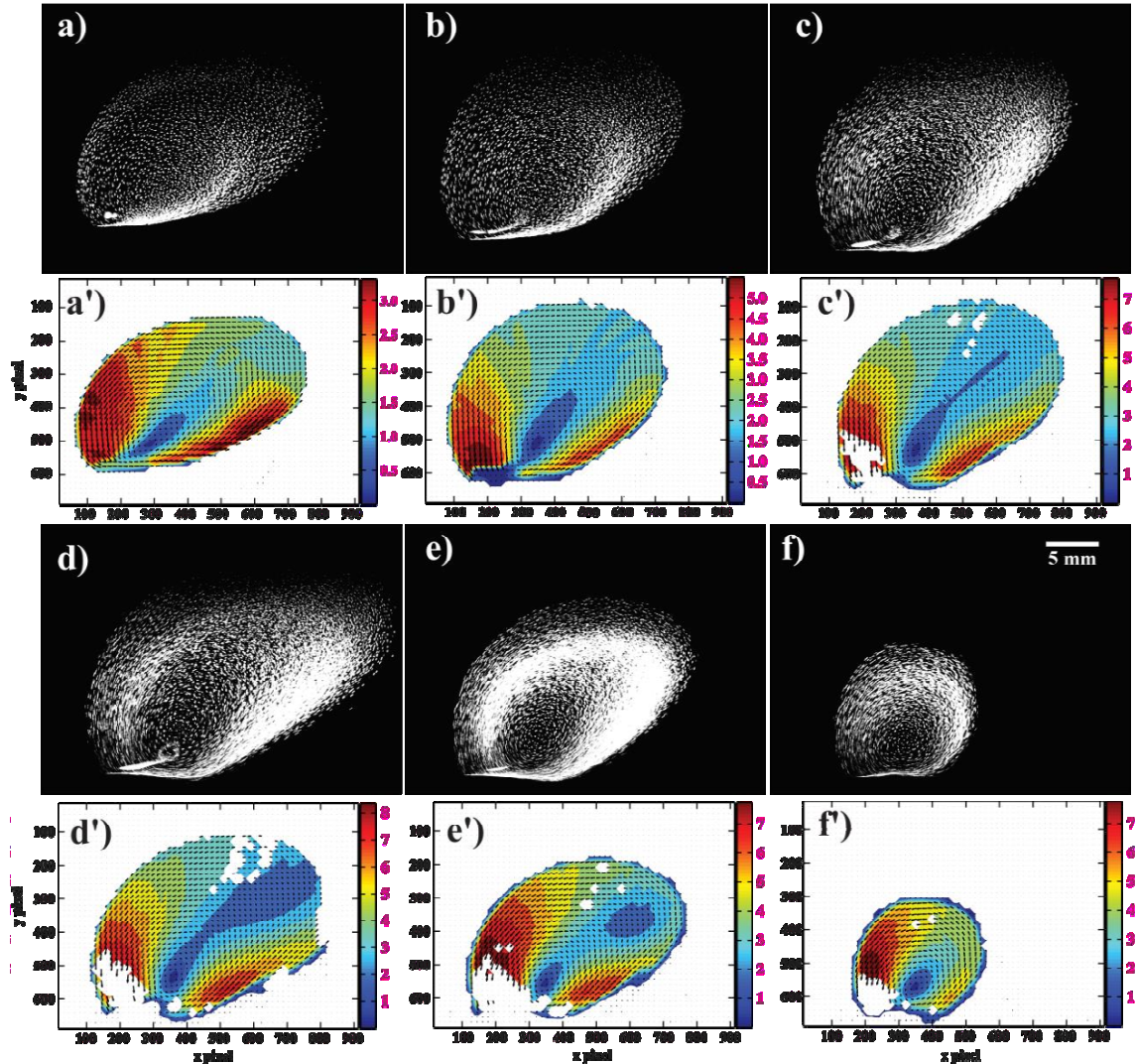


Figure 6.3: The variation in the poloidal cross-section of the dust torus with an increase in the background pressure at a discharge current of 25 mA: a) 92.9 Pa, b) 126 Pa, c) 184 Pa, d) 196 Pa, e) 213 Pa and f) 220 Pa. The colorbar shows the velocity in cm s^{-1} .

At high values of discharge current and low dust density, it is observed that the dust particle vortex undergoes a transition from a filled vortex to a vortex with void (dust-free region) at the centre and then again to a vortex with no void. Additionally, the size

of the vortex first increases and then attains a constant value. Whereas, no vortex structure with void at the centre inside is observed in case of low discharge current with high dust density. Also, the size of the dust cloud increases, reaches a maximum value and then start decreasing. The dust particle velocity is found to increase with an increase in pressure. The dust particles after gaining higher velocities go to higher radial locations leaving a dust free region at the centre and resulting in an increase in the size of the dust cloud. This dust free region acts as a vapour like phase with outer boundary (dust ring) as the fluid like phase. The filling of the dust ring can be because of the thermal agitation of the dust particles at higher pressures. In the following section, the effects of the increase in background gas pressure on the dust particle are discussed in detail.

6.2.1 Number of Dust Particles

With an increase in pressure, the number of dust particles in the dust vortex (appear as a disk of particles) first increases, then the vortex gets transformed into a dust ring at high discharge current. The number of dust particles gradually decreases, reaches a minima and increases again as the void in the dust ring starts filling with dust particles. Whereas, at low values of the discharge current, the levitated dust density always increases with an increase in pressure despite of reduction in the total number of levitated dust particles. The levitated dust number density, in addition to the discharge conditions, also depends upon the amount of dust particles present on the cathode as well as its distribution on cathode surface.

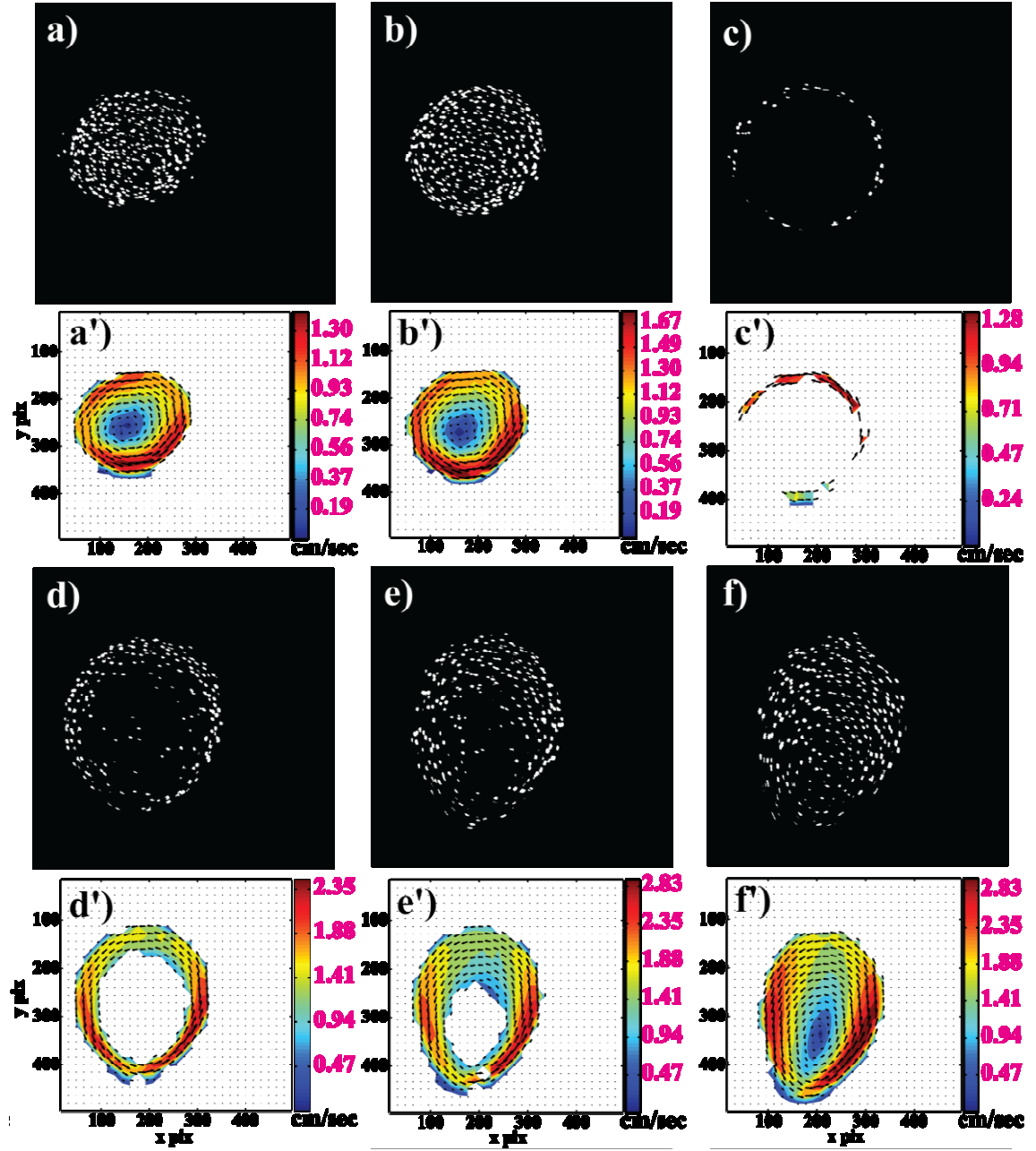


Figure 6.4: The variation in the poloidal cross-section of the dust torus with an increase in the background pressure at a discharge current of 37 mA: a) 84 Pa, b) 90.5 Pa, c) 115 Pa, d) 124 Pa, e) 205 Pa and f) 253 Pa. The colorbar shows the velocity in cm s^{-1} .

6.2.2 Dust Vortex Height above Cathode Surface

As the neutral gas pressure is increased, the height of the dust vortex/cloud above the electrode surface decreases as is shown in Figure 6.5 (a) and (b). In this case, the height of the cloud is measured as the distance of the bottom of the cloud above the cathode

surface. It is well-known that the cathode fall thickness decreases with an increase in the neutral gas pressure.

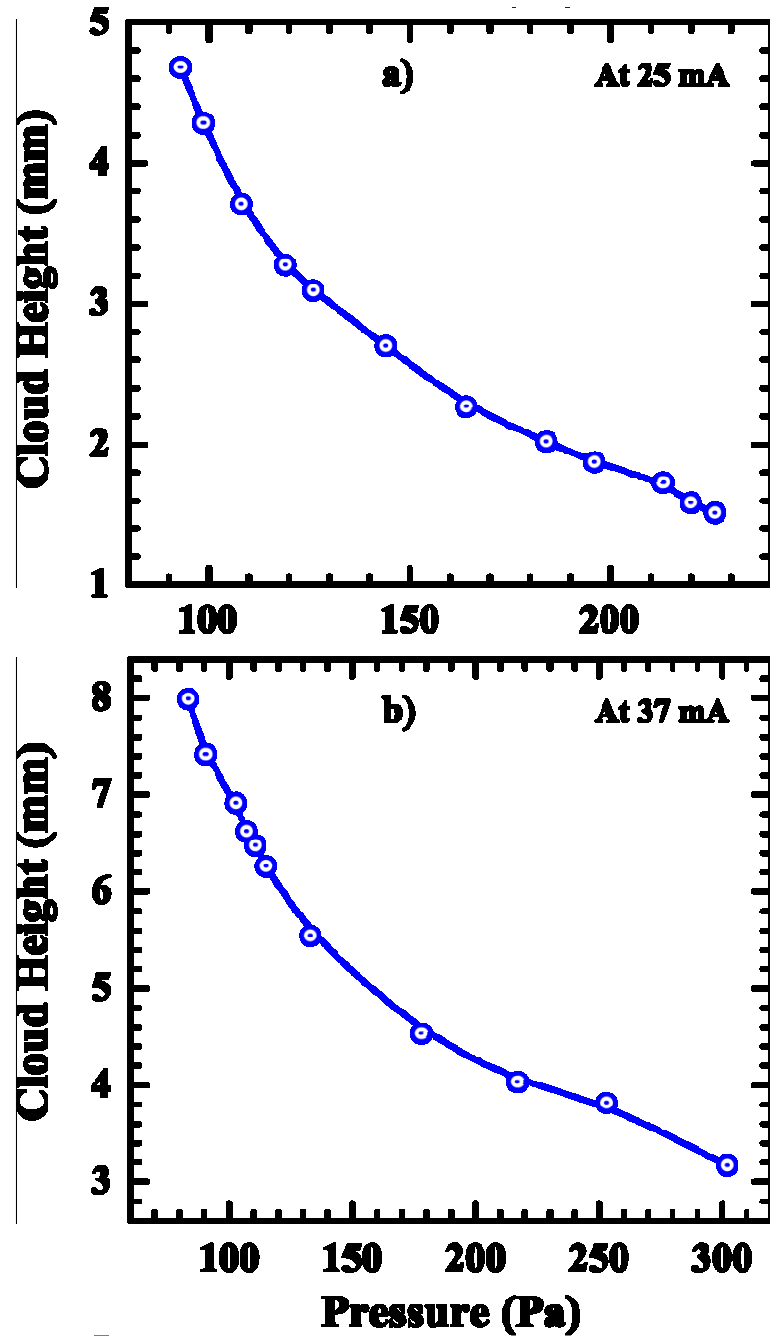


Figure 6.5: The decrease in dust particle cloud above the cathode with an increase in the background gas pressure at a fixed discharge current of (a) 25 mA and (b) 37 mA.

Also, the functional behaviour of the cathode sheath thickness with the pressure is same as that of the cloud height with pressure at constant discharge current. Thus, the decrease in the cloud height above the cathode surface may be due to a decrease in the cathode sheath thickness with pressure.

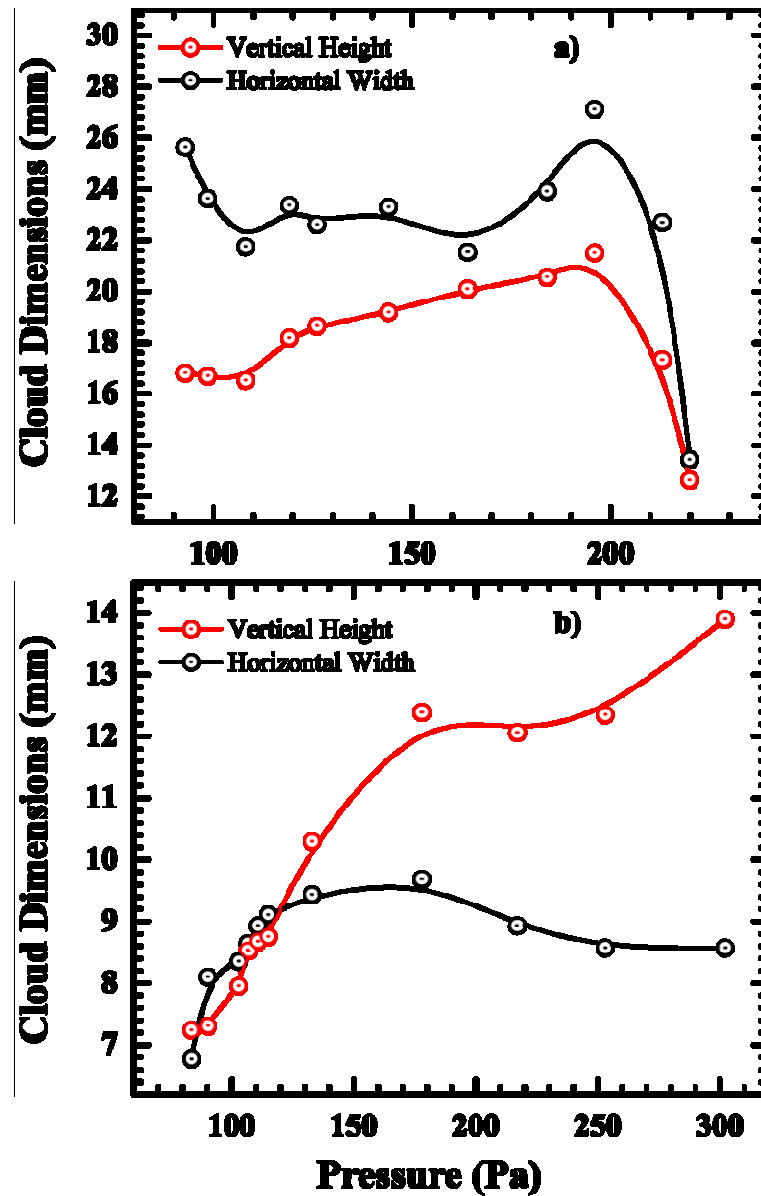


Figure 6.6: The evolution of the dust particle vortex dimensions with an increase in the background gas pressure at a fixed discharge current of (a) 25 mA and (b) 37 mA.

6.2.3 Dust Vortex Dimensions

With an increase in gas pressure, the size of the dust cloud also changes. As the dust vortex cross-section is elliptical (vertical ellipsoid with major axis at an angle with the $z - axis$) in nature, so it is easier to discuss the variation in its dimensions in terms of its vertical “height” and horizontal “width”. As the background gas pressure increases at a low discharge current, the dimensions of the dust vortex first remains nearly constant and then decreases sharply as shown in Figure 6.6 (a). Also, the effect of change in pressure is more dominant on the width of the vortex than on its height.

At high discharge currents, the dimensions of the dust vortex show an opposite behavior to that at low discharge current. With an increase in pressure, the vortex dimensions first increases sharply and then becomes almost constant as shown in Figure 6.6 (b). Additionally, the effect of increase in pressure is more dominant on the height of the vortex than on its width.

6.2.4 Dust Particle Velocity

The most interesting effect of the background neutral gas is seen on the dust particle velocity. The dust particle velocity in the poloidal vortex is found to increase with an increase in the gas pressure inspite of an increase in the neutral friction experienced by the dust particles, contrary to its usual behaviour reported in other experiments [33].

It has already been discussed in previous chapter that the dust rotation is driven by a radial gradient in the plasma density which further induces a gradient in the ion drag force. The radial gradient in the ion drag force acts as a torque on the dust particle cloud and makes it rotate. Therefore, the velocity of rotation of the dust particles in the vortex depends upon the value of gradient in the ion drag force. As the dust velocity increases with an increase in pressure, there should be a net increase in the driver too.

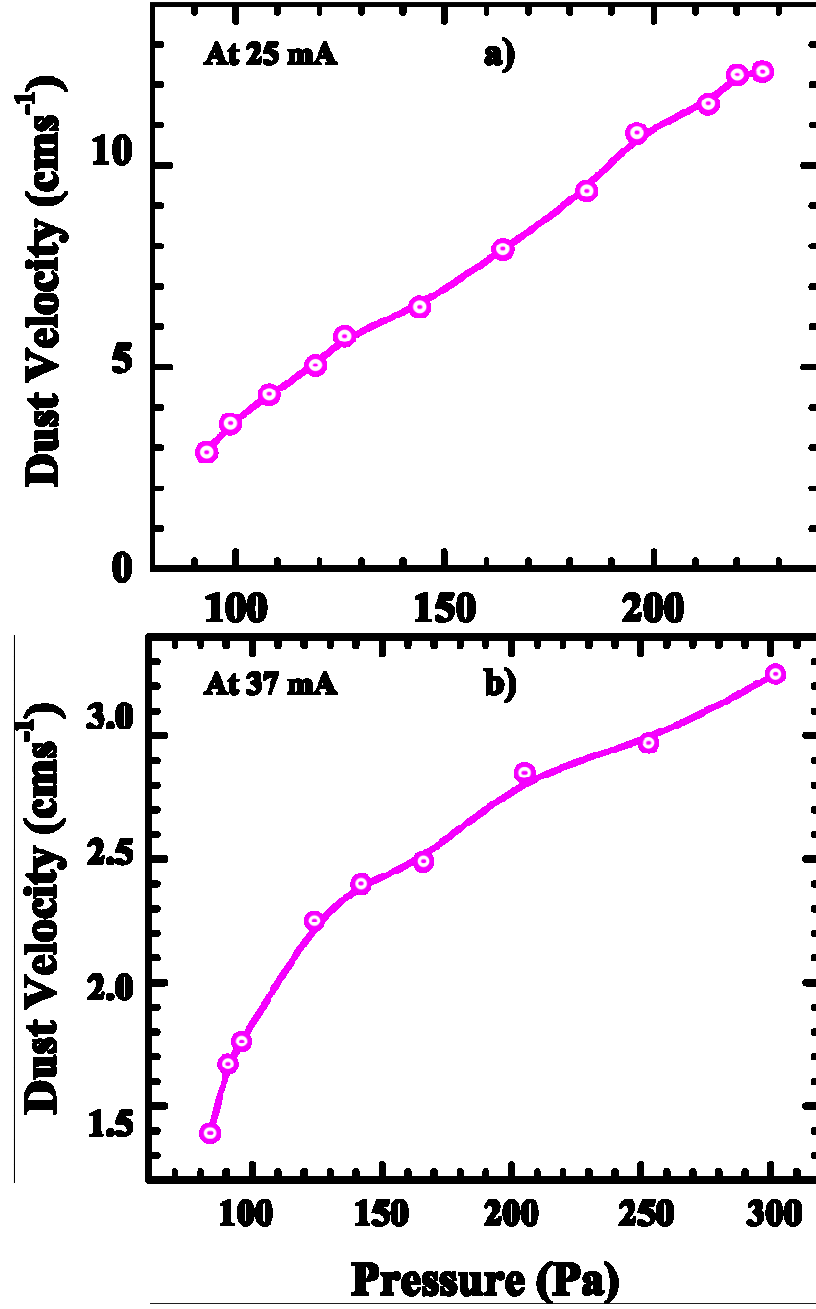


Figure 6.7: Increase in the particle velocity in the dust cloud with an increase in the background gas pressure at a fixed discharge current of (a) 25 mA and (b) 37 mA.

The expression for ion drag force from equation (1.22) can be further simplified as

$$F_i \cong \frac{1}{6} \frac{(Z_d e)^2}{\lambda_D} \frac{eE}{k_B T_i} \quad (6.1)$$

where $v_i = \mu_i E = \frac{eE}{m_i \nu_{in}}$; ν_{in} is the ion-neutral collision frequency. From the equation (6.1), it is clear that the ion drag force, $F_i \propto \sqrt{n_i} E$ and it is not an explicit function of pressure. That means the driver may increase with an increase in pressure either due to a steepening in the radial gradient of plasma density or due to an increase in the ambient electric field.

To determine the steepening in the radial gradient in plasma density (if present), the radial measurements of plasma density are carried out using Langmuir probe with an increase in pressure at fixed discharge current and is plotted in Figure 6.8. It is observed that initially the gradient in the plasma density increase with pressure but saturates at high pressure. Also, the absolute value of the plasma density decreases with an increase in pressure at the height at which the probe measurements are carried out. Thus, the steepening in the plasma density may contribute towards an increase in dust velocity but not at all pressure ranges.

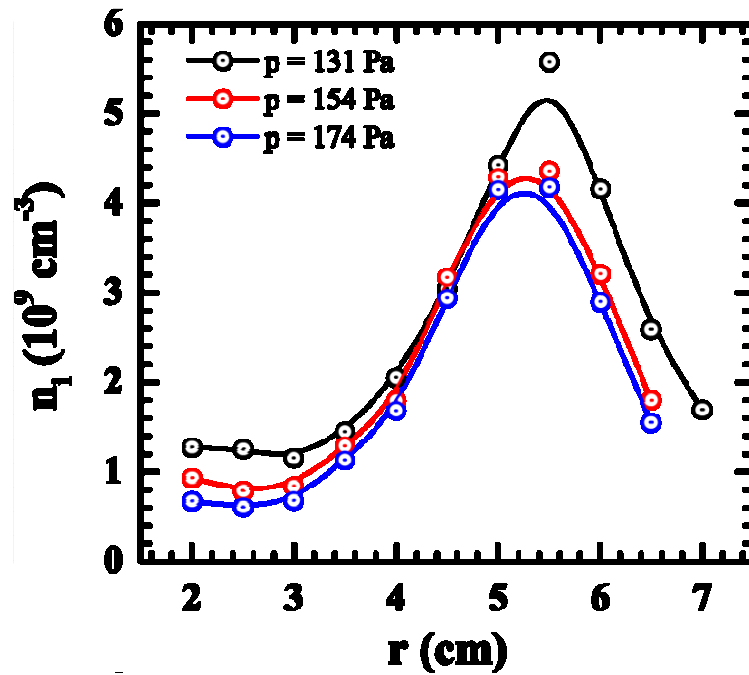


Figure 6.8: The radial variation in the plasma density with increase in pressure at a discharge current of 25 mA. The probe measurements are taken at a height of ~ 10 mm above the cathode surface.

Also, it has been observed by Carstensen *et al.* [43] in their experiments in presence of vertical magnetic field that the ion rotation in the horizontal plane can set the neutral gas into rotation via ion-neutral collisions which further acts as a driving force (in the direction of ion drag force) on the dust particles. This mechanism helped in the rotation of dust particles and result into an increased dust rotation frequency in their case. The expression for the force (F_{in}) experienced [43] by the neutrals due to their collisions with ions in a small volume dV is

$$dF_{in} = n_i m_i v_i v'_{in} dV, \quad (6.2)$$

and the viscous damping force (F_{visc}) experienced by the neutrals at viscosity (η) becomes

$$dF_{visc} = -\eta \Delta u_n dV, \quad (6.3)$$

where v_{in} and u_n are the ion-neutral collision frequency and neutral velocity respectively. For the neutral gas to have a flow in the direction of the ions, these two forces should balance each other i.e.,

$$\begin{aligned} dF_{visc} &= dF_{in} \\ \eta \Delta u_n dV &= -n_i m_i v_i v'_{in} dV \\ \Delta u_n &= -\frac{n_i m_i v_i v'_{in}}{\eta} \end{aligned} \quad (6.4)$$

where v'_{in} is the ion-neutral collision frequency which is a function of ion drift velocity.

In case of present experiments, the left hand side of equation (6.4) can be written as

$$\Delta u_n = u_n / d^2 \quad (6.5)$$

where d is of the order of the length of the gradient in plasma density. After using equation (6.5) in equation (6.4), we obtain

$$u_n = -\frac{n_i m_i v_i v'_{in} d^2}{\eta}. \quad (6.6)$$

For Argon gas ions at room temperature and a pressure of $\sim 133 \text{ Pa}$ in an electric field of $E = 3 \text{ Vcm}^{-1}$, $n_i = 1 \times 10^9 \text{ cm}^{-3}$, neutral viscosity, $\eta = 2.2 \times 10^{-5} \text{ Pa.s}$ and $d = 1 \text{ cm}$, the value of ion-induced neutral flow velocity becomes $\sim 6 \text{ cms}^{-1}$. However, it is clear from equation (6.6) that the neutral flow velocity does not increase with pressure, rather it decreases. Whereas, in our experiments, we observe a clear increase in the dust particle velocity which means if dust particle velocity is increasing due to ion-induced neutral flow then the neutral velocity should increase with an increase in pressure that may further contribute towards an increase in the dust particle velocity. Therefore, based on the above analysis, it is suggested that the ion-induced neutral flow may not contribute towards an increase in the velocity of dust particles with an increase in pressure (at higher pressures). This phenomenon is not fully understood till now and is an open question in the present situation and may be studied further.

6.3 Summary and Conclusions

The observations and results with an increase in the discharge current and background pressure can be summarized and concluded in the following way. With an increase in the discharge current, the dust velocity is found to increase with a small increase in the size of the poloidal cross-section which can be attributed to an overall increase in the absolute magnitude of the plasma density and an increase in its radial gradient. An increase in the fill-in gas pressure results into many interesting changes. A decrease in the

cathode fall thickness occurs which results into the decrease in dust particle cloud height from the cathode surface. A transition from filled-vortex to a vortex with void at the centre and then again to a filled-vortex is observed. The size of the dust vortex is also observed to vary with pressure in an interesting manner depending upon the value of the discharge current. Above all, the dust particle velocity increases at a sharp rate. Below are the major observations of the present experiment:

1. With the increase in background pressure, the dust particle velocity increases, contrary to an increase in the neutral friction.
2. At high discharge current, the dust vortex undergoes a transition from a filled-vortex to a vortex with void at the center and again to a filled-vortex.
3. At high discharge current, before the formation of vortex with void (at low pressures), the dust cloud was oblate like in shape while after the formation of the vortex with void (at higher pressures), it appears more like a prolate.
4. The height of the dust vortex from the surface of cathode decreases as the pressure increases.

7 CHAPTER: CONCLUSIONS AND FUTURE SCOPE

In this chapter, a brief summary and conclusion of the present work carried out in this research is provided in section 7.1 followed by a future scope in section 7.2.

7.1 Summary and conclusions

A device for carrying out sophisticated and complex dusty plasma experiments is designed, fabricated and made operational at the Institute for Plasma Research, India. The device is named as “**C**omplex **P**lasma **E**xperimental **D**evice (CPED)”. The main aim of this multipurpose machine is to study the formation and behaviour of dust vortices in absence of external magnetic field under the effect of various plasma parameters. Further, the device is equipped with advanced imaging diagnostics for studying many other interesting phenomena such as dust oscillations, three-dimensional crystalline structures and dust rotation, etc. The device is quite flexible to accommodate many innovative experiments related to dust oscillations, three-dimensional dust structures and phase transitions, intrinsic dust rotations, etc. Experiments on formation of poloidally rotating toroidally symmetric dust vortices in absence of external magnetic field in this device established the role played by gradients of ion drag force in dust cloud rotation along with the understanding of several other phenomena such as high amplitude dust oscillations, dust acoustics modes, crystal structures etc. Detailed design of the device, its diagnostics capabilities and the advanced image analysis techniques has been presented in this thesis.

As the working pressure in the present experiments is high ($> 100 \text{ Pa}$), so the ion-neutral collisions greatly affect the current collection to the probe. Also, the negatively

charged dust particles, present in plasma get, deposited on the current collecting surface of the probe when it's potential rises above the floating potential. While designing and using a Langmuir probe both these issues should be addressed. In the present research work, a specially designed Langmuir probe system is described and used for determining the pristine plasma parameters, which is immune to dust contamination and is capable of working in high pressure plasmas giving correct estimates of plasma parameters. Also, the biasing circuit of the probe has been suitably designed to minimize the effects of capacitive current and noise on the probe characteristics using tri-axial cable having a driven shield.

The rotation of dust particles in the vertical plane in a parallel-plate DC glow discharge plasma is reported. The experiments are carried out at high pressures ($> 100 \text{ Pa}$) with a metallic ring placed on the lower electrode. The dust cloud rotates poloidally in the vertical plane near the cathode surface. This structure is continuous toroidally. Absence of magnetic field rules out the possibility of $E \times B$ induced ion flow as the cause of dust rotation. The dust rotational structures exist even with water cooled cathode. Therefore, temperature gradient driven mechanisms, such as thermophoretic force, thermal creep flow and free convection cannot be causing the observed dust rotation. Langmuir probe measurement reveals the existence of a sharp density gradient near the location of the rotating dust cloud. The gradient in the density, giving rise to a gradient in the ion drag force, is identified as the principal cause behind the rotation of dust particles. The gradient in the ion drag force exerts a torque on the dust particle cloud. The dust particles move downwards against the sheath electric field in the regions of high ion drag force and upward in the regions with low values of ion drag force. PIV analysis is also performed to estimate the velocity field profile of the vortex rotation. This analysis reveals that the velocity profile is similar to that of a rotating solid body.

Observation of two well-separated dust vortices in an unmagnetized parallel plate DC glow discharge plasma is also reported in this thesis. A non-monotonic radial density profile, achieved by an especially designed cathode structure using a concentric metallic disk and ring of different radii, is observed to produce double dust tori between cathode and anode. This consolidates the importance of the role played by a density gradient in the formation of rotating dust structure. PIV analysis of the still images of the double tori shows oppositely rotating dust structures between the central disk and the ring. Langmuir probe measurements of background plasma shows a non-uniform plasma density profile between the disk and the ring. Location and sense of rotation of the dust vortices coincides with the location and direction of the radial gradient in the ion drag force caused by the radial density gradient. The experimentally observed dust vorticity matches well with the calculated one using hydrodynamic formulations with shear in ion drag dominating over the dust charge gradient. These results corroborate that a radial gradient in the ion drag force directed towards cathode is the principal cause of dust rotation.

In this thesis, we reported the evolution of these rotating dust structures with the discharge current and background gas pressure too. The dust particle velocity in the poloidal plane is found to increase considerably with an increase in the discharge current as well as with neutral gas pressure. The observations are made in the absence of any directed neutral gas flow arising due to method of its insertion and evacuation in the experimental region of interest. This behaviour of increase in the dust particle velocity with background neutral gas pressure is just opposite to the general trend of its decrease due to an increase in neutral friction.

The major accomplishments and findings of thesis are as follows:

1. **C**omplex **P**lasma **E**xperimental **D**evice (CPED), with a specially designed lower electrode (cathode) having the provision of active water cooling, is developed and operated at IPR for carrying out the physics studies related to the formation of dust vortices due to the presence of controllable density gradient.
2. For diagnosing the background plasma parameters, a low noise Langmuir probe system, capable of working at high pressures in a dusty plasma environment, is developed.
3. The observation of the poloidal rotation of mono-dispersed dust particles in toroidally symmetric structures is reported and is explained on the basis of the presence of a sharp density gradient at the location of the rotating structure. The radial density gradient gives rise to a radial gradient in the ion drag force, directed towards the cathode surface, which acts as a torque on the dust structure, making it rotate.
4. Ion drag force as the cause of formation of rotating structure is further verified by conducting another experiment by introducing additional density gradient. This leads to the formation of additional rotating structure at the location of the second gradient.
5. The dust particle dynamic is studied using hydrodynamic formulations. The estimated values of dust vorticity, (obtained from these formulations) due to a gradient in the ion drag force, is found to be well in agreement with the experimentally observed value of the dust vorticity.
6. The velocity profile of the dust particles is studied with the help of Particle Image Velocimetry (PIV) techniques which shows a rotating rigid body like behaviour of the rotating structures. Also, the dust particle velocity increases

while it moves towards the cathode surface (downwards) and decreases again in its upward motion.

7. The direction of rotation of the dust particles is found to be in accordance with the direction of the density gradient.
8. The evolution of the poloidal rotation of dust particles is studied with respect to the variation in the background gas pressure as well as the discharge current.
9. With an increase in the background gas pressure, the dust particle velocity in the poloidal plane is found to increase considerably. This behaviour of the dust particle velocity is exactly opposite to its usual behaviour.
10. With an increase in the discharge current, the dust particle velocity does increase but with a slower rate.

7.2 Future scope

In this section, a brief list of future works that can be carried out further is provided.

A two-dimensional density profile can be measured to make the argument, of a gradient in the ion drag force arising due to density gradient as the principal cause of rotation of dust particles, stronger. A two-dimensional mapping of the ambient plasma electric field can help in understanding the cause of an increase in the dust velocity with an increase in the background pressure. Both these measurements would be laborious but would provide a much detailed understanding of the phenomenon observed.

The cause of the vortex transition from a filled-vortex to a vortex with void at the centre is still very much unknown and can be studied further. The effect of ion induced neutral flow on the dust particle velocity with an increase in background pressure can also be studied further which may provide a new insight into the observed phenomena and may contribute towards the understanding of the peculiar behaviour of increase in dust

velocity with pressure. In some of the experiments, Kelvin-Helmholtz type of rotating structures have been observed which can also be studied further.

In the present thesis, the entire work has been done with one particle size and using Argon gas. This study can be further extended by using different mono-dispersed particle sizes and different background gases.

REFERENCES

- [1] C. K. Goertz, *Rev. Geophys.* 27, 271 (1989).
- [2] O. Havnes and G. E. Morfill, *Adv. Space Rev.*, 4, 85 (1984).
- [3] F. Li and O. Havnes, *Planet. Space Sci.*, 48, 117 (2000).
- [4] G. S. Selwyn, J. Singh, and R. S. Bennett, *J. Vac. Sci. Technol.*, 7, 2758 (1989).
- [5] P. Roca i Cabarrocas, P. Gay, and A. Hadjadj, *J. Vac. Sci. Technol. A*, 14, 655 (1996).
- [6] G.M.W. Kroesen, Netherland: Academic Publishers, Dordrecht, 1997, page 515.
- [7] Y. Feng, J. Goree, and Bin Liu, *Rev. Sci. Instrum.*, 78, 053704 (2007).
- [8] Edward Thomas, *Phys. Plasmas*, 6, 2672 (1999).
- [9] H. Ikezi, *Phys. Fluids*, 29, 1764 (1986).
- [10] J. H. Chu and Lin I, *Phys. Rev. Lett.*, 72, 4009 (1994).
- [11] H. Thomas, G. E. Morfill, V. Demmel, J. Goree, B. Feuerbacher and D. Mohlmann, *Phys. rev. Lett.*, 73, 652 (1994).
- [12] Y. Hayashi and S. Tachibana, *Jpn. J. Appl. Phys.*, 33, L804 (1994).
- [13] A. Melzer, T. Trottenberg, and A. Piel, *Phys. Lett. A*, 191, 301 (1994).
- [14] V. E. Fortov, A. P. Nefedov, V.M. Torchinskii, V.I. Molotkov, A. G. Khrapak, O.F.Petrov, K. F. Volykhin, *Journ. Exp. Theoretical Phys. Lett.*, 64, 92 – 98 (1996).
- [15] G. E. Morfill, H. M. Thomas, U. Konopka, H. Rothermal, M. Zuzic , A. Ivlev, J. Goree, *Phys. Rev. Lett.*, 83, 1598 (1999).
- [16] J. Goree, G. E. Morfill, V. N. Tsytovich, and S. V. Vladimirov, *Phys. Rev. E*, 59, 7055 (1999).
- [17] V. N. Tsytovich, S. V. Vladimirov, G. E. Morfill, and J. Goree, *Phys. Rev. E*, 63, 056609 (2001).
- [18] M. R. Akdim and W. J. Goedheer, *Phys. Rev. E*, 67, 056405 (2003).
- [19] N. A. Horton and D. Pokrajac, *Phys. Fluids*, 21, 045104 (2009).
- [20] A. Groisman and V. Steinberg, *Nature*, 405, 53 (2000).

- [21] S.A. Khrapak and G.E. Morfill, *Phys. Plasmas*, 15, 114503 (2008).
- [22] Andre Melzer, *Introduction to Colloidal (Dusty) Plasmas*. Greifswald, Germany, 2012. <http://www5.physik.uni-greifswald.de/skript/skript.pdf>
- [23] Chunshi Cui and J. Goree, *IEEE Transactions on Plasma Science*, 22, 151(1994).
- [24] A. V. Ivlev, S. K. Zhdanov, S.A. Khrapak, and G. E. Morfill, *Plasma Phys. Control. Fusion*, 46, B267-B279 (2004).
- [25] C Zafiu, A Melzer, and A Piel, *Phys. Plasmas*, 10, 1278 (2003).
- [26] S. A. Khrapak , A. V. Ivlev, H. M. Thomas, and H. M. Thomas, *Phys. Rev. E*, 66, 046414 (2002).
- [27] A. V. Ivlev, S.A. khrapak, S. K. Zhdanov, and G. E. Morfill, *Phys. Rev. Lett.*, 90, 205007 (2004).
- [28] A. V. Ivlev, S. K. Zhdanov, S. A. Khrapak, and G. E. Morfill, *Phys. Rev. E*, 71, 016405 (2005).
- [29] A.F. Pal, A. N. Ryabinkin, A. O. Serov, N. A. Dyatko, A. N. Starostin, A. V. Filippov, *Journ. of Exp. Theoret. Phys.*, 114, 535 (2012).
- [30] P. K. Shukla and A. A. Mamun, *Introduciton to Dusty Plasmas.*: IOP Bristol, 2010.
- [31] Y. Nakamura, H. Bailung, and P. K. Shukla, *Phys. Rev. Lett.*, 83, 1602 (1999).
- [32] Q-Z, Luo, N. D'Angelo, and R. L. Merlino, *Phys. Plasmas*, 6, 3455 (1999).
- [33] O. S. Vaulina, A. A. Samarian, O. F. Petrov, B. James, and F. Melandso, *Plasma Phys. Reports*, 30, 918 – 936 (2004).
- [34] N. N. Rao, P. K. Shukla, and M. Y. YU, *Planet Space Sci.*, 38, 543 - 546 (1990).
- [35] J. Pramanik, G. Prasad, A. Sen, and P. K. Kaw, *Phys. Rev. Lett.*, 88, 175001 (2002).
- [36] R. L. Merlino, *Phys. Plasmas*, 16, 124501 (2009).
- [37] Tim Bockwoldt, Oliver Arp, Kristoffer Ole Menzel, and Alexander Piel, *Phys. Plasmas*, 21, 103703 (2014).
- [38] U. Konopka, D. Samsonov, A. V Ivlev, J. Goree, and V. Steinberg, *Phys. Rev. E*, 61, 9 (2000).
- [39] Nariyoshi Sato, Giichiro Uchida, Toshiro Kaneko, Shinya Shimizu, and Satoru Lizuka, *Phys. Plasmas*, 8, 1786 (2001).

- [40] K. Matyash, M. Frohlich, H. Kersten, G. Thieme, R. Schneider, M. Hannemann, R. Hiller, *J. Phys. D: Appl. Phys.*, 37, 2703 - 2708 (2004).
- [41] Felix Cheung, Alex Samarian, and Brian James, *New Journ. Phys.*, 5, 75 (2003).
- [42] Iris Pilch, Torben Reichstein, and Alexander Piel, *Phys. Plasmas*, 15, 103706 (2008).
- [43] J. Carstensen, Franko Greiner, Lu-Jing Hou, Horst Maurer, and Alexander Piel, *Phys. Plasmas*, 16, 013702 (2009).
- [44] Yoshifumi Saitou and Osamu Ishihara, *Phys. Rev. Lett.*, 111, 185003 (2013).
- [45] D. A. Law, W. H. Steel, B. M. Annaratone, and J. E. Allen, *Phys. Rev. Lett.*, 80, 4189 (1998).
- [46] O. S. Vaulina, A. A. Samarian, A. P. Nefedov, and V. E. Fortov, *Phys. Lett. A*, 289, 240 (2001).
- [47] O. S. Vaulina, A. A. Samarian, O. F. Petrov, B. W. James, and V. E. Fortov, *New Journ. Phys.*, 5, 82 (2003).
- [48] O. S. Vaulina, O. F. Petrov, V. E. Fortov, G. E. Morfill, H. M. Thomas, Yu. P. Semenov, A. I. Ivanov, S. K. Krikalev, Yu. P. Gidzenko, *Physica Scripta*, T107, 224 (2004).
- [49] A. A. Samarian, O. Vaulina, W. Tsang, and B. W. James, *Physica Scripta*, T98, 123 (2002).
- [50] Giichiro Uchida, Satoru Iizuka, Tetsuo Kamimura, and Nariyoshi Sato, *Phys. Plasmas*, 16, 053707 (2009).
- [51] M Schwabe, L-J Hou, S. Zhdanov, A. V. Ivlev, H. M. Thomas, G. E. Morfill, *New Journ. Phys.*, 13, 083034 (2011).
- [52] S. Mitic, R. Sutterlin, A. V. Ivlev, H. Hofner, H. M. Thomas, S. Zhdnov, G. E. Morfill, *Phys. Rev. Lett.*, 101, 235001 (2008).
- [53] T. M. Flanagan and J. Goree, *Phys. Rev. E*, 80, 046402 (2009).
- [54] Modhuchandra Laishram, Devendra Sharma, Pradhiman Kaw, *Phys. Plasmas*, 21, 073703 (2014).
- [55] Michael A. Dopita, Charlene Heisler, Stuart Lumsden, and Jeremy Bailey, *The Astrophys. Journ.*, 498, 570 - 578 (1998).
- [56] James P. Gleenson, *Phys. Fluids*, 17, 100614 (2005).
- [57] A. J. Chorin, *Vorticity and Turbulence*. New York: Springer-Verlag, 1998.

- [58] Mierk Schwabe, Sergey Zhdanov, Christoph Rath, David B. Graves, Hubertus M. Thomas, Gregor E. Morfill, *Phys. Rev. Lett.*, 112, 115002 (2014).
- [59] G. E. Morfill, M. R. Zuzic, Rothermel Hermann; A. V. Ivlev, B. A. Klumov, H. M. Thomas, U. Konopka, *Phys. Rev. Lett.*, 92, 175004 (2004).
- [60] H. M. Mott-Smith and Irving Langmuir, *Phys. Rev.*, 28, 727 (1926).
- [61] J. E. Allen, R. L. F. Boyd, and P. Reynolds, *Proc. Phys. Soc.*, 3B, 297 (1957).
- [62] F. F. Chen, *Plasma Phys.*, 7, 47 (1965).
- [63] James G. Laframboise, "Theory of spherical and cylindrical Langmuir probes in a collisionless, Maxwellian plasma at rest," UTIAS report No. 100 (1966).
- [64] Roger E. Kiel, *AIAA Journal*, 6, 708 (1968).
- [65] E. W. Peterson and L. Talbot, *AIAA Journal*, 8, 1391 (1970).
- [66] Christoph Steinbruchel, *J. Vac. Sci. Technol.*, A 8, 1663 (1990).
- [67] A. Karamcheti and Ch. Steinbruchel, *J. Vac. Sci. Technol.*, A 17, 3051 (1999).
- [68] G. Narasimhan and Ch Steinbruchel, *J. Vac. Sci. Technol.*, A 19, 376 (2001).
- [69] Michael Mausbach, *J. Vac. Sci. Technol.*, A 15, 2923 (1997).
- [70] F. F. Chen, *Phys. Plasmas*, 8, 3029 (2001).
- [71] P. M. Bryant, *Plasma Sources Sci. Technol.*, 18, 014013 (2009).
- [72] Z. Zakrzewski and T. Kopiczynski, *Plasma Phys.*, 16, 1195 (1974).
- [73] George J. Schulz and Sanborn C. Brown, *Phys. Rev.*, 98, 1642 (1955).
- [74] S. Klagge and M. Tichy, *Czech. J. Phys. B.*, 35, 988 (1985).
- [75] Y. S. Chou, L. Talbot , and D. R. Willis, *Phys. Fluids*, 9, 2150 (1966).
- [76] L. Talbot and Y. S. Chou, *Raefied Gas dynamics.*: Ac. Press 1723, 1966.
- [77] M. Tichy, M. Sicha, P. David, and T. David, *Contrib. Plasma Phys.*, 34, 59 – 68 (1994).
- [78] C. H. Su and R. E. Kiel, *Journal Appl. Phys.*, 37, 4907 (1966).
- [79] Markus Klindworth, "*Fundamentals and Applications of langmuir Probe Diagnostics in Complex Plamas*", Kiel (2001).
- [80] M. Klindworth, O. Arp, and A. Piel, *Rev. Sci. Instrum.*, 78, 033502 (2007).

- [81] T. F. Yang, Q. F. Zu, and Ping Liu, *Rev. Sci. Instrum.*, 66, 3879 (1995).
- [82] Robert B. Lobbia and Alec D. Gallimore, *Rev. Sci. Instrum.*, 81, 073503 (2010).
- [83] E. O. Johnson and L. Malter, *Phys. Rev.*, 80, 58 (1950).
- [84] Manjit Kaur, Sayak Bose, P. K. Chattopadhyay, D. Sharma, J. Ghosh and Y. C. Saxena, *Phys. Plasmas*, 22, 073703 (2015).
- [85] A. Liberzon, R. Gurka, and Z. Taylor, "OpenPIV," (2009).
<http://www.openpiv.net>.
- [86] Manjit Kaur, Sayak Bose, P. K. Chattopadhyay, D. Sharma, J. Ghosh ,Y. C. Saxena and Edward Thomas Jr., *Phys. Plasmas*, 22, 093702 (2015).
- [87] V. A. Lisovskiyy and N. D. Kharchenko, *Plasma Phys. reports*, 26, 1066 (2000).
- [88] V. E. Fortov and G. E. Morfill, *Complex and Dusty Plasmas: From Laboratory to Space*.: CRC Press, 2010.